2018

Geochronological Constraints On The Timing Of Deformation: An Examination Of The Prospect Rock Fault Footwall In North-Central Vermont

Evan Tam
University of Vermont

GEOCHRONOLOGICAL CONSTRAINTS ON THE TIMING OF DEFORMATION: AN EXAMINATION OF THE PROSPECT ROCK FAULT FOOTWALL IN NORTH-CENTRAL VERMONT

A Thesis Presented

by

Evan Tam

to

The Faculty of the Graduate College

of

The University of Vermont

In Partial Fulfillment of the Requirements
for the Degree of Master of Science
Specializing in Geology

October, 2018

Defense Date: June 14, 2018
Thesis Examination Committee:

Laura E. Webb, Ph.D., Advisor
Ehsan Ghazanfari, Ph.D., Chairperson
Keith A. Klepeis, Ph.D.
Cynthia J. Forehand, Ph.D., Dean of the Graduate College

ABSTRACT

The Prospect Rock Fault (PRF) is key to our understanding of the regional tectonic evolution of Vermont during the Taconic, Salinic, and Acadian Orogenies, and may have played an important role in the exhumation of blueschist and eclogite-facies rocks in the Tillotson Peak Complex (TPC) during the Taconic Orogeny. The TPC is in the footwall of the PRF in the eastern limb of the Green Mountain Anticlinorium. In the TPC, the dominant foliation is S_2 and E-W trending F_2 folds parallel L_2 stretching lineations, which trend orthogonal to regional N-S trending folds associated with the Taconic Orogeny. The PRF itself is folded by F_2 folds. Presently, there is a lack of consensus about the role of the PRF in the exhumation of the TPC, and studies have not reconciled the formation of the E-W folds and lineations to a regional model.

Oriented samples and structural data were collected from the footwall of the PRF over several transects. Samples were processed into orthogonal thin sections for microstructural analyses and for $^{40}Ar/^{39}Ar$ step heating of white mica. The dominant foliations in the PRF samples were identified through microstructural analysis and correlating the age of deformation as S_2 and S_3. These were defined in thin section by mica and quartz microlithons, and oriented mica grains. S_1, and in some samples S_2, are locally preserved in some mica domains and albite/garnet inclusion trails. S_4 appears as crenulations of S_3, with no significant new mineral crystallization. In the field, L_2 and L_3 lineations are defined by mineral and quartz rods, and L_4 lineations are defined as intersection lineations on S_2 surfaces.

$^{40}Ar/^{39}Ar$ analyses yielded plateau ages ranging from 458.6 ± 2.0 Ma to 419.0 ± 2.4 Ma (1σ). The oldest plateau ages are just slightly younger, yet concordant, with published and new $^{40}Ar/^{39}Ar$ ages from the TPC and come from the structurally highest portions of the footwall in the northern part of the study area. Virtually all apparent age spectra show age gradients. Results from this study suggest the PRF played a role in exhumation of the TPC and ages obtained are closely aligned with deformation ages constrained from $^{40}Ar/^{39}Ar$ dating in southern Quebec for the Taconic D_2 and Salinian D_3 deformation. These dates may aid correlatation of ages and structures regionally and further refining of tectonostratigraphic models describing southern Quebec and New England.

ACKNOWLEDGEMENTS

The completion of this thesis document is certainly the apex of my academic career, but I would nowhere without the help and support of my mentors, friends, and family. First, I wish to thank my advisor Dr. Laura Webb; I always felt encouraged to ask more questions, and to come to you for help when I needed it. Your advice was always encouraging, practical, and never stress-inducing in the least. I learnt many skills from you in the lab, field, and at my desk. I am also thankful to my committee members Keith Klepeis and Ehsan Ghazanfari for offering advice, helping my thesis evolve past my own limits. I must also thank my mentors, Timothy Byrne and Will Ouimet, from my alma matter at the University of Connecticut. Without your inspiration, I would no doubt be elsewhere working on who knows what.

I also extend my thanks to members of our UVM geology department. I am proud to have had such a reliable, and wisecracking lab partner in Cheyne Aiken. Your thoughts, insights, and jokes have kept me safe and sane, in the field and the lab. Dan Jones, thank you for teaching me new skills and offering a refreshing break when needed. Keith Klepeis, Jon Kim, and Stephen Wright; thank you for teaching me new field skills and about Vermont's complex geology. Furthermore, many people traveled into the field with Cheyne and I, including Hannah Blatchford, Beth Pidgeon, John Mark Brigham, Joe Gonzales, and Suzanne Baldwin. Thank you for your support and insight from within the wilderness of Vermont!

My experience would be completely different without my graduate peers from the UVM geology department. I will miss working, grading, and complaining with you

all. Special thanks go to Meagan Leduc, for your friend and for keeping me sane. Go buy yourself some Monk of Underhill.

I also would like to thank my friends at Burlington Taiko and UVM Taiko. You all gave me a space to be myself outside of the classroom, and it was fun to grow with you and watch you all grow. I wish I had infinitely more time to spend with you all. Special thanks to Stuart Paton – you taught me many skills that encompassed much more than just playing a drum. I hope to see you all in the future.

Finally, and certainly not least, I would be nowhere without my family. I thank my parents, William and Sandra, and my sister Karmen for being never-endingly supporting. Finally, I owe an enormous amount of gratitude to Christine – thank you for always pushing me to be my best self, even when I didn't want to be. I cannot wait to see what the future holds.

TABLE OF CONTENTS

Contents Page

LIST OF TABLES

Table Page

LIST OF FIGURES

Figure Page

Chapter 1: Introduction

This study examines rocks of northern Vermont (Figure 2-1), specifically the footwall of the Prospect Rock Fault, which are within the Green Mountain Anticlinorium (GMA, Figure 2-2). Rocks exposed in the GMA were deformed and metamorphosed during the Taconic Orogeny, which lasted from ~470–460 Ma (Stanley and Ratcliffe, 1985; Karabinos et al, 1998). East-dipping subduction (present-day coordinates) of oceanic lithosphere in the Iapetus Ocean formed a series of island arcs which ultimately collided with the proto-North American continent, accreting basin and rift sediments, ophiolites, and the island arcs themselves were accreted onto the continental margin as tectonic slices (Stanley and Ratcliffe, 1985; Karabinos et al., 1998).

The Tillotson Peak Complex (TPC) is juxtaposed with the eastern limb of the GMA and is known to preserve blueschist and eclogite-facies rocks that record high-pressure (HP) metamorphism in a subduction zone setting (Laird and Albee, 1981). Recent studies on the TPC in northern Vermont have suggested peak metamorphic pressures of 2.5 GPa, approaching ultrahigh-pressure (UHP) metamorphic conditions (Honsberger, 2015). UHP terranes are subducted to and exhumed from depths of 90–150 km or more (Ernst, 1997; Dobrzhinetskaya, 2011). Over 20 locales have been recognized globally since the discovery of UHP terranes in 1984 (Chopin, 1984; Hacker et al., 2013). Rapid exhumation of HP–UHP terranes must occur, or retrograde deformation and metamorphic reactions may obscure earlier signs of the subduction-exhumation history (Hacker, 2013). Though structural mapping and limited dating studies have been performed on the TPC (Laird et al., 1984; Bothner and Laird, 1999), the timing of peak

metamorphism, exhumation, and kinematics for the TPC have not been examined in depth. However, several studies have examined the Prospect Rock Fault (PRF) (Lamon, 2001; Thompson and Thompson, 2003; Castonguay et al., 2011), which contains the TPC in its footwall.

Interpreting data from $^{40}Ar/^{39}Ar$ dating and microstructural analysis for the PRF and the TPC may impact our current understanding of exhumation models for the TPC, and for the broader local tectonic setting. Contrasting models detailing the evolution of the PRF have been proposed (Lamon 2001; Thompson and Thompson 2003), suggesting different methods of exhumation for the TPC. The presence of the TPC in Vermont affects local tectonic models, as they must account for the conditions needed to produce and preserve a (U)HP terrane. Breakthroughs on an exhumation model may have implications for regional tectonics, as studies have shown that the geology of Vermont, southern Quebec, and other regions of New England represent different structural levels of the Taconic orogeny (Castonaguay et al., 2011).

This study integrates microstructural analysis and $^{40}Ar/^{39}Ar$ geochronology with the goal of constraining the timing of deformation in the footwall of the PRF. It is a companion project with a coeval study of the TPC (Aiken, MS thesis in preparation). Together, these data provide new findings that must be taken into account by exhumation models and provide new insights into the local tectonic history. The following literature review will introduce topics relevant to (U)HP exhumation, the geologic setting of the Green Mountain Anticlinorium, proposed exhumation models utilizing the PRF, and the use of geochronology in Vermont and Canada.

Chapter 2: Literature Review

2.1 Introduction to Ultrahigh-Pressure Terranes

Ultrahigh-pressure (UHP) rocks are formed when continental crust is subducted to depths of 90 km and deeper (Ernst, 1997; Dobrzhinetskaya, 2011), bearing minerals such as coesite and microdiamond formed under these conditions (Chopin, 1984; Smith, 1984). Exhumation of these rocks from depth must occur at tectonic rates, or overprinting of UHP indicator minerals and structures occur (Hacker, 2013). Over 20 UHP terranes have been identified globally (Liou et al., 2004), and many models, both hypothetical and confirmed, have been created to delineate the rapid exhumation of these unique terranes (Hacker et al., 2013 a; Hacker et al., 2013 b; Guilot et al 2009).

Recent studies on the Tillotson Peak Complex (TPC) in north central Vermont (Figure 2-1, 2-2) have suggested peak metamorphic pressures of 2.5 GPa, approaching UHP metamorphic conditions (Honsberger, 2015). Though structural mapping and limited dating studies have been performed on the TPC (Laird and Albee, 1981; Bothner and Laird, 1999), timing of peak metamorphism, exhumation, and kinematics for the TPC have not been examined in depth. However, several studies have examined the Prospect Rock Fault (PRF) (Lamon, 2001; Thompson and Thompson, 2003; Castonguay et al., 2011), which contains the TPC in its footwall as a part of the Green Mountain Anticlinorium (GMA).

The PRF has been described as both the western limit of the Taconic accretionary complex (Thompson and Thompson, 2003), and as a roof-thrust during tectonic wedging

(Lamon, 2001), but studies have not investigated the PRF's role specifically in the exhumation of the TPC, nor have they placed direct quantitative constraints on the timing of deformation. High-strain folds in the TPC are oriented E-W and parallel stretching lineations, which all run orthogonal to regional N-S trending folds associated with the Taconic and Acadian Orogeny (Thompson et al., 1999; Thompson and Thompson, 2003, Figure 2-2). Features found in the footwall of the PRF, and in some locations even the PRF itself, also exhibit E-W trending folds (Thompson et al., 1999; Thompson and Thompson, 2003; Lamon, 2001).

This study aims to constrain the tectonic significance of the PRF and its role in the exhumation of high-pressure rocks of the TPC. Results of this study will aid in constraining an appropriate exhumation model through its investigation of structural features as observed in the field, microstructural indicators of kinematics and temperatures of cooling and deformation, and $^{40}Ar/^{39}Ar$ dating to aid in determining a P-T-t-D gradient along the footwall. This literature review will cover topics integral to this study, including 1) current understanding of UHP exhumation 2) the geologic and tectonic evolution of the GMA, which includes the PRF and the TPC, 3) exhumation models, and their relevance to this study, and 4) a summary of geochronology and its use in this study.

2.2 HP–UHP Terranes and Exhumation

Eclogite facies rocks have been reported since 1822 (Hauy, 1822), and were thought to have undergone subduction to great depths prior to exhumation (Compagnoni

and Maeffo, 1973; Carswell, 1990). With the discovery of coesite in metamorphic rocks by Smith (1984) and Chopin (1984), UHP metamorphism was introduced to the scientific community, demonstrating that continental crust could be subducted to depths of 90km and greater (Figure 2-3). This unusual discovery also lead to the prevailing assumption that UHP rocks must be exhumed at plate tectonic rates in order to avoid metamorphic overprinting, which would erase evidence of minerals formed by metamorphism at these depths (Guillot et al., 2009). Pelitic rocks metamorphosed under eclogite conditions have also been discovered (Compagnoni and Maeffo, 1973; Carswell, 1990). Since the discovery of coesite and microdiamond, over UHP 20 terranes have been identified worldwide (Liou et al., 2004). As of 2009, the oldest UHP unit has been dated at 620 Ma (Caby, 1994; Jahn et al., 2001), and the youngest at ~7 Ma (Monteleone et al., 2007).

UHP metamorphism is associated with subduction zones, as they provide a pathway for exhumation through which rock units can return to the surface without exceeding the temperatures (<800º) associated with UHP terranes (Hacker et al., 2013a). Studies have been hampered by common overprinting that erase structures and minerals formed at depth by UHP metamorphism. As a result, many numerical and theoretical models have been examined to better understand the implications of different exhumation pathways.

Pressure-temperature-time-depth (P-T-t-D) paths are used to investigate conditions experienced by UHP terranes during subduction and exhumation (Duchene et al., 1997). Kinematic analysis and metamorphic dating of HP–UHP rock units help to more precisely constrain the mechanisms of exhumation. Numerical modeling has also

been used to simulate exhumation under specific conditions, creating models that correlate to real world UHP terranes (Hacker et al., 2013a).

Analysis of HP–UHP terranes is hindered by complications inherent to the terranes. Metamorphic rocks frequently have undergone multiple deformational events, making it difficult to date minerals without producing mixed ages. Additionally, isotopic systems are often used to date rock terranes, but these dates record the time of isotopic closure rather than the timing of formation (Rubatto and Hermann, 2001). These problems must be kept in mind while examining terranes.

2.3 General Subduction Models

Guillot et al. (2009) suggest that exhumation events occur during a perturbation to a subduction zone. Disturbances such as a change in subduction velocity, change in subduction angle, or docking of a seamount, arc, or continental block may result in UHP exhumation. As such, UHP exhumation models are dependent on the variables introduced by a given subduction zone. Differences in the subducting protolith, boundary mechanisms, flow pathways, and overall subduction geometry can in turn influence the exhumation velocity, rock buoyancy, boundary forces, and return flow (Guillot et al., 2009).

Based on the examination of more than 60 HP–UHP units, Guillot et al. (2009) has described three different subduction models which are summarized below: accretionary-type subduction, serpentinite-type subduction, and continental-type subduction. The listed subduction types can coexist within a single subduction zone, and

examples of this have been found globally. Type of subduction zone(s) imply different settings that may influence how HP–UHP terrane exhumation occurs.

2.3.1 Accretionary Type Subduction

Accretionary-type subduction zones develop in convergent margins, between intra-oceanic arcs or oceanic-continental convergent. As an oceanic arc subducts beneath a second plate, oceanic sediments are stacked as they are scraped off the subducting plate, forming an accretionary wedge. Accretionary wedges can reach 40–60 km in thickness in extreme cases, though are more typically found to be around 20 km.

The geometry of the accretionary wedge itself depends heavily on the geometry of the non-subducting plate, which acts as a backstop against which the wedge pushes against and forms. Numerical models have shown how the wedge shape and metamorphic pressures within it are altered depending on the shape of the backstop (Beaumont et al., 1999; Yamato et al., 2007). This geometry affects how deeply sediments can be subducted, and how likely subducted sediments could return to the surface to be exhumed. More than 20 HP–UHP massifs globally have been identified as having formed through this style of subduction (Tsujimori et al., 2006; Agard et al., 2008). Accretionary type subduction is more heavily associated with HP exhumation (Guillot et al., 2009).

2.3.2 Serpentinite-Type Subduction Complexes

Serpentinites are frequently found with HP-LT rocks, and have been interpreted as parts of oceanic lithosphere. Examinations from 18 serpentinite–type subduction

complexes suggest origins from subducted oceanic plates, though an exception exists as a serpentinite diapir found in the Izu-Bonin Arc (Ueda et al., 2004). Initial geometries of serpentinite-type subduction complexes are difficult to understand, as contacts between serpentinized units are generally unrecognizable. However, serpentine mineral properties cause them to be highly ductile, and act as lubricants on subduction planes.

Serpentine minerals can contain up to 13 wt% water, and host fluid mobile elements in deep subduction zones (Schmidt and Poli, 1998; Hattori and Guillot, 2007). They are stable down to depths of 150–170km (Ulmer and Trommsdorf), and have low density (2600 kg/m^3) and low viscosity (4.10^{19} Pas), a high poisson ratio, and a low shear modulus (Moore and Lockner, 2007; Reynard et al., 2007; Hilariret et al., 2007). With these properties serpentines are highly ductile at shallow depths, allowing easier exhumation by acting as a lubricant between the two subduction planes (Guillot et al, 2001).

Calculated exhumation velocities in serpentinite-type subduction complexes have varied between 3 to 10 mm yr^{-1}. Exhumed units are highly dominated by sheared serpentinites, with additional rock units contained within. Deformed units can vary from kilometers to centimeters in size. Studies on exhumed eclogite blocks in these types of subduction complexes have shown pressures of between 1.8–2.5 GPa, with a few locales with higher pressures of 3.2 and 4.0 GPa.

2.3.3 Continental Type Subduction

Continental type subduction occurs with the subduction of continental crust down to depths of over 90 km. The discovery of coesite indicated to the scientific

community that subduction of continental crust was a possibility (Chopin, 1984; Smith, 1984). During subduction of continental crust, positive buoyancy and thickness prevent the entirety of the lithosphere from entering the subduction zone. Buoyancy of subducted continental crust relative to the mantle when subducted also aids in the terrane's exhumation from depth (Chemenda et al., 1995; Ernst, 2006).

In the Himalayas, subducting continental lithosphere has been shown to separate from itself and stack as nappes, building the high topography of the Himalayas (Guillot et al., 2003). UHP rocks from continental style subduction are mostly granite gneiss and metasedimentary rocks in origins, with some mafic plutons from intrusions prior to subduction. Exhumed terrane sizes vary wildly in size, ranging from 25km^2 to over 50,000km^2. Exhumation velocities are estimated to be faster than 6 mm yr^{-1}.

UHP minerals are only locally preserved in continental type subduction, and evidence of these conditions are found locally in lenses or as relics in other minerals. Regardless, their presence indicates that rapid exhumation, rapid cooling during decompression, and little deformation must have occurred during exhumation, in addition to fluid absent conditions.

2.4 Ultrahigh-Pressure Exhumation Models

As noted above, the formation of UHP terranes require the subduction of a protolith to great depths in a subduction zone, and rapid return of the terrane back to the surface. Various UHP terrane exhumation models have been proposed, but can vary

greatly due to the variables that control exhumation details, such as tectonic settings and buoyancy.

Plate tectonics lay a foundation for each exhumation model, creating collisional regimes, subducting proto-UHP terranes, and creating a geometric framework utilized during exhumation. Colliding plates allow for the proto-UHP terranes to be subducted down to depths sufficient for UHP metamorphism. Once there, the geometry of the subduction zone can influence material flow and flow pathways within the subduction channel. Steep subduction angles are also necessary to subduct and exhume terranes to depths necessary for their formation (Guillot et al., 2009). Exhumation can be greatly enhanced by initial geometry (Guillot et al., 2009), as gentle subduction angles may prevent subduction and exhumation to and from appropriate depths (Guillot et al., 2008), whereas steeper angles may allow for subduction to depths of 200–300 km (Negredo et al., 2007).

Buoyancy is also a driving force in exhumation, as it brings subducted terranes back to the surface through the subduction channel. Buoyancy can be determined by the lithology of the subducted terrane, when compared to its surrounding materials. Phase transformations due to pressure and temperature changes attending subduction and exhumation impact buoyancy (Hacker et al., 2013b).

A weak subduction channel may also be necessary in some models to aid for exhumation. Models examining the exhumation of continental rocks rely less heavily on a weak subduction channel, as buoyancy of continental rocks can be considered sufficient for their exhumation (Chemenda et al., 1995, Ernst 2006). Subducting slabs during

progressive metamorphism can release fluids, facilitating the lubrication of subduction planes. Release of fluids can also aid in the formation of weak metamorphic minerals, such as lawsonite and phengite (Stockert and Renner, 1998). High strain shear zones can form using these weak minerals, and can surround and preserve pockets of HP/UHP mineral assemblages during exhumation. Models by Gorczyk et al. (2007) indicate that hydration of the mantle wedge can ultimately lead to slab retreat and exhumation of UHP mafic rocks subducted to depths of 100-150kms.

Comparison of different exhumation models can aid in evaluating the exhumational and tectonic history of a given terrane. P-T-t-D paths within a model imply patterns that should appear in the structural geology, petrology, and geochronology of an exhumed rock terrane. Field structures, microstructures, bulk composition, and ages for a given terrane can help in understanding a locale's tectonic history.

2.4.1 Chemenda Model

The Chemenda Model, from Chemenda et al. (1995) demonstrates the subduction and exhumation of a large, coherent crustal slice, and remains a frequently utilized exhumation model for UHP terranes (Hacker et al., 2013; Figure 2-4). Continental lithosphere is subducted to depth in the subduction zone, where its buoyancy creates large deviatoric stresses that causes brittle or plastic failure. The continental slab detaches from the subducting lithosphere, where it is bound by a thrust fault below and a normal fault above it. The slab is thrust towards the surface along a shear zone. The exhumation of this slice can be extremely rapid, within 0.2 My (Sizova et al., 2012).

2.4.2 Serpentine Channel

As mentioned above, serpentine channel exhumation is a recognized mechanism that can exhume UHP rocks to the surface, as recognized in the Himalayas, Mariana forearc, and the Alps (Guillot et al., 2000; Fryer et al., 1999; Guillot et al, 2009). UHP rocks are frequently spatially associated with serpentinites and hydrated peridotites, both of which can be associated with dewatering of a hydrated mantle (Guillot et al., 2000). At depth, serpentines can act as a lubricant along the subduction plane, aiding in the rapid exhumation of a UHP block along subduction planes (Figure 2-5). They can play an analogous role to hydrated sediments in a subduction zone at shallow depths. The buoyancy of serpentinite is also thought to be able to aid in exhumation of rocks from depth.

2.4.3 Eduction Model

The eduction model was named and proposed by Andersen et al. (1991), when lack of contractional structures in the Western Gneiss Region of Norway lead to the need for a new model. Their proposed model brought UHP rocks to the surface through the reversal of relative motion between two plates (Figure 2-6). In Andersen et al. (1991), the subducting slab breaks off, which results in continental margin rebound. The subducting slab is no longer driving subduction and reverses, creating extensional structures. UHP rocks are exhumed to the surface through rebound, buoyancy, and the removal of overburden by extensional structures. Exhumation can be accompanied by an along strike

gradient in peak pressures, and formation of motion parallel stretching lineations (Hacker et al., 2013; Webb et al., 2008).

2.4.4 Diapiric Rise

Diapiric rise was proposed as an exhumation model for UHP terranes by Gerya and Stockhert (2006) for rocks in the Alps. Sediment or rock is subducted to UHP metamorphic depths, and there can aggregate as diapirs and rise through the overlying mantle (Figure 2-7). Currie et al. (2007) and Yin et al. (2007) showed that crustal rocks at depth could rise diapirically through the mantle wedge and not experience melting or assimilation into the wedge. The rising diapir can relaminate the base of the upper plate, after changes in chemical and physical properties (Hacker et al., 2013).

2.5 Regional Tectonics and Geologic Overview

Vermont's geology can be more clearly interpreted through an understanding of its tectonic history, which stretches more than one billion years into the past. Sections of Vermont's geology are linked to the formation of Rodinia supercontinent, and its rifting to create Laurentia (Proto North-American continent), Gondwana, and the Iapetus Ocean (Ratcliffe et al., 1991; Mclellan et al., 2010, Cawood et al., 2001b). Laurentia underwent collisions with island arcs, a continental margin, and a microcontinent, in addition to experiencing extensional regimes, as part of the Taconic, Salinic, and Acadian Orogenies (van Staal and Barr, 2012).

2.5.1 Vermont Geology and Tectonic History

The geology of Vermont can be subdivided in six lithotectonic slices, with each slice representing a different period in Vermont's tectonic history (Stanley and Ratcliffe, 1985). These slices include the Grenvillian Basement, the Carbonate Platform, the Taconic Allochthon, the Green Mountain Slice, the Rowe Hawley Belt, and the Connecticut Valley Gaspé Trough (Figure 2-2). Everything from the rock types found in each province to the smallest microstructures found in in samples has been influenced by its tectonic history.

Rocks associated with the Grenvillian Basement can be found in southern Vermont. Rocks within this province are interpreted as exposures of North American continental crust (representing Rodinia), which are much older than the rocks of the Green Mountains. Sections of Vermont's basement rocks are dated to have formed at ages up to 1.35 Ga as a part of the Grenville orogeny (Ratcliffe et al., 1991; Mclellan et al., 2010). Mineral and whole-rock dates of these basement rocks exceed 900 Ma. Basement rocks are typically granitic gneiss, and are unconformably overlain by clastic sequences. (Naylor, 1976; Stanley and Ratcliffe, 1985).

Rocks found in Vermont's Carbonate Platform are related to early rifting of Rodinia. Iapetan rifting commenced ca. 570 with separation of Rodinia into Gondwana and Laurentia. A second rifting phase of further blocks off Laurentia occurred from ca. 540–535 Ma, establishing a passive margin sequence that can be recognized throughout the Appalachians. Extension and rifting was also accompanied by magmatic activity, manifest in dikes and plutons (Cawood et al., 2001 a). The creation of a passive margin,

followed by a foreland basin allowed for the accumulation of carbonate sediments. These sediments would the marbles and dolomites of the carbonate platform (Cawood et al., 2001 b; Rodgers 1968).

Rocks associated with the Taconic Allochthons, the Green Mountain Slice, and the Rowe-Hawley Belt are interpreted to have been deformed during the Taconic Orogeny. During this event, oceanic sediments were scraped up and accreted onto the Laurentian Margin due to the collision between the Laurentian Continent and an incoming island arc, lasting from between ~470–460 Ma (Stanley and Ratcliffe, 1985; Karabinos et al, 1998).

Rocks in the Connecticut Valley Gaspé Trough (CVGT) are associated with a period of extensional tectonics that occurred after the Taconic orogeny. Like with the formation of the Carbonate Platform, extension lead to thinning of the lithosphere, subsidence, and the formation of basins. These factors encouraged the flow of sediments into the low basin areas during rifting, eventually lithifying into sedimentary and meta-sedimentary rocks (Hepburn, 1991; Slack, 1994; Karabinos, 1998; Karabinos and others, 1998; Slack and others, 2001).

The rocks in Vermont are also affected by a later mountain building event called the Acadian orogeny. Evidence of volcanic activity is present in eastern Vermont and New Hampshire suggesting that subduction after the Taconic orogeny had continued to the east (Rankin et al., 2007). After the oceanic crust of the Iapetus ocean was consumed by subduction, the Laurentian continent collided with the Avalonian microcontinent (van Staal and Barr, 2012). This collision is interpreted to have deformed and/or reactivated

pre-existing structures, such as the folding of the Burgess Branch Fault Zone (Kim et al., 2003). This event is associated with much of the north-south trending structures in Vermont.

2.5.2 The Taconic Orogeny, Extension, and the Acadian Orogeny.

One of Vermont's defining features, its multitude of mountains, are attributed to the Taconic Orogeny and the Acadian Orogeny as mentioned above. The first of the two orogenies is documented as a collision between the Laurentian continent and the Shelburne Falls island arc (Karabinos et al., 1998).

Off the coast of Laurentia, the formation of an east dipping subduction zone (relative to present day coordinates) began the closure of the Iapetus ocean (Figure 2-8). Lithosphere consumed by the subduction zone was subducted to depth, generating magma that would create both the Shelburne Falls island arc and ophiolites on the overriding plate (Karabinos et al.,1998). As subduction continued, the Shelburne Falls island arc would ultimately collide with the Laurentian continent, thrusting oceanic terranes, ophiolites, and island arc sediments onto the continent (Kim et al., 2003, Figure 2-9). $^{40}Ar/^{39}Ar$ ages from rocks on the Laurentian margin related to Taconian metamorphism in southern Quebec, Vermont, and western Massachusetts have been dated from 470 to 460 Ma (Laird et al 1984; Sutter et al., 1985; Hames and Hodges, 1993; Castonguay et al., 1997).

After the Taconic collision, the Laurentian margin experienced a period of extension. Listric block faulting and normal faulting, along with eustatic sea-level fall, created basins where sediments could accumulate (Bourque et al., 2001; William et al.,

1988, Figure 2-11). The Connecticut Valley Gaspé Trough (CVGT) is one of many Silurian basins formed during this period of extension (Tremblay and Pinet, 2005). Sediments in the CVGT are thought to be eroded remnants of the Shelburne Falls arc and the Bronson Hill arc, which were located to the west and east of the trough respectively (Karabinos et al 1998; Stanley and Ratcliffe, 1985). Detrital zircon ages from McWilliams et al. (2010) suggest that depositional environments existed near the CVGT from before 423 Ma to at least 409 ± 5 Ma. Igneous rocks associated with Silurian extension can also be found in and around the CVGT trough (Rankin et al 2007).

Several models have been created to explain the period of extension following the Taconic Orogeny. Kim et al. (2003) summarizes several of these models, and posits that models must have a mechanism for the emplacement of boninites onto the Laurentian Continent, and the creation of an extensional regime before collision with an island arc. In Kim et al.'s (2003) preferred model, ophiolites were obducted onto the Laurentian margin before extension begins. Subduction of continental crust down the east dipping subduction zone effectively "jammed" the pathway, causing thrusting and collisional delamination of the subducted lithosphere. Breakthrough of a new west-dipping subduction zone then occurred, transforming the forearc into a backarc.

After a period of extension and sediment deposition, the CVGT experienced loading and metamorphism during the Acadian orogeny. The collision of Laurentia and the microcontinent Avalonia causes the emplacement of westward thrust sheets from Bronson Hill Arc and central Maine over the CVGT (McWilliams et al., 2010).

Subduction of the oceanic crust between Laurentia and Avalonia ultimately consumed the Iapetus Ocean (Doolan, 1996, Figure 2-11).

2.5.3 Salinic Orogeny

The Salinic Orogeny, an event still debated in New England, is thought to have occurred between the Taconic Orogeny and the Acadian Orogeny. Evidence for this tectonic event has been recognized in parts of the northern Appalachians, including in Newfoundland (van Staal et al., 2009), New Brunswick (van Staal and de Roo, 1995), and Maine (West et al., 1992; Hibbard 1994). Studies in central New England have shown little to no evidence for a Salinic age collisional event thus far (Rankin et al., 2007). $^{40}Ar/^{39}Ar$ ages from southern Quebec range between 433 to 405 Ma (Castonguay et al., 2001, 2007), but early Salinic deformation is thought to have begun from 440-435 Ma in southern Quebec (Castonguay et al., 2001, 2007; Tremblay and Pinet 2016). These dates overlap with ages for the formation of the CVGT (see subsection below).

The most widely accepted model for the Salinic Orogeny continues from the events of the Taconic Orogeny with the closure of the Iapetus Ocean. The east-dipping subduction zone (southeast-dipping in literature from southern Quebec) experienced slab breakoff beneath a collision thickened arc. Further to the east of Laurentia, a west (northwest in southern Quebec) dipping subduction zone formed, continuing to consume the Iapetus Ocean (van Staal et al., 2007). Ultimately, the collision between Laurentia and the Gander Margin lead to the mid-Silurian Salinic Orogeny (430–422 Ma, van Staal and Barr, 2012, Figure 2-10). Post collision, crustal scale extension from asthenospheric upwelling caused the formation of normal faults and troughs (Tremblay and Pinet, 2016).

Many of the papers detailing the Salinic Orogeny have described it in terms of events as documented in the Quebec Appalachians, and denote it as a D_3 tectonic event (Kim et al., 2011). More recent papers have recognized two phases of to the Salinic Orogeny, denoted as D_{3a} and D_{3b} (Tremblay and Pinet, 2016). This paper will denote these two phases simply as phase 1 and phase 2, as the tectonometamorphic events are recorded differently between southern Quebec and Vermont.

2.5.3.1 The Salinic Orogeny: Phase 1

Phase 1, as documented in Quebec, is not linked to intense metamorphism and regional deformation. Rather, phase 1 is a compressional deformational event characterized by hinterland directed structures that are younger than deformation features found in the Taconic Orogeny (Tremblay and Pinet, 2016, Figure 2-10).

Northwest directed hinterland folds, backthrusts, and retrograde metamorphism recorded in southern Quebec stand as evidence to the Salinic Orogeny. These structures may be kinematically linked to the west dipping subduction zone formed east of Laurentia (Oldow et al., 1990; Mazotti and Hyndman, 2002). Southeast directed retroshears and backfolds are proposed to be associated with thick skin thrusting of tectonic slices of Grenvillian basement rocks (Pinet et al., 1996), deformed in the Middle to Late Ordivician and exposed at Green Mountain Anticlinorium of northern Vermont. The Sutton - Notre Dame Mountains in southern Quebec anticlinorium represents an up-plunge version of the GMA. Continental and oceanic material subducted and accreted in Taconic orogeny were transported to the southeast in the hanging wall of backthrusts, locally exhuming to the surface. This may account for Ordovician eclogite and blueschist

facies found at the Tillotson Peak Complex in northern Vermont (Tremblay and Pinet, 2016).

Timing constraints for phase 1 from $^{40}Ar/^{39}Ar$ dating are abundant in southern Quebec. Low temperature steps of apparent-age spectra of retrograde amphiboles and biotites range from 429–424 Ma and 420–411 Ma respectively. Muscovite plateau ages range from 433–405 Ma, reflecting presence of mixed mineral phases from progressive deformation. These muscovite age spectra show an irregular younging from northwest to southeast across Sutton-Notre Dame Mountain anticlinorium (Castonguay et al., 2001, 2007). Tremblay and Pinet (2016) suggest that early Salinic deformation started around 440–435 Ma. Dates in southern Quebec are thought to be younger than those of correlative structures in western New England, based on muscovite ages yielded from correlative structures (Castonguay et al., 2012).

2.5.3.2 The Salinic Orogeny: Phase 2

Phase 2 of the Salinic Orogeny is associated with extensional tectonics. After the collision between Laurentia and Ganderia, asthenospheric upwelling due to slab delamination and/or trench retreat of the subduction zone is thought to have created crustal-scale extension (Tremblay and Pinet, 2016, Figure 2-11). This extension lead to the formation of normal faults, half-grabens, and graben and horst formations (Tremblay and Pinet, 2005).

Extension during the Salinic Orogeny has been documented along the whole length of the Quebec Appalachians, and is linked to the formation of the Connecticut Valley-Gaspé Trough and the Merrimack Valley Trough in Quebec and New England.

South and southeast dipping normal faults in Quebec are correlated to phase 2, though poorly documented in some areas due to reactivation of normal faults during the Acadian Orogeny (Tremblay and Pinet, 2016). Studies have showed conclusive evidence for extensional movement during the Silurian, as seismic data from Pinet (2013) reveals a 3.8 km normal sense vertical separation between Silurian units on both sides of a fault.

In southern Quebec, phase 2 structures correspond to structures in the Gaspé Peninsula, western New England, and northwest Maine (Kim et al., 1999; Tremblay and Pinet, 2005). Correlative normal faults found in these regions are characterized by moderately to steeply dipping shear bands, and brittle–ductile normal sense shear zones, pointing to a top to the east sense of motion (Pinet et al., 1996; Tremblay and Pinet, 2005; Perrot, 2014). The amount of displacement along these structures is not constrained, but correlative faults separate high to medium grade rocks in the hanging wall from less metamorphosed rocks in the footwall (Castonguay and Tremblay, 2003; Tremblay and Pinet, 2005).

Much of the timing constraints for phase 2 extensional events involve the interpretation of 2D seismic lines. Growth strata indicate that syn-sedimentary normal faulting or transtensional faulting mainly occurred during the late Silurian to early Devonian in the Gaspé Peninsula (Pinet, 2013). $^{40}Ar/^{39}Ar$ data from hanging wall of the St. Joseph fault in southern Quebec (420-410 Ma) is contemporaneous with brittle fault activity in Gaspé Peninsula, and likely records progressive exhumation in response to extension (Castonguay et al., 2007).

2.5.3.3 The Salinic Orogeny and Vermont

Some authors have found evidence for a mountain building event in between the Taconic and Acadian, (Castonguay et al., 2011), whereas others have explicitly noted a lack of intervening compressional regimes (Rankin et al., 2007). Castonguay et al. (2011) utilized $^{40}Ar/^{39}Ar$ dates to correlate a third tectonic event in the GMA to Silurian deformation, in the same time frame as the Salinic Orogeny. Rankin et al. (2007) argues that despite Silurian metamorphism and compressional regimes found in Newfoundland, New Brunswick, Cape Breton Islands, there is no evidence for Silurian compression in CVGT, making it hard to reconcile compression with extension. The existence of a period of extension (phase two as described above) between the Taconic and Acadian Orogenies is widely accepted in Vermont. Detrital zircon ages from the CVGT in Vermont (McWilliams et al., 2010) and late Silurian normal faulting are associated extension must have occurred to create the CVGT and other correlative structures in New England and Quebec.

2.6 Regional Geology

The collision between the island arcs with the Laurentian continent, or the Taconic Orogeny, lasted from about 470 to 460 Ma (Castonguay et al., 2011), and accreted rift and basin sediments, ophiolites, and island arcs onto Laurentia as slices. These units were thrust onto Laurentia as part of a foreland-propagating thrust system (St-Julien and Hubert, 1975; Sasseville et al., 2008; van Staal et al., 2009). Evidence of Taconic Orogeny can be found in N–S trending metamorphic slices recognized in modern

day Vermont and Quebec. Several of these slices are included within the Green Mountain Anticlinorium, which is a part of the Green Mountain Slice and borders the Rowe Hawley Belt.

2.6.1 Lithology of the Green Mountain Anticlinorium

The Prospect Rock Fault (PRF) is mapped within the Green Mountain Anticlinorium (GMA, Figure 2-2). Rocks in the footwall are noted as part of the Green Mountain Slice, and are composed internally of the Fayston Formation and the Hazens Notch Formation. These formations have been interpreted to represent metamorphosed rift clastics and slope-rise deposits from the rift-drift transition prior to the Taconic orogeny (Thompson and Thompson, 2003). The Fayston Formation consists of schist with high mica and chlorite content, with garnet, magnetite, and albite porphyroblasts (Cady et al., 1963). The Hazens Notch Formation contains graphitic schist with albite, with or without chlorite, garnet, and pyrite. It also contains discontinuous quartzites, greenstones, and localized bodies of ultramafics and talc-carbonate bodies (Cady et al., 1963). Rocks in the hanging wall of the PRF have been noted to contain more albite than those found in the footwall (Lamon, 2003).

Rocks in the hanging wall of the PRF are a part of the Prospect Rock Slice, mapped as the Jay Peak and Ottauquechee Formations. The Jay Peak Formation contains includes phyllite and schist, with or without magnetite, garnet, chloritoid, and albite. White quartzite and rare greenstone can also be found in the unit. The Ottauquechee Formation contains non-albitic, graphitic quartzose phyllite and schist, discontinuous quartzite beds, and local lenses of non-graphitic phyllite (Cady et al., 1963).

On the eastern limb of the GMA, the Tillotson Peak Complex is surrounded core rocks of the Hazens Notch Formation, and contains blueschist, eclogite, and small ultramafic lenses within the Haystack Tillotson Slice (Laird and Albee, 1981; Bothner and Laird, 1999, 1987). The surrounding Hazens Notch Formation is split into two regions of mafic schist and felsic gneiss. Isolated serpentine lenses are found along the contact of the Hazens Notch Formation, and contain strongly sheared serpentinite. Blueschist and eclogite of the TPC are fine to medium grained (Laird and Albee, 1981).

2.6.2 Structures of the Green Mountain Anticlinorium

Structures in the GMA have been linked to the two dominant orogenies of Vermont: the Taconic and the Acadian orogenies. Three stages of deformation have been identified in the GMA, with D_1 and D_2 associated with the Taconic Orogeny, and D_3 linked to the Acadian. A study by Castonguay et al. (2011) has suggested that the D_3 phase could possibly be instead attributed to Salinic deformation, but most other literature has described D_3 as Acadian. Foliations, lineations, and folds of the GMA have been well documented and described, though vary by location due to a multideformational history. Recent studies in the Tillotson Peak Complex, found on the eastern limb of the GMA, recognize four deformational events (Aiken, MS thesis, in prep.) which may aid in reconciling the discrepancies between southern Quebec and Vermont structures, as noted above. Structures will be described in terms of these four deformational events, though previous studies have utilized three.

2.6.2.1 Foliations of the Green Mountain Anticlinorium

Three sets of foliation are present in the GMA, not including bedding (S_0). Occurrences of S_0 are rare, and typically appear transposed by later foliations (Kim et al., 1999). Distinguishing between foliations in the field can be challenging, as different combinations of foliations can be found as composite foliations. Nonetheless, general trends in the foliations can be described and recognized.

In the GMA, S_1 foliations are generally not well preserved, and are most easily observed in quartzite beds. S_1 can be found locally as compositional layering, axial planar to rootless isoclinal F_1 folds (Castonguay et al., 2011). S_1 is often found parallel to S_2, and is difficult to distinguish from S_2 other than in D_2 fold hinges (Thompson et al., 1999). In other areas, S_1 is folded by a second generation of transposed isoclinal folds with an axial planar spaced cleavage, representing S_2 (Castonguay et al., 2011). S_1 is associated with the Taconic Orogeny (Thompson and Thompson, 2003).

S_2 foliations are associated with peak metamorphism during the Taconic orogeny (Thompson et al., 1999). S_2 foliations are defined by axial planar spaced cleavage (Castonguay et al., 2011). Dip direction of S_2 varies over the GMA, dipping southeast on the eastern limb of the GMA and curving towards the southwest traveling west over the GMA (Thompson and Thomspon, 2003).

S_3 foliations have been interpreted to be associated with the Acadian orogeny and the folding of the GMA. The overall trend of the anticlinorium is 015º (Thompson et al., 1999). Foliations are generally defined as spaced cleavage or a crenulation cleavage, and

are parallel to axial planes of F_3 folds. In some areas, such as east of the Burgess Branch Fault Zone, S_2 and S_3 can form a composite foliation (Kim et al., 1999).

2.6.2.2 Lineations of the Green Mountain Anticlinorium

Lineations in the GMA are grouped into L_2 or L_3. L_2 lineations are defined by the long axes of minerals, stretching lineations or quartz rods, and plunge parallel to F_2 fold axes. Near the Lamoille River, L_2 structures trend roughly east and west across the anticlinorium. South of the Lamoille river, older quartz lineations remain east-west, whereas younger structures gradually shift in orientation. Stretching lineations have been interpreted as parallel to transport direction during deformation (Thompson and Thompson, 2003; Thompson et al., 1999).

L_3 lineations are found as intersection or crenulation lineations. These may overprint L_2 quartz rod lineations (Kim et al., 1999). L_3 lineations run parallel to F_3 fold hinges, and plunge gently north or south (Thompson, et al., 1999).

2.6.2.3 Folds of the Green Mountain Anticlinorium

Structures associated with D_1 are generally poorly preserved and hard to find. F_1 and F_2 folds are often difficult to distinguish, especially when axial planes and fold axes are sub-parallel. F_1 folds are generally isoclinal, with fold axes trending east-west. Folds are observed with disarticulated hinges and sheared out limbs (Thompson et al., 1999). Despite S_1 and S_2 commonly appearing parallel, F_1 and F_2 fold axes are not coaxial (Kim et al., 1999).

F_2 folds are tight, isoclinal, and fold an earlier foliation (S_1). Fold axial planes parallel the dominant S_2 foliation. Close to the Lamoille River, F_2 fold hinges trend roughly E–W across the anticlinorium, though trending more towards NE–SW on the eastern side of the GMA, and more northwest-southeast on the western side (Thompson et al., 1999; Thompson and Thompson, 2003). Due to the rarity of F_1 folds, and the subparallel nature between F_1 and F_2, folds are generally assumed to be F_2 when a clear distinction cannot be made.

F_3 folds have been linked in the literature with the folding of the GMA and the Acadian Orogeny. The fold axis trends about 015º (NNE), though it varies between locations. F_3 folds are generally open and upright, asymmetric (Kim et al., 2003), and fold the dominant foliation (S_2). Axial planes are steeply dipping. F_3 folds are common throughout the GMA, and can plunge gently north to gently south (Thompson et al., 1999).

2.6.3 Structures of the Tillotson Peak Complex

Previous studies have also identified three distinct deformational events (Bothner and Laird, 1987). S_1 is the dominant foliation in the field, and is axial planar to isoclinal folds preserved in mafic schist. It is primarily defined by minerals associated with blueschist and greenschist facies mineral assemblages. S_1 has also been refolded, creating approximately E–W F_2 folds that can be seen on map scale. S_2 appears as a spaced crenulation cleavage best developed in the mafic schist, though it also appears in the felsic gneiss (Bothner and Laird, 1987). The S_3 foliation is approximately axial planar to F_3 folding.

Three generations of folds have been identified in the field or from field samples. F_1 folds are small, isoclinal, recumbent folds axial planar to S_1. F_2 folds are gentle to open folds, nearly reclined, and generally E-W trending. These folds can be identified on map view of the Tillotson Peak Complex. F_3 are inferred to be represented by the Gilmore Antiform, and is a broad, open macroscopic antiform that can be noted on map scale (Figure 2-2). Earlier studies (Bothner and Laird, 1987) noted that no mesoscopic structures have been tied to F_2 folding, but trends of plunges of F_2 fold axes over the TPC appear to be altered by F_3.

A recent study by Aiken (MS thesis, in prep) on the TPC identified four generations of foliations and folds. S_1 foliations are documented in microstructural examinations, and are preserved locally in garnet and albite porphyroblasts, as well as in F_2 fold hinges. S_2, S_3, and S_4 correspond to foliations from prior studies (S_{1-3}). The study also identifies four generations of folds, with F_1 folds inferred to be locally absent or transposed and axial planar to F_2 in the field area. F_{2-4} correspond to F_{1-3} as noted above. Furthermore, F_3 and F_4 folds have been identified in hand samples from this study.

2.6.4 The Prospect Rock Fault

The Prospect Rock Fault was discovered by mapping rock units near the Prospect Rock in Jeffersonville, Vermont (Thompson, 1998). Phyllites of Ottauquechee and Jay Peak Formation were identified as units of the hanging wall, which overlay coarse albitic schists of the Hazens Notch and Fayston formation in the footwall. One exception exists in a small overturned limb of a fold west of the prospect rock. The Prospect Rock Fault is folded by the GMA, matching F_4 folds identified in the region (Figure 2-12). The PRF

generally dips towards the east, except where it passes through fold hinges. The fault also dipps more steeply to the southeast on the short F_3 limb than on the long limb.

Sense of motion of the Prospect Rock Fault is debated. Lamon (2001) suggested transport of the hanging wall to the east, based on microstructural kinematic and strain indicators. Thompson and Thompson (2003) suggest that initial fault movement was directed westward, and later eastward normal reactivation may have occurred during the Acadian. Different models discussing the movement of the Prospect Rock Fault, and its role in the exhumation of the Tillotson Peak Complex are further discussed below.

2.7 Exhumation Models and the Tillotson Peak Complex

The presence of the Tillotson Peak Complex (TPC) in Vermont has had a strong effect on regional tectonic models, as new models must have an explanation for how this high-pressure metamorphic terrane was exhumed to the surface. Studies have utilized data from the PRF and the associated core and cover rocks to analyze the fault's role in the obduction of Taconian orogenic rocks and the TPC with varying interpretations.

The TPC has several structural features that must be reconciled within an exhumational model. First, previous studies have suggested peak metamorphic pressures of 2.5 GPa, approaching UHP metamorphic conditions (Honsberger, 2015). Rapid exhumation of the terrane must have occurred, or retrograde deformation would have obscured pre-existing high-pressure assemblages (Hacker, 2013). Second, high-strain folds in the TPC are oriented E-W and parallel stretching lineations, which all run orthogonal to regional N-S trending folds associated with the Taconic Orogeny

(Thompson et al., 1999; Thompson and Thompson, 2003). These features are also found in the footwall of the PRF, and in some locations even the PRF itself, also exhibit E-W trending folds (Thompson et al., 1999; Thompson and Thompson, 2003; Lamon, 2001, Figure 2-2). Finally, Lamon (2001) suggested an overall top-to-the-east sense of movement of the PRF, based on microstructural kinematic indicators from near the Prospect Rock area.

Two models have been proposed for the evolution of the PRF, and its role in the exhumation of the TPC. Lamon (2001) suggested that the PRF was formed as an east directed roof thrust during tectonic wedging, and that the TPC was a part of the westward thrust slice thrust onto the Laurentia (Figure 2-13). Thompson and Thompson (2003) suggested that the PRF represents the basal thrust of the Taconic accretionary prism, which was thrust west onto the Laurentian continent (Figure 2-14). This chapter will also examine the eduction model and its possible application to the PRF and the TPC. Details on this model are informed by Webb et al. (2008, Figure 2-15).

2.7.1 Tectonic Wedging Model

Lamon (2001) describes the PRF as a roof thrust formed as a part of tectonic wedging during orogenesis (Figure 2-13). Petrologic analysis of rock in the foot wall revealed a metamorphic gradient along the footwall, increasing from west to east. Thin section observations of the albitic foot wall rock also showed a top-to-the-east shear sense. Fine-grained cover rocks (PRF hanging wall) were interpreted as having undergone low-grade metamorphism, as opposed to the core rocks (PRF foot wall) which underwent higher grade metamorphism. The metamorphic gradient, combined with the-

top-to-the-east shear sense, were interpreted by Lamon to support emplacement of a wedge, where the "inserted" rocks of the PRF footwall were thrust to the west under the low grade hanging wall rocks which moved eastward. These wedge rocks represent fault bounded slices assembled prior or during wedging within the subduction zone. Under this model, the PRF represents the roof thrust of the emplaced wedge of high-grade rocks.

The addition of the TPC to the wedge is addressed by underplating, combined with normal faulting to later expose the terrane. Rocks of the TPC were added to the base of the wedge through underplating, while the wedge was actively thrust towards the surface. The Burgess Branch Fault Zone is interpreted in this case to be a steep extension of the PRF in this model, which aided in the rapid ascent of the TPC to the surface. Foreland directed normal faulting above the TPC helped to exhume the complex by removing overburden and exposing higher grade rocks. This E–W oriented extension could be linked to the creation of extension parallel structures, such as lineations and folds.

2.7.2 Basal Thrust Model

Studies have utilized data from the PRF and the associated core and cover rocks to analyze the fault's role in the obduction of Taconian orogenic rocks with varying interpretations. Thompson and Thompson (2003) interpreted the PRF as the basal thrust of the Taconian accretionary prism (Figure 2-14). Under their description, east-directed subduction along the Laurentian Margin basin created an accretionary prism, which rode up onto the Laurentian continent. Thrusting along the PRF emplaced the prism above the autochthonous footwall rocks. The accretionary prism, which includes the Stowe and

Ottauquechee Formations of the hanging wall, grew through underplating as it was thrust to the west.

As thicker, buoyant Laurentian crust was pulled towards the east dipping subduction zone by subduction, the rate of subduction decreased and material was ejected from the accretionary prism. Aided by deformation of weak serpentinized ultramafics along their boundaries, exhumed blocks could move rapidly over a significant distance. In this manner, the TPC could have been rapidly exhumed and avoid overprinting of UHP structures.

In this model, E–W verging folds and structures formed during a later deformational event during the Taconic Orogeny. The Champlain Thrust Slice, an underlying slice stratigraphically far below the GMS, is described to have moved westward during this later event. Thrusting may have passed over the Grenvillian basement, causing the slices to encounter ancient normal faults at rift basin margins. As the slices moved, material above them splayed out in two directions, forming west verging folds in western Vermont, and east verging folds and back thrusts above and east of the deep ancient faults.

The results of Lamon's study (2001) recognizing eastward motion along the PRF is recognized by Thompson and Thompson (2003), though their model argues for overall westward motion along the PRF. They attribute eastward motion noted by Lamon (2001) to later fault reactivation during a later deformation stage.

2.7.3 Subduction Zone Reversal

Exhumation models for the TPC must be reconciled with rapid exhumation of the terrane, E–W trending structural features orthogonal to dominant Taconic structures, and top-to-the-east motion along the PRF as observed through kinematics. UHP terranes in Papua New Guinea and China have been recognized with similar characteristics: rapid exhumation of an ~8 Ma HP–UHP terrane (Baldwin et al., 2008), and structural features that are non-parallel to the direction of convergence (Hacker et al., 2000, Little et al., 2007, Daczko et al., 2011). Webb and al. (2008) proposed a model for UHP exhumation in Papua New Guinea that utilizes eduction to reconcile rapid exhumation with the local structures non-parallel to collision. In this section, we apply the model to the PRF and the TPC (Figure 2-15).

In our applied model, the PRF initially represents a thrust fault in a convergent tectonic zone. The Taconic orogeny has at least partially occurred, with the incoming island arc colliding to the west into Laurentia. Rocks and sediments are subducted down the east dipping subduction zone, and HP–UHP terranes are being formed at depth.

The reversal of tectonic forces, possible through methods such as microplate rotation as noted in Webb et al. (2008), shifts convergence into divergence. The PRF is reactivated as a normal fault, pulling rocks of the hanging wall to the east. Continued extension removes the overlying rocks, allowing deeply subducted rocks such as the TPC to be uncovered and rapidly exhumed. Buoyancy of subducted rocks may also aid in exhumation to the surface.

East-directed normal sense movement along the PRF is consistent with the E–W trending lineations and folds present in the GMA. Exhumation of UHP terrane at the Woodlark Basin in Papua New Guinea and the Dabie Hong'an area in China have been linked to stretching lineations that parallel the hinges of high-strain folds, and normal faulting associated with extensional regimes (Hacker et al., 2000, Little et al., 2007, Daczko et al., 2011). This narrative reconciles the presence of E–W folds in the GMA which run counter to north-south trending structures associated with the Taconic and Acadian orogenies.

2.8 Exhumation Models and Testability

Microstructures, age gradients, and transport direction identified in the footwall of the PRF have implications on the likeliness of modes of exhumation utilizing the PRF. This study examines patterns identified in these categories, which may aid in constraining possible exhumation models.

Patterns in strain gradients along the footwall can speak to the tectonic history of the terrane. Activation of the PRF utilizing eduction would likely result in a smooth strain gradient increasing from west to east, with rocks buried deeper along the fault experience more strain (Webb et al., 2008). In models for tectonic wedging and basal thrust exhumation, smaller thrust faults are active in the westward moving wedge (Thompson and Thompson, 2003; Lamon, 2001). Additional faults can alter the strain experienced over an area, so the strain gradient over the PRF under these conditions would not look as

smooth as under the eduction model. Increasing strain along the footwall can be identified by comparing microstructures between samples.

Age gradients observed under these different exhumation models would likely produce a similar pattern to strain gradients as described above. Smooth exhumation of rocks through eduction result in an age gradient from west to east, with younger ages towards the east (Webb et al., 2008). The presence of faults within the wedge in tectonic wedging and basal thrust models would likely alter age gradients, due to heat produced due to faulting that could alter or reset ages identified through $^{40}Ar/^{39}Ar$ dating.

Kinematics of deformation as correlated to fault motion along the PRF can also aid in constraining possible exhumation models. Both the eduction and tectonic wedging models argue for top-to-the-east motion of the PRF (Lamon, 2001; Webb et al., 2008). The basal thrust model suggests top-to-the-west motion along the fault, with possibility for local fault reactivation showing top-to-the-east senses of motion (Thompson and Thompson, 2003). Past studies conducted utilizing kinematic indicators have concentrated on select areas of the PRF, so more thorough kinematic studies of the PRF are necessary to accurately constrain fault movement.

2.9 Geochronology and $^{40}Ar/^{39}Ar$ Dating

This study utilizes the $^{40}Ar/^{39}Ar$ dating technique to obtain ages from collected field samples, as summarized by Mcdougall and Harrison (1999). The $^{40}Ar/^{39}Ar$ dating method is an evolution of the K/Ar dating method, both of which are based on the radioactive decay of ^{40}K. ^{40}K can break down into ^{40}Ca and ^{40}Ar, and has a half-life of

1250 My. Measuring concentrations of ^{40}K and radiogenic ^{40}Ar can delineate the amount of radioactive decay, and the amount of time passed since system closure. Minerals rich in K are targeted for techniques utilizing K and Ar, including muscovite, biotite, and amphibole.

Concentrations of ^{40}K and radiogenic ^{40}Ar can be used to measure the passage of time. When temperatures are sufficiently high within a rock, argon concentrations equilibrate with the ambient gas phase equal or close to that of the Earth's surface. Once a mineral system is closed, concentrations of ^{40}Ar in minerals increase over time, barring resetting by metamorphism or deformation. Concentrations of radiogenic ^{40}Ar can be calculated, with argon concentrations correlating with the passage of time. Previously formed systems can be "reset", when rocks are subjected to high temperatures long enough for the argon to equilibrate again. Systems can also undergo a partial resetting, which occurs when conditions do not allow for complete equilibration of the system, and result in argon concentrations (and thus calculated ages) that fall between equilibrium and concentrations in the system before reheating.

In $^{40}Ar/^{39}Ar$ dating, collected samples are irradiated to turn ^{39}K into ^{39}Ar. Concentrations of $^{40}Ar/^{39}Ar$ are measured, which are proportional to $^{40}Ar/^{40}K$ concentrations and thus work as a proxy. Samples can also be heated in increments to release gas to be analyzed, which provides more information about gas released from different parts of the grain, and about the precision of ages obtained. K/Ar dating utilizes fusion heating, which releases all the Ar from a sample at once.

$^{40}Ar/^{39}Ar$ dating utilizes step heating, which releases gas from a sample incrementally and allows for the dating of multiple aliquots of gas from an individual sample. This allows for the analysis of reheating events and diffusion of argon from sample grain boundaries, which may result in lower $^{40}Ar/^{39}Ar$ ages when gas from these spots are released. Plateau ages–concordant ages between multiple steps–can give a representative age of initial cooling, though may be changed by later tectonic events that would have altered the system (Figure 2-16).

2.10 Geochronologal studies in Vermont and the GMA

Laird et al. (1984, 1993) analyzed from rocks in the GMA using the $^{40}Ar/^{39}Ar$ technique, reporting $^{40}Ar/^{39}Ar$ total fusion ages and plateau ages of amphibole and muscovite ranging from 471 to 439 Ma. Ages between 386 to 355 Ma were also reported on muscovite, biotite, and amphiboles to the east and west of the GMA axis, suggesting that metamorphic overprinting occurred during the Devonian. These ages were interpreted to represent the Taconic and Acadian orogenies, respectively.

Laird et al.'s 1993 study further refined Ordovician metamorphic ages to 471–460 Ma based on total fusion and amphibolite ages, interpreting the Silurian total fusion age from the previous study (439 Ma) as due to inseparable biotite intergrowths because of high K/Ca. These ages were interpreted to represent Taconian metamorphism ranges, and included a total fusion age of 468 ± 6 Ma on glaucophane from HP rocks of the TPC. Both studies provided $^{40}Ar/^{39}Ar$ ages on amphiboles from the Belvidere Mountain Complex (Figure 2-2), reporting a range between 504–490 Ma. Ages determined in Laird

et al. (1984, 1993) have been later interpreted to represent the first pulse of Taconic metamorphism (470–460 Ma, in Lamon, 2001; Thompson and Thompson, 2003) and Acadian metamorphic overprinting (386–355 Ma, in Laird et al., 1984, 1993).

Castonguay et al. (2011) also conducted $^{40}Ar/^{39}Ar$ analyses of rocks in and near the GMA, examining rocks from the PRF hanging wall and footwall (including the Belvidere Mountain Complex), and the westward neighboring Underhill slice. Analysis of these $^{40}Ar/^{39}Ar$ ages from the GMA helped to further refine the timing of deformational events, denoted in their paper as early (D_e), middle (D_m), and late (D_l). D_e, with ages obtained from mafic schist amphiboles, ranges from 471–460 Ma, and is linked to Taconic deformation. This postdates the deformation of the Belvidere Complex, at 505–473 Ma. D_m is associated with Silurian and early Devonian fabrics and southeast directed structures. Ages from D_m are from between 446–415Ma, and foliations defining D_m are associated with synkinematic mica crystallization and recrystallization of inherited muscovite. D_l deformation dates range from 386 to 355 Ma, providing a maximum age for Acadian deformation in northern Vermont. Dates obtained in this study are correlative with dates from Quebec, but give evidence for diachronism along strike.

2.11 Relevant Geochronology in Canada

Geological structures in Vermont are key to a full tectonic understanding of the northern Appalachians because they link correlative ophiolite and accretionary prism sequences found in southern Quebec and New England (Kim et al, 2003). For example, the St-Joseph/Bai Verte-Brompton Line correlates to the Burgess Branch Fault Zone

(Figure 2-17), juxtaposing different metamorphic domains with contrasting isotopic ages (Tremblay and Pinet, 2016). As such, dates chronicling metamorphism and tectonic activity in southern Quebec are vital for a complete tectonic understanding for the region. Apparent along-strike diachronism is attributed in part to different structural levels between features found in southern Quebec and western New England (i.e. younger cooling ages from deeper structural levels compared to older ages from higher structural levels), adding further complexity.

2.11.1 Canadian Geochronology and the Taconic Orogeny

Taconic metamorphism in the northern Appalachians is interpreted to include ophiolitic metamorphic soles, which are in fault contact with lower grade metamorphic rocks of the Humber Zone. $^{40}Ar/^{39}$ ages from amphibole and muscovite from amphibolite soles and ophiolites fall between 456-470 Ma in southern Quebec (Tremblay et al., 2011; de Souza et al., 2012) and between 456-470 in the Gaspe Peninsula (Pincivy et al., 2003; Malo et al., 2008, de Souza et al., 2012), chronicling metamorphism during Taconic Orogeny. Older ages have been obtained, including 491 ± 11 Ma by Whitehead et al. (1996) from an amphibolite from the ultramafic Pennington Sheet, and a U-Pb crystallization age of 480 Ma for the Thetford Mines and Asbestos Ophiolitic Complexes (Dunning et al., 1986; Whitehead et al., 2000; Tremblay et al., 2011).

2.11.2 Canadian Geochronology and the Salinic Orogeny

Data from Castonguay et al. (1997, 2001, 2007) have produced dates from $^{40}Ar/^{39}$ dating linked to phase 1 of the Salinic Orogeny. Plateau and apparent low temperature

step ages of retrograded amphiboles from southern Quebec generated ages from 429–424 Ma, and biotite plateau ages ranged between 420–411 Ma. Plateau ages from muscovite grains ranged from 433–405 Ma, which have been interpreted to reflect the presence of mixed mineral phases during progressive deformation and metamorphism (Castonguay et al., 2001, 2007). An irregular younging of weighted apparent age maxima is documented from northwest to southeast over the Sutton-Notre Dame Mountains anticlinorium, which is considered a continuation of the Green Mountain anticlinorium (Castonguay et al., 2001 2007). $^{40}Ar/^{39}Ar$ ages within the Salinic Orogeny are generally absent in samples from the internal Humber Zone of the Gaspe Peninsula, but one date from a mica schist sample from the Shickshock-Sud fault (correlative to the St. Josephs Fault) yielded a low temperature step age of 417.8 ± 3.7 Ma (2σ).

$^{40}Ar/^{39}$ data also records the timing of phase 2 of the Salinic Orogeny. Dates from the hanging wall of the St. Joseph fault range from 420–410 Ma, and match brittle faulting in the Gaspe Peninsula, recording progressive deform that occurred in response to extension. (Castonguay et al., 2007). Constraints for phase 2 faulting events are also recorded through 2D seismic lines and sedimentary growth strata, which indicate a period of syn-depositional normal or transtensional faulting during the late Silurian to Early Devonian (Pinet, 2013).

2.11.3 Canadian Geochronology and the Acadian Orogeny

Dates chronicling the Acadian Orogeny in the Northern Appalachians, including Canada, Maine, and New England show evidence for northwest migration of the deformation front towards Quebec over a 40 My period (Bradley et al., 2000). In Quebec

and the Gaspe Peninsula, the age of Acadian Deformation has been constrained using several methods, including dating of late to post-tectonic magmatic rocks, and dating the age of metamorphism (Tremblay and Pinet, 2016).

Granitic plutons from along the La Guadeloupe fault and the Gaspe Belt in southern Quebec were dated between 384–374 Ma (Simonetti and Doig, 1990). The Gaspe Peninsula itself has granitic intrusions found in the north side of the peninsula dated at 391 ± 3.4 Ma (Whalen et al., 1991). Plutons here are not affected by Acadian deformation.

Regional metamorphism in southern Quebec and western New England recording the Acadian Orogeny range from 395–375 Ma (Armstrong et al., 1992; Tremblay et al., 2000). Acadian overprints are observed in several $^{40}Ar/^{39}$ age spectra from the Sutton-Notre Dame Mountains anticlinorium (Castonguay et al., 2001, 2007). Acadian overprinting is not observable in some regions of southern Quebec, due to higher structural levels and low-grade Acadian deformation (Hesse and Dalton, 1991; Bertrand and Malo, 2001).

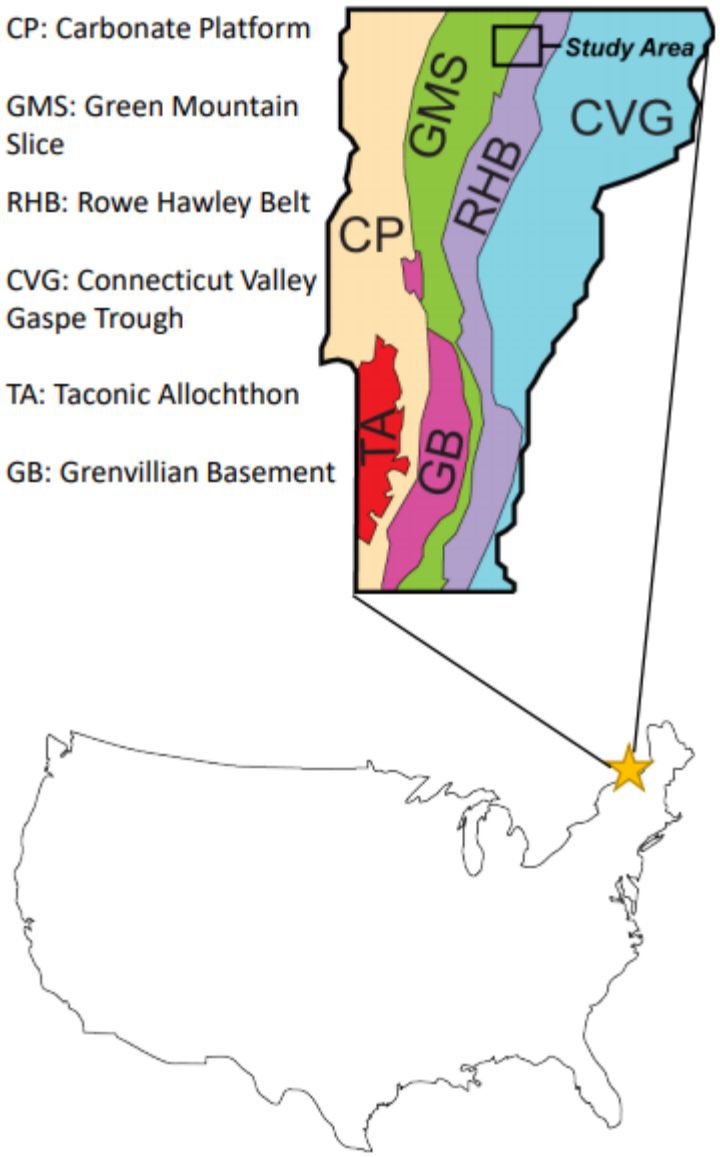

Figure 2-1: An inlaid map of the study area in Vermont, within the context of the United States. Vermont geology can be simplified into six lithotectonic slices, representing different periods in its geologic history (Stanley and Ratcliffe, 1985). The map of Vermont is modified from Kim et al. (2003).

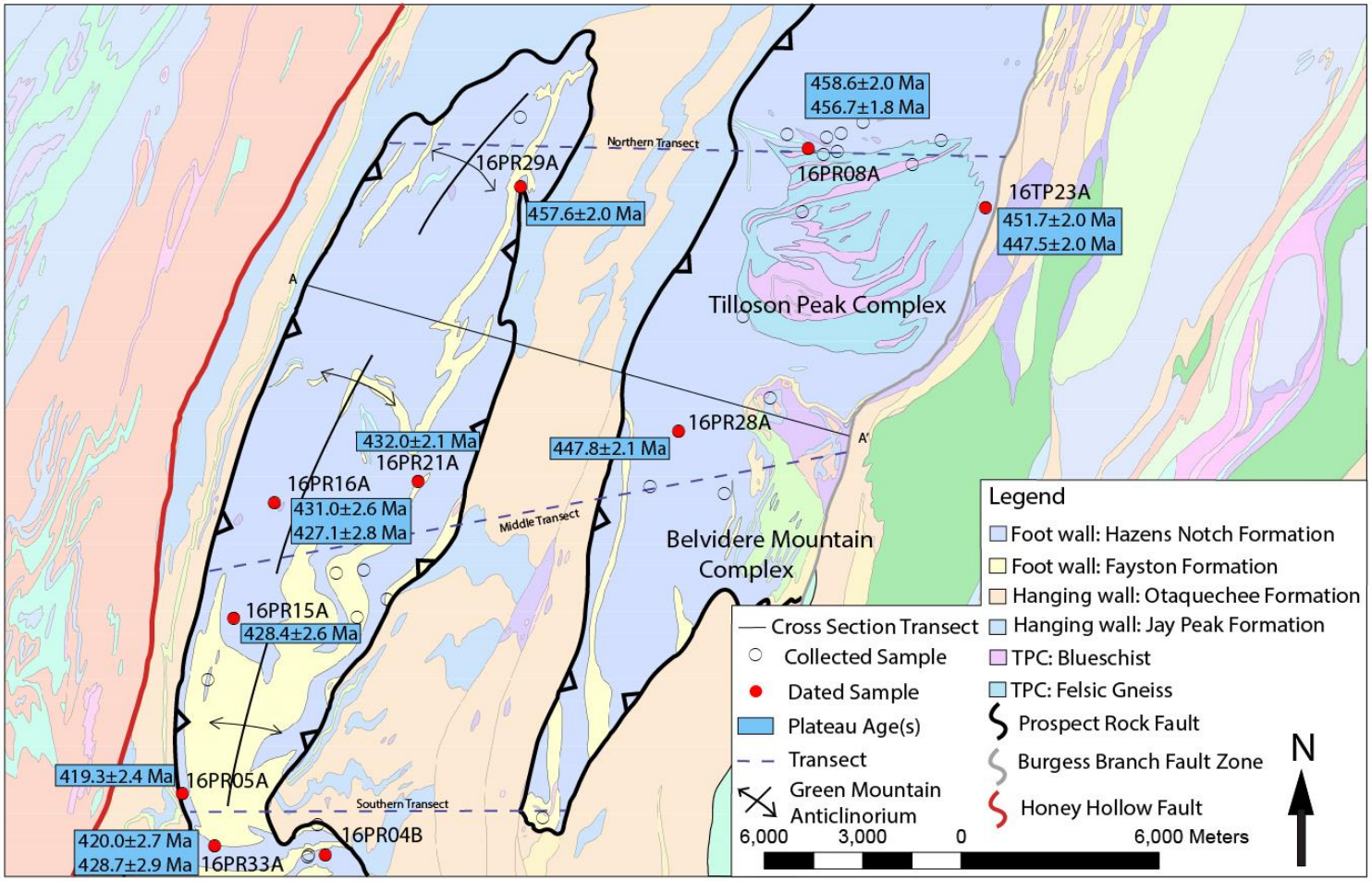

Figure 2-2: Geologic map of the Prospect Rock Fault and surrounding areas. Modified from Ratcliffe et al., 2011.

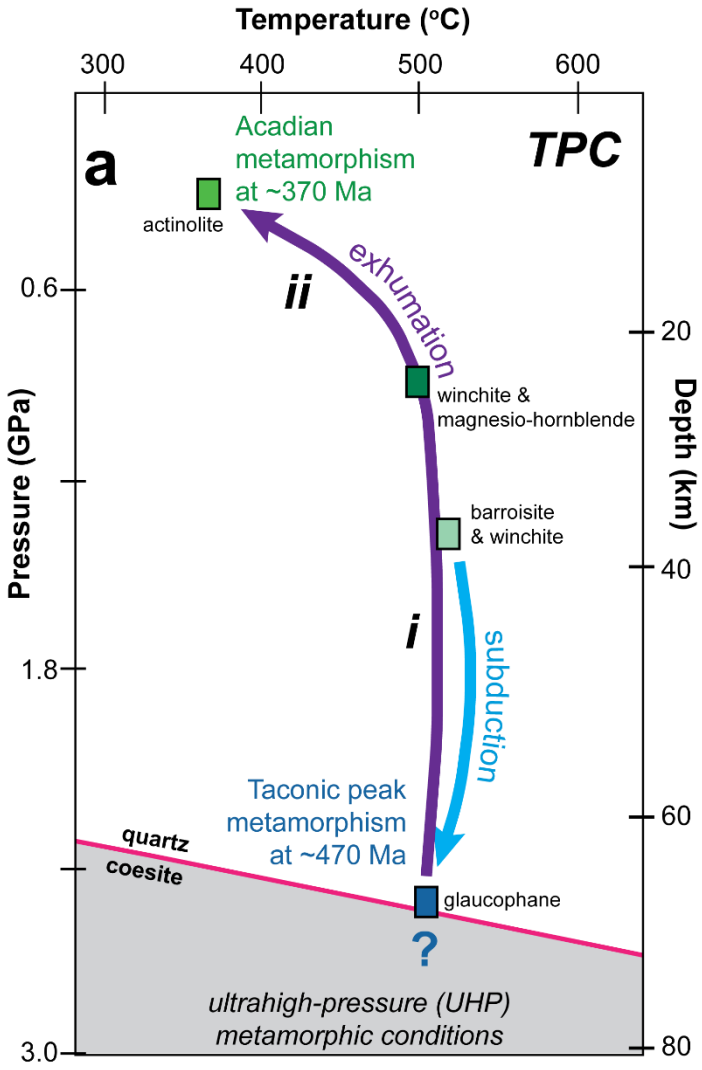

Figure 2-3: Specific temperature, depth, and pressure thresholds must be met for UHP metamorphism to occur to form UHP minerals such as glaucophane. Figure modified from Honsberger (2015), showing the P-T-t pathway for an amphibole group mineral, and its forms as conditions change.

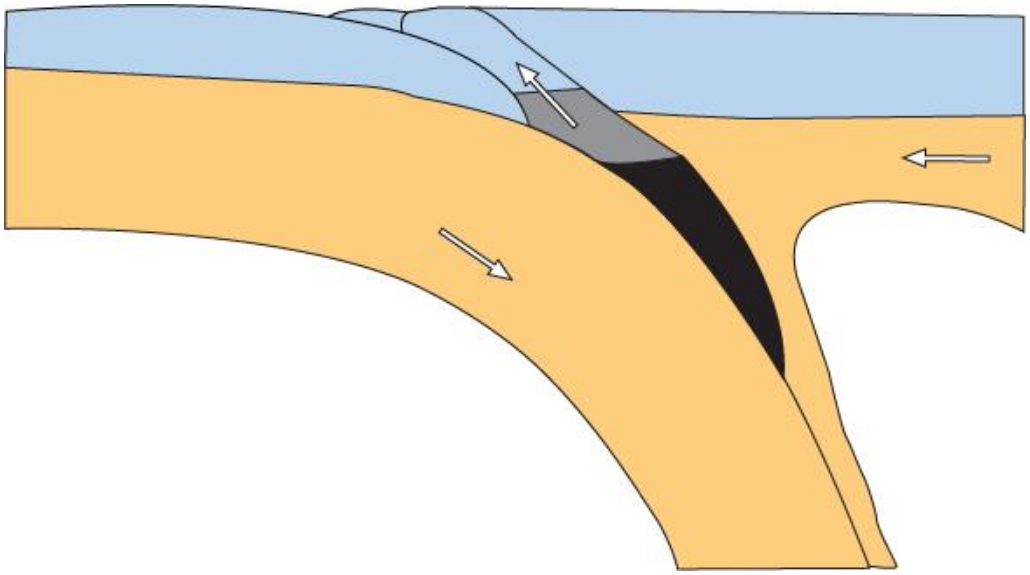

Figure 2-4: A diagram depicting the Chemenda Model, modified from Hacker et al. (2013). As a trapped continental slab (black, gray) is subducted with the surrounding mantle lithosphere (orange) and crust (blue), it can undergo UHP metamorphism. Buoyancy in the slab can cause detachment (gray), and the slab is thrust to the surface along the shear zone.

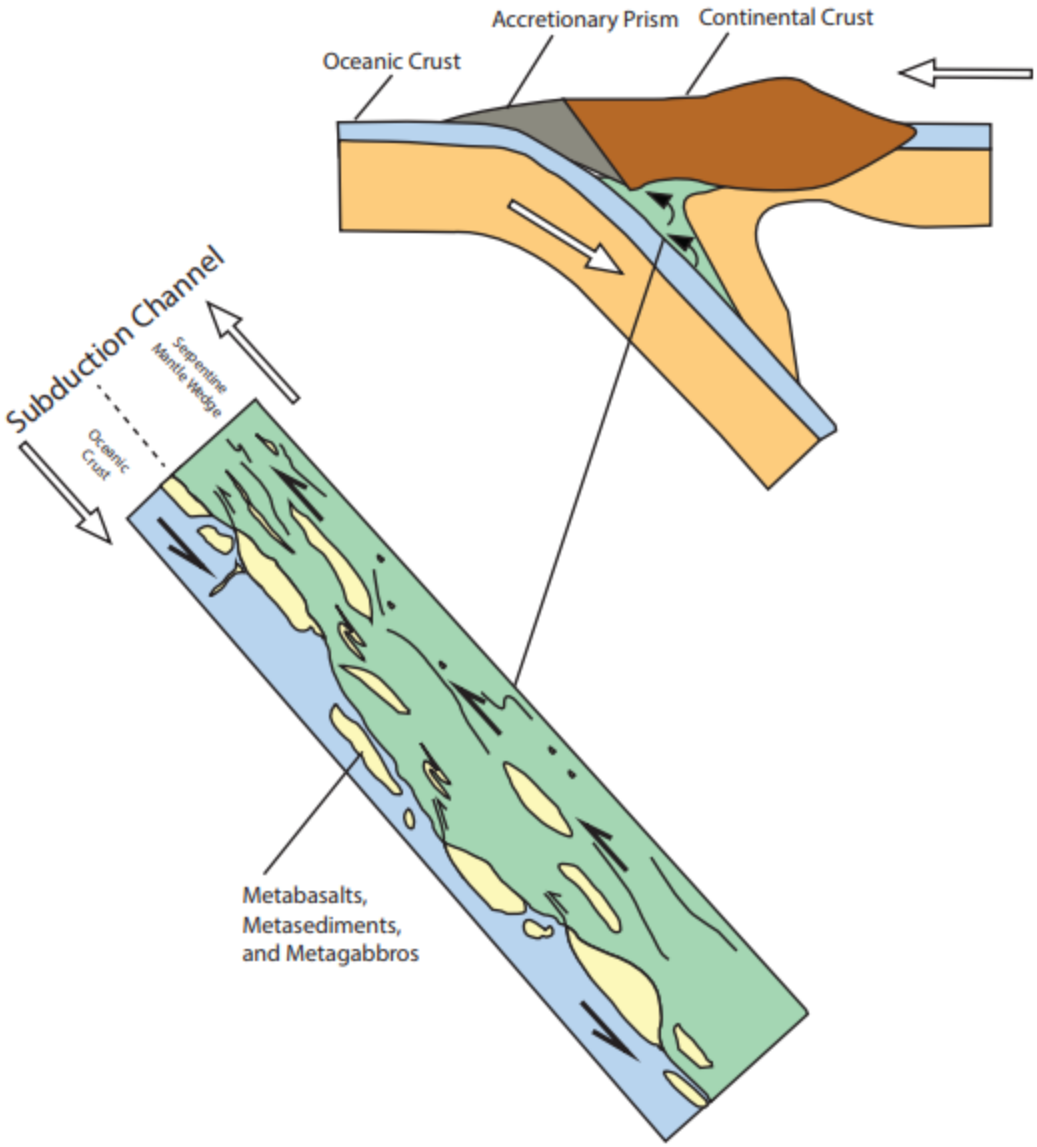

Figure 2-5: Exhumation via a serpentinite channel, modified from Guillot et al. (2009). Metabasalts, metasediments, and metaggabros derived from the oceanic lithosphere are incorporated into a mélange of serpentinites. The low viscosity and density of serpentinite, combined with the triangle shape of the serpentinite channel entrains the material upward towards the surface (Guillot et al., 2009, and references therein).9, and references therein).

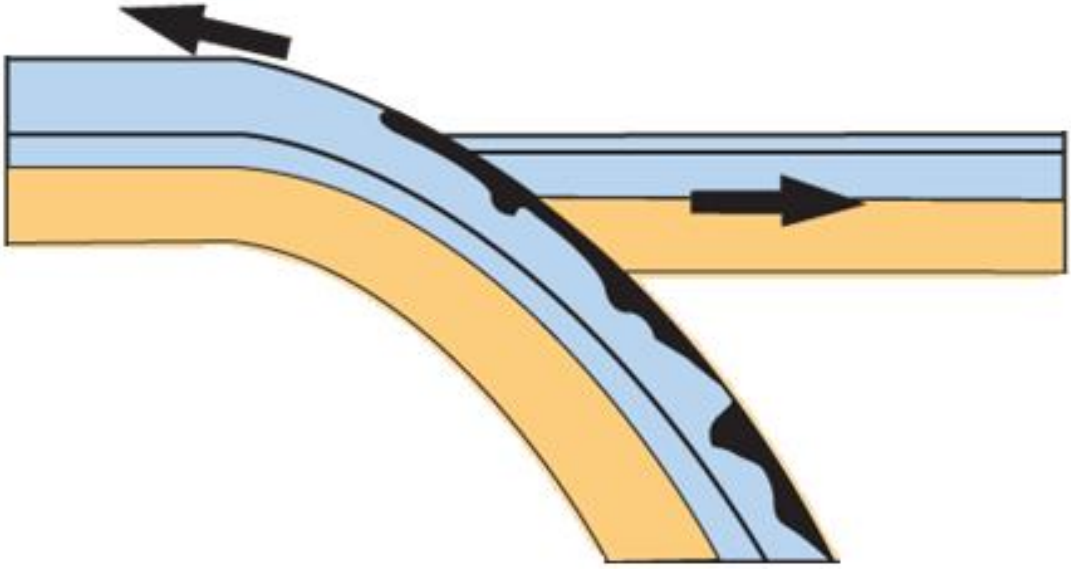

Figure 2-6: Exhumation via eduction, modified from Hacker et al. (2013). Subduction zones can be reversed and activated as normal sense fault zones. UHP rocks (black) buried deeper in the subduction zone are exhumed and exposed at the surface.

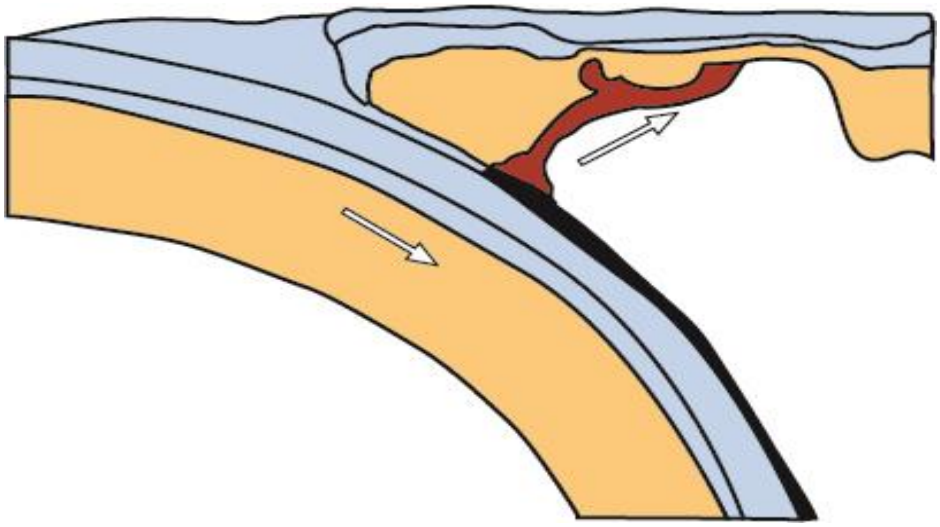

Figure 2-7: Exhumation via diapir rise, modified from Hacker et al. (2013). Rocks subducted to UHP metamorphic depths (black) can aggregate as diapirs and rise through the surface (red), without being assimilated into the mantle wedge.

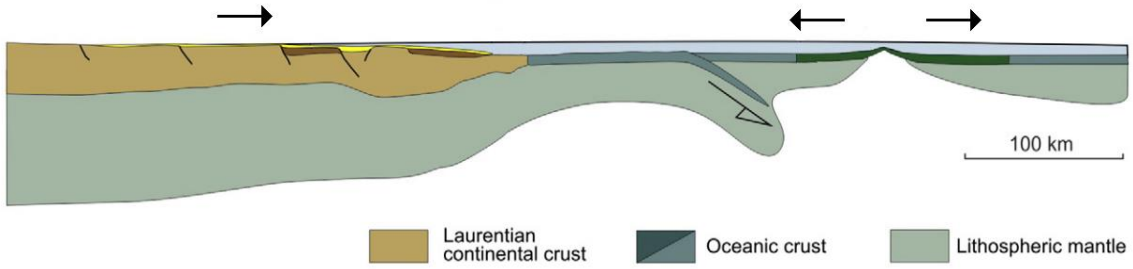

Figure 2-8: Rifting off the coast of Laurentia, modified from Tremblay and Piney (2016). Rifting of the supercontinent Rodinia created the proto North American continent of Laurentia and the Iapetus ocean. Subduction off the coast of Laurentia created an east dipping subduction zone (present day coordinates). Modified from Tremblay and Pinet, 2016.

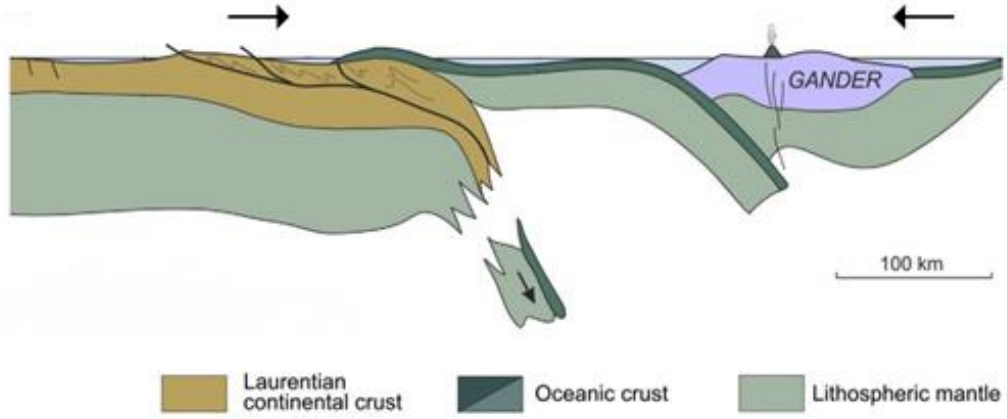

Figure 2-9: Collision of Laurentia and an island arc, as part of the Taconic Orogeny. Subduction continues to the east off the coast of Laurentia while the Gander margin approaches. Modified from Tremblay and Pinet, 2016.

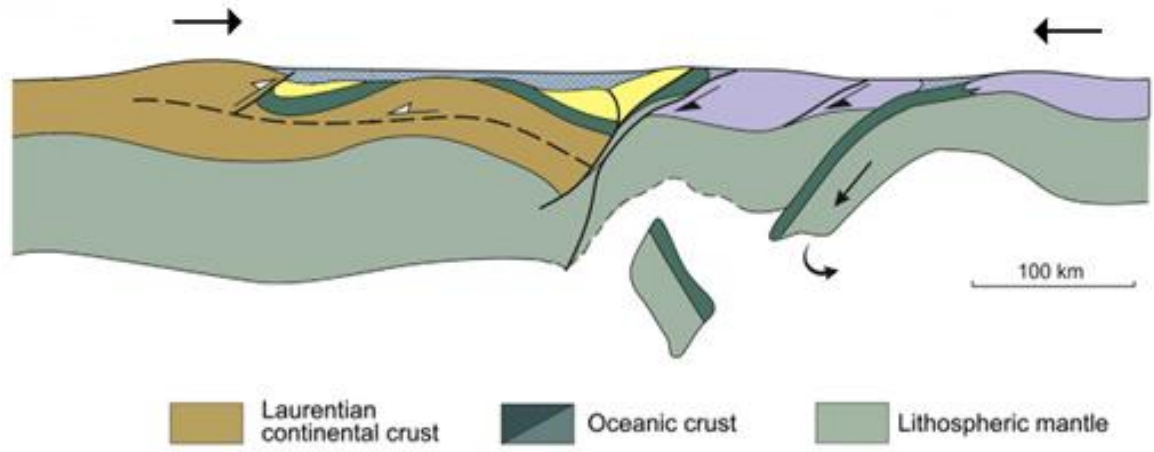

Figure 2-10: The collision between Laurentia and the Gander margin causes the Salinic Orogeny. Subduction has changed orientation from east dipping to west dipping. Modified from Tremblay and Pinet, 2016.

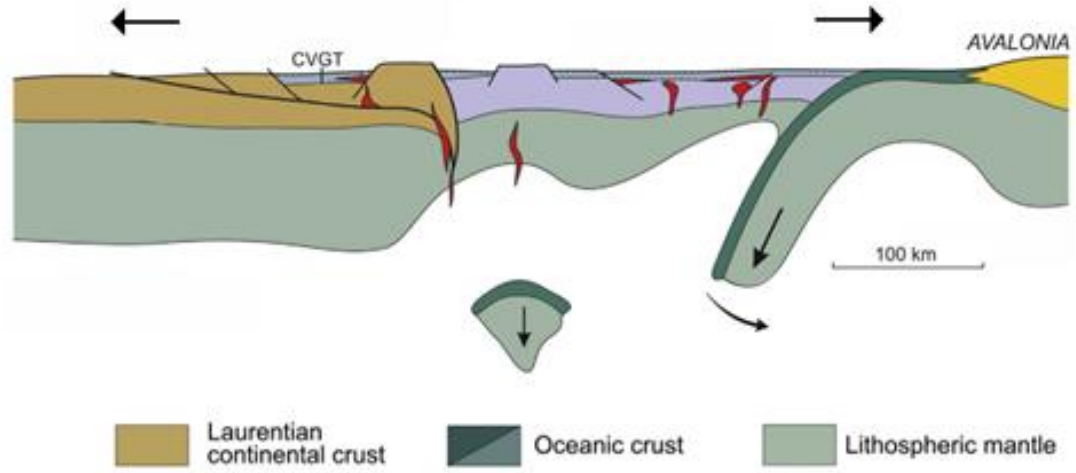

Figure 2-11: Rising asthenosphere under the Laurentian continent causes extension and creates the Connecticut Valley-Gaspe Trough. The Iapetus Ocean is consumed as Avalonia approaches, and its collision with Laurentia results in the Acadian orogeny. Modified from Tremblay and Pinet, 2016.

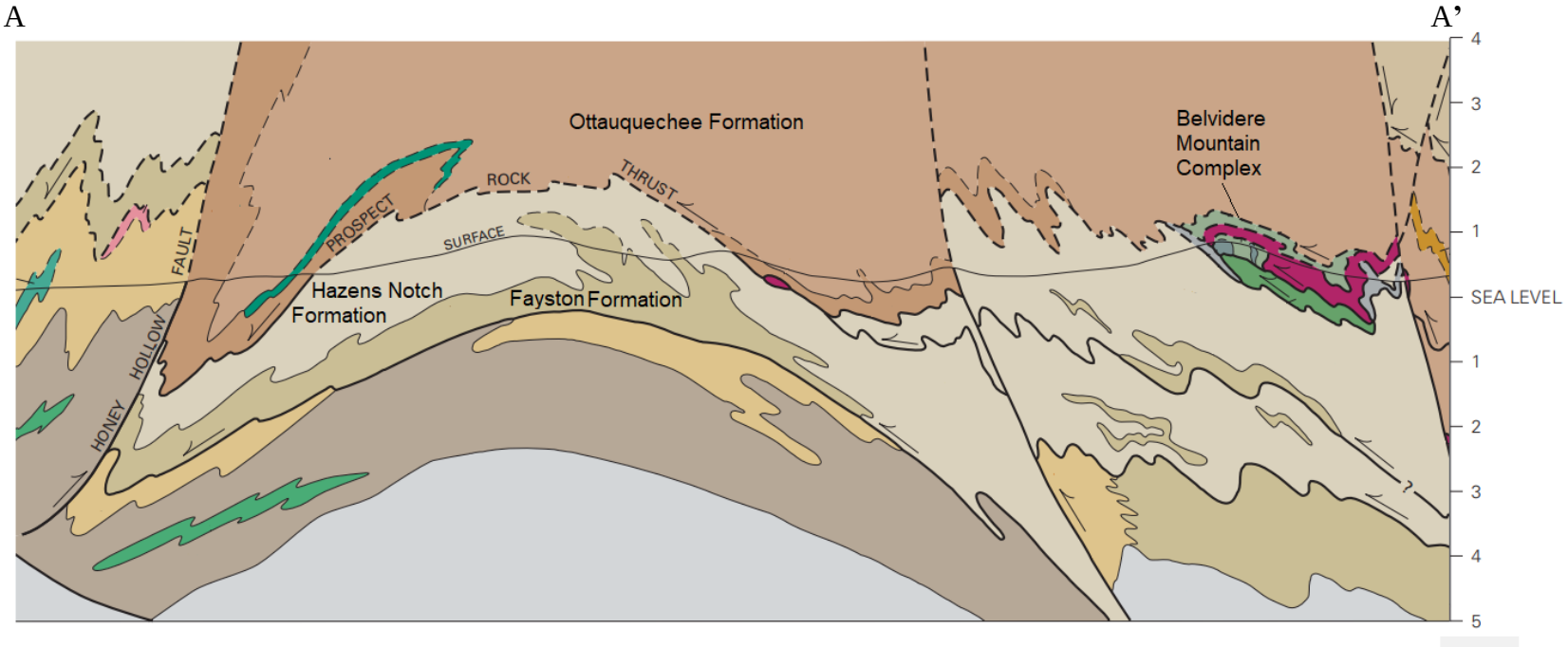

Figure 2-12: Cross section of structures along the PRF, modified from Ratcliffe et al. (2011). The cross section transect can be found in Figure 2-1. Structures in the PRF are folded, and are cut by the Burgess Branch Fault Zone, and the Honey Hollow Fault. The Hazens Notch Formation (beige), Fayston Formation (gray-brown), Ottaquechee Formation (light brown) and Jay Peak Formation (darker brown) define the footwall and hanging wall of the PRF.

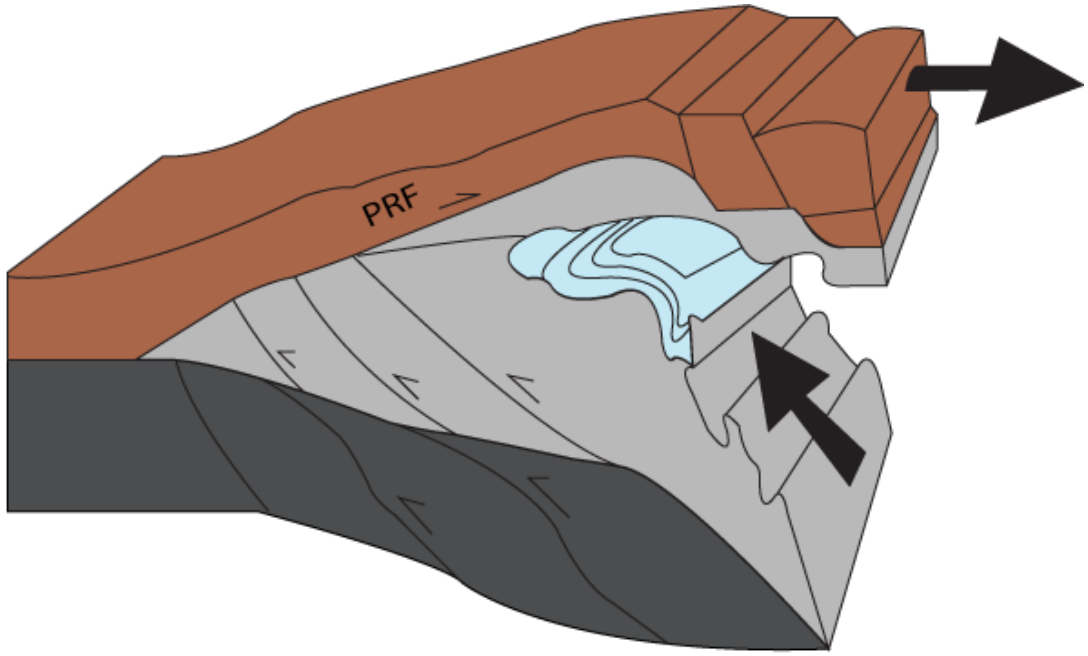

Figure 2-13: The Tectonic Wedging model, as proposed by Lamon (2001). The PRF represents the roof thrust formed as a part of tectonic wedging. Footwall rocks experience higher grade metamorphism, and are thrust westwards under fined grain rocks. Rocks experience a top-to-the-east shear sense. The TPC is added to the wedge by underplating, and exposed to the surface by normal faulting.

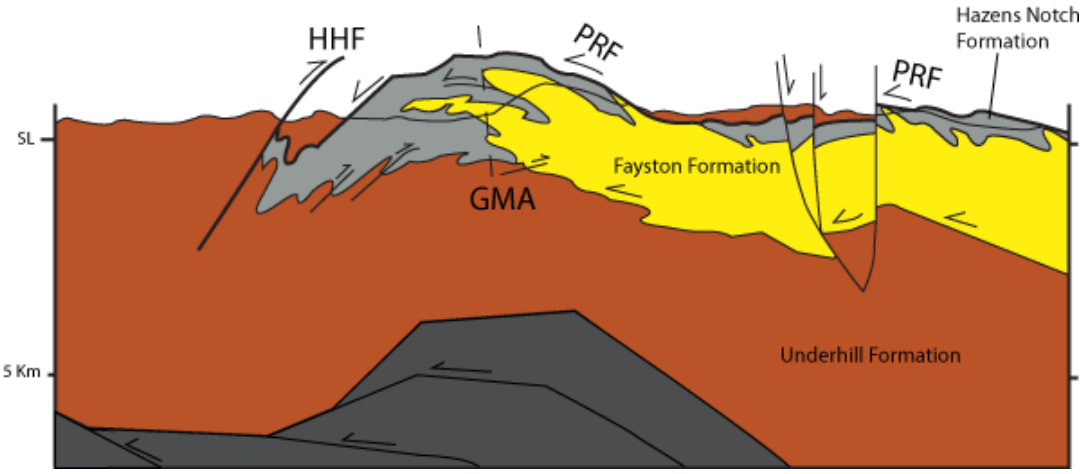

Figure 2-14: The Basal Thrust Model, adapted from Thompson and Thompson (2003). The PRF represents the basal thrust of an emplaced accretionary prism riding westward onto the Laurentian continent. The exhumation of the TPC is explained through serpentinite channel exhumation, which could rapidly move the terrane towards the surface.

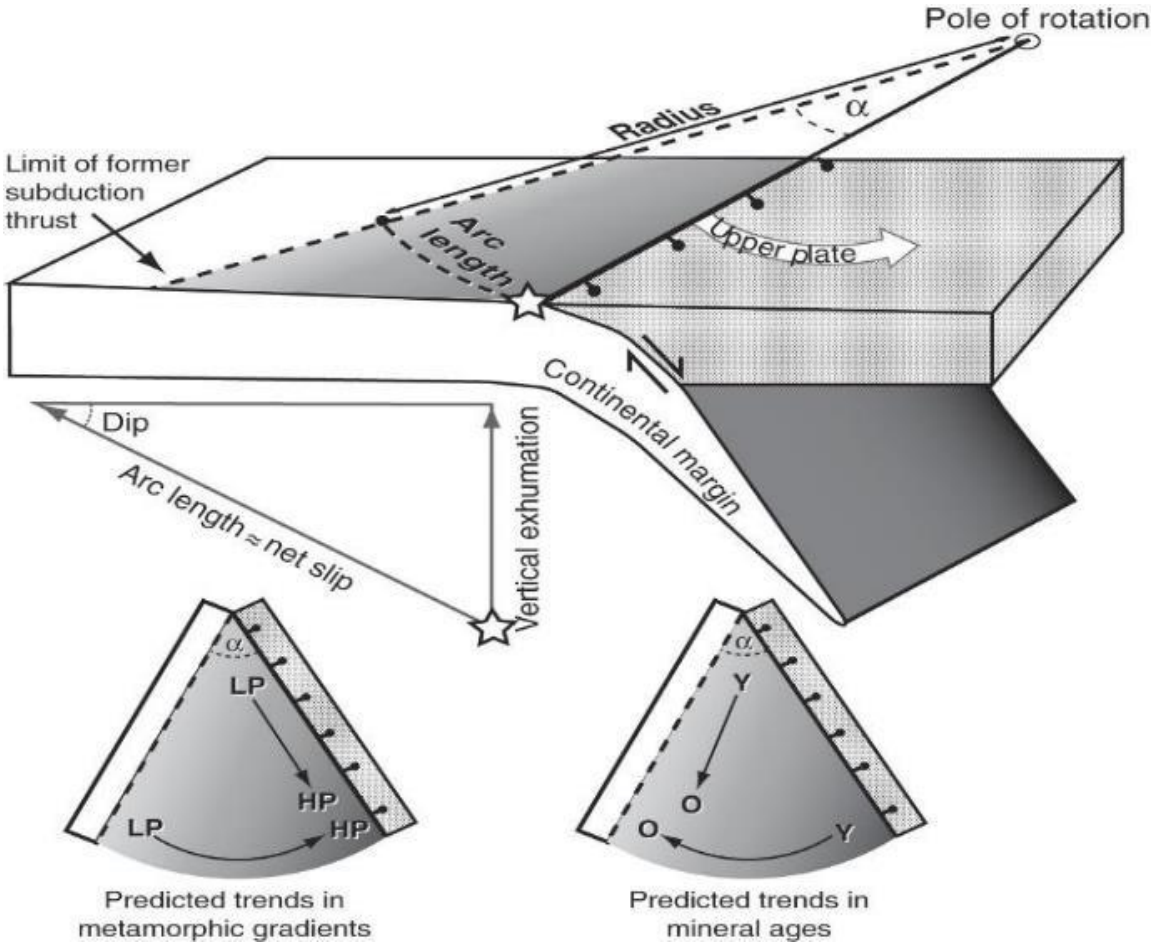

Figure 2-15: An example of eduction via microplate rotation, from Webb et al. (2008). Under this model, the PRF is reactivated as a normal fault. Deeply subducted UHP rocks are exhumed as overburden is removed through normal sense movement. In the original model from Papua New Guinea, extension occurs with an aspect of rotation (α).

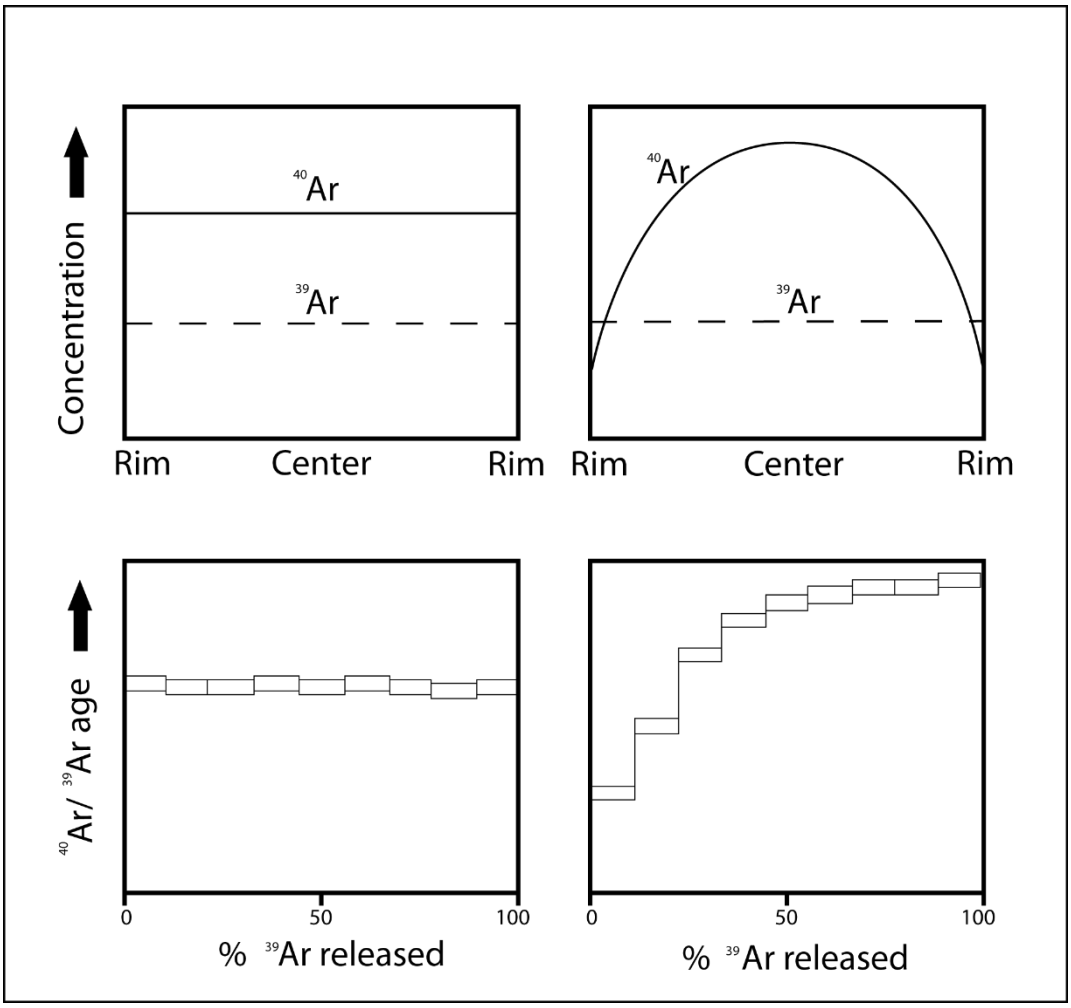

Figure 2-16: Figure modified from McDougall and Harrison, (1999). Theoretical results of $^{40}Ar/^{39}Ar$ dating for two different samples. Step heating is used to incrementally release Ar from a mineral. During step heating, samples are heated by laser at increasingly higher values, which can allow the release of Ar from more retentive spots, such as the center of the mineral grain. The ratio between $^{40}Ar/^{39}Ar$ isotopes is used to an age. Each box represents a higher temperature step, which is able to release Ar from more retentive spots. Rocks with simple cooling histories may show just one consistent age, whereas rocks with complex metamorphic or deformation histories may show age gradients.

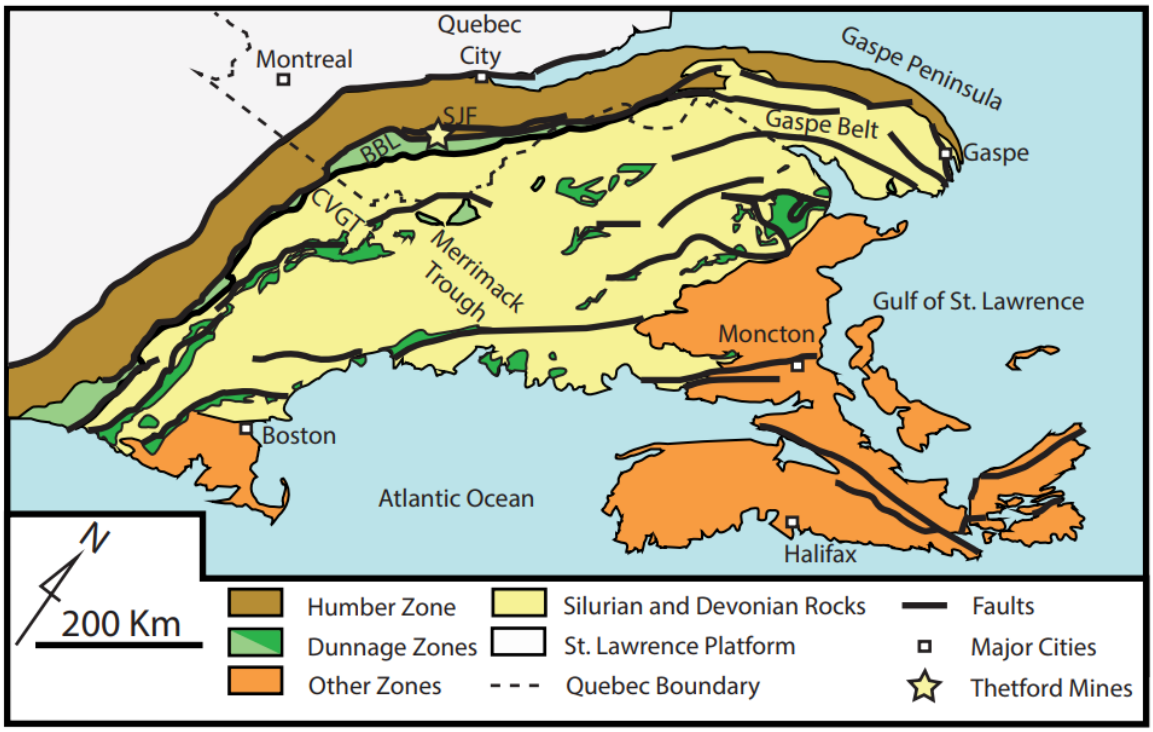

Figure 2-17: Simplified geologic map of New England and the Gaspe Peninsula, adapted from Tremblay and Pinet (2016). The Baie verte-Brompton Line (BBL) and the St-Josephs Fault (SJL) are interpreted as a continuation of the Burgess Branch Fault Zone. The Connecticut Valley Gaspe Trough (CVGT) and the Merrimack Trough are continuous from New England into Canada.

Chapter 3: Methods

Modes of exhumation utilizing the PRF to exhume the TPC have varying implications for the resulting microstructures, strain, transport direction, and P-T-t-D histories along and around the fault. To understand the tectonic significance of the PRF, microstructural analysis, geochronology and P-T-t-D analysis were employed constrain its history. This study examines new geochronological dates from the PRF footwall, and interprets the results within the context of microstructural data, and existing mapping and structural frameworks.

3.1 Field Component

The field component of this study was conducted during the summer of 2016. The area was surveyed through five transects that spanned over the footwall of the Prospect Rock Fault. Transects were oriented E–W and N–S along the footwall of the PRF, between the Vermont towns of Johnson, Cambridge, Montgomery, and Westfield. Three major transects were utilized, and are denoted as the northern, middle, and southern transects (See Figure 2-1 in Chapter 2).

The area was surveyed with three goals: documentation of field structures across the PRF footwall, identifying lithologies and minerals within the study area, and collection of oriented samples for use in microstructural, kinematic, and $^{40}Ar/^{39}Ar$ analyses. Structural data was utilized from previous studies, including Kim et al., (1999), Thompson et al., (1999), and Bothner and Laird (1999). Forty oriented samples were collected during the field study, in addition to structural and lithological observations

recorded for over 100 sites in the PRF footwall. Structural data was used to orient hand samples and thin sections.

3.2 Microstructural Analysis

Orthogonal thin section billets were cut to capture the X-Z and Y-Z sections of the finite strain ellipse. The X-Z section is parallel to the stretching L_2 lineation and perpendicular to the dominant S_2 foliation, and the Y-Z section perpendicular to both the lineation and foliation. In the absence of L_2 lineation, the 'X-Z' section was cut parallel to the dip direction (Figure 3-1). Thin sections were examined with a petrographic microscope. Analysis of thin sections allowed for selection of target minerals for $^{40}Ar/^{39}Ar$ dating. Thin sections were described according to microstructural elements as detailed in Passchier and Trouw (2005). Samples were analyzed to examine potential kinematic indicators, relationships between foliation generations, and mineral growth in respect to P-T-t-D changes. Minerals defining foliation, and the relationship between foliations were utilized to interpret $^{40}Ar/^{39}Ar$ ages in the context of tectonic events. Quartz microstructures were used to qualitatively infer temperatures of deformation, investigating if samples experienced elevated temperatures following deformation or cooled rapidly. Details on microstructures can be found in the results and discussion chapters.

3.3 $^{40}Ar/^{39}Ar$ Dating

Samples for $^{40}Ar/^{39}Ar$ dating were selected after analyzing thin sections for presence of K-bearing minerals and associated foliations, bearing in mind sample

location. White mica and tourmaline were identified in thin section as potential targets, though only white mica samples were utilized in $^{40}Ar/^{39}Ar$ dating. Samples were crushed to 125-500 µm fraction, washed, sonified, and dried to remove lose dust and particulates. Inclusion free target minerals were handpicked from crushed samples under a bioptic microscope. Picked minerals were loaded into packets of aluminum foil, which were inserted into suprasil vials. Vials were placed within an aluminum canister for irradiation. Samples were irradiated alongside aliquots of Fish Canyon Tuff Sanidine for use as an apparent flux monitor (age = 28.03 Ma; Renne et al., 1998). Samples were sent to Oregon State University (Corvallis, Oregon, USA), and were irradiated for 14 hours at the Cadminum-Lined In-Core Irradiation Tube (CLICIT) reactor.

$^{40}Ar/^{39}Ar$ dating analysis was conducted at University of Vermont Noble Gas Geochronology Laboratory. Laser step hearting utilized a Santa Cruz Laser Microfurnace 75 W diode laser system. Muscovite samples were loaded into a copper planchet with 1.5mm wells. A Nu Instruments Noblesse magnetic sector noble gas mass spectrometer was used to analyze argon isotopes released during step-heating. Step-heating analyses were performed predominantly on single grain samples, but also included multigrain aliquots. Data corrections were performed to account for mass discrimination, atmospheric argon, neutron-induced interfering isotopes, and decay of ^{37}Ar and ^{39}Ar.

Mass discrimination was calculated by analyzing known aliquots of atmospheric argon, with a mass discrimination of 296.8, an error percentage of 0.35, and an assumed atmospheric value of 298.56 (Lee et al., 2006). Correction factors were calculated to account for interfering nuclear reactions for irradiated samples by analyzing argon

extracted from irradiated samples of CaF^2 and K glass. These correction factors are as follows: $(^{40}Ar/^{39}Ar)_K = 5.40 \times 10^{-4} \pm 1.35 \times 10^{-4}$, $(^{36}Ar/^{37}Ar)_{Ca} = 2.65 \times 10^{-4} \pm 2.20 \times 10^{-5}$, $(^{39}Ar/^{37}Ar)_{Ca} = 6.95$ x 10-04 $\pm 8.97 \times 10^{-6}$ (Jicha and Brown, 2014; Renne et al., 2013)

J factors were calculated for samples through a linear interpolation of sample positions between flux monitor packets within the irradiation tube. Isotope decay constants from Steiger and Jäger (1977) and Stoenner et al. (1965) were utilized to calculate ages. An in-house data reduction program and Isoplot 3.0 were used in age calculations for both inverse isochron and apparent age data (Ludwig, 2003).

Plateau ages for sample spectra are reported at the 1σ level if the criteria is met to calculate one (at least three concordant contiguous steps comprising a minimum of 50% of the ^{39}Ar released; see McDougall and Harrison, 1999). In the absence of plateau ages, weighted mean averages are reported at the 2σ level. Complete data tables, including J-factors and errors, can be found in the Appendix.

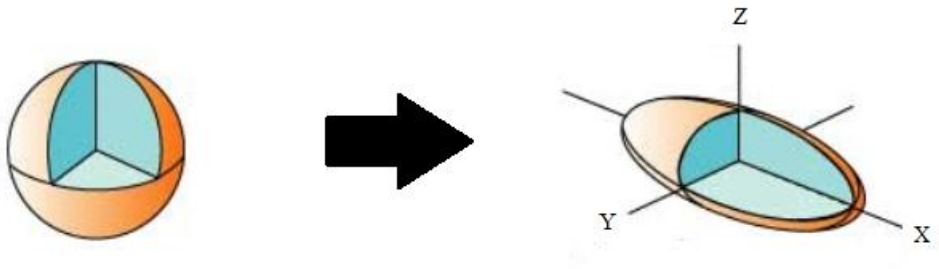

Figure 3-1: Figure modified from Van der Pluijm and Marshak (2004). Strain ellipsoids are used to depict deformation of a three-dimensional object. Deformation of the sphere into the ellipsoid can be described utilizing three axis: X, Y, and Z. The X axis represents the long axis of deformation, Y the middle axis, and Z the shortest axis. Thin sections in this study were cut along the X-Z and Y-Z sections, with L_2 stretching lineations defining the X axis, and S_2 foliation defining the X-Y plane. Dip direction of S_2 foliation was utilized for defining the X axis when the sample did not exhibit L_2 stretching lineations.

Chapter 4: Results

4.1 Introduction

This chapter describes the results from both microstructural and $^{40}Ar/^{39}Ar$ analysis for samples of interest. Results will be described by transect order, examining the northern, middle, and southern transects from west to east. Sample locations can be found in figure 2-1 in Chapter 2. Patterns from sample analysis results, and their implications for the PRF will be discussed in Chapter 5. Microstructure descriptions will cover several topics, including mineral assemblage, features that define foliations, kinematic indicators, and quartz and albite microstructures. The dominant foliation for the thin section is denoted as S_n, with foliations pre-dating S_n denoted as S_{n-1}, and foliations post-dating Sn denoted as S_{n+1}.

$^{40}Ar/^{39}Ar$ spectra analyses will examine calculated plateau ages, weighted mean averages, and the age ranges of individual steps when of interest. Major microstructures per sample, and also $^{40}Ar/^{39}Ar$ plateau ages are summarized in Tables 4-1 through 4-5.

4.2 Northern Transect

4.2.1 16PR29A

Microstructures

Sample 16PR29A is a schist from the Hazens Notch Formation, obtained on the western side of the Prospect Rock Fault foot wall. Thin sections exhibit spaced foliation (S_n), largely defined by quartz microlithons and mica cleavage domains. Mica domains

contain white mica and chlorite, with small amounts of biotite. Titanite, albite, and calcite grains are found sporadically as accessory minerals.

Outcrop foliation was measured as 358º/40º (Az), and lineation as 080º/40º. Mica and quartz that define the dominant S_n foliation are found truncated by C' shear bands, indicating a top-to-the-northwest sense of movement (Figure 4-1). In this sample both the dominant foliation and lineation dip towards the east, thus top-to-the-northwest shear aligns with apparent reverse motion. Quartz grain sizes can vary, with some microlithons containing larger grains than others. Quartz grains shapes are amoeboid, suggesting grain boundary migration as the predominant deformation mechanism. Grains preserve evidence of subgrain rotation and limited bulging. Locally, some mica grains are highly oblique to the S_n foliation, and appear to be truncated by cleavage domains. This could be evidence of an older foliation (S_{n-1}).

$^{40}Ar/^{39}Ar$ Step-Heating Results

Two aliquots of single white mica were analyzed from sample 16PR29A (Figure 4-2). Aliquot #1 yielded a reasonably flat spectrum with a plateau age of 457.6 ± 2.0 Ma (1σ). Steps not included in the plateau age (blue steps) ranged from c. 442–490 Ma. In comparison, the spectrum obtained from Aliquot #2 displays an age spectrum of c. 479–431 Ma, with ages decreasing of the course of the experiment. While aliquot #2 did not yield a plateau age, a weighted mean age of 449.7 ± 4.3 Ma (1σ) is obtained from the plateau-like segment and is concordant with the plateau age of aliquot #1 at the 2σ level.

4.2.2 16PR08A

Microstructures

Sample 16PR08A is from the Hazens Notch Formation, located just north of the Tillotson Peak Complex. In thin section, the sample is composed of quartz and mica. Mica domains are predominantly white mica, but also contain chlorite and small amounts of biotite. Medium sized garnet porphyrobasts are relatively abundant, in addition to titanite and tourmaline accessory minerals.

An anastomosing spaced foliation (S_n)is defined by mica cleavage domains and quartz microlithons (Figure 4-3a). Individual mica grains diagonal to S_n appear locally in thin section, and may represent S_{n-1} when truncated by mica grains oriented along S_n, and potentially S_{n-2} when orthogonally oriented micas. However, diagonal mica grains and anastomosing micas are hard to differentiate. Garnets are idiomorphic, and exhibit fractures perpendicular to foliation (Figure 4-3b).

Quartz grains are amoeboid and display subgrains within individual quartz grains, suggesting grain boundary migration and subgrain rotation were active in this sample. Some grains preserve limited evidence of grain boundary area reduction, bulging, and undulose extinction.

$^{40}Ar/^{39}Ar$ Step-Heating Results

Two aliquots of single grains of white mica were analyzed from sample 16PR08A (Figure 4-4). Both aliquot #1 and #2 yielded plateau ages of 458.6 ± 2.0 Ma (1σ) and 456.7 ± 1.8 Ma (1σ), respectively. These ages are concordant and both are composed of steps comprising 100% of the Ar released.

4.2.3 16TP23A

Microstructures

Sample 16TP23A is from Hazens Notch formation, taken to the east of the TPC. In thin section, the sample is composed of quartz, albite, muscovite and biotite. Chlorite, opaques, and calcite are found as accessory minerals.

The foliation in this sample is defined by compositional layering (S_n), with quartz and mica layers (Figure 4-5a). Dissolution trails run parallel to the mica cleavage domains. Mica crenulations (S_{n-1}) perpendicular to S_n can be found within layers truncated by dissolution trails. Individual mica grains within layers are small and not well defined, with many not aligned with the overall foliation (S_n). Larger mica grains are found truncated by both microlithon boundaries/dissolution trails. In the Y-Z section (Figure 4-5b), an isoclinal fold is defined by folded quartz and albite microliths, and is parallel to Sn. Its isoclinal and horizontal nature suggests that is an F_n fold, and foliation could be an S_{n-1}/S_n composite.

Quartz grains are found in isolated microlithons, with some exhibiting larger grain sizes. Grains are locally amoeboid, showing variable development of polygonal grain boundaries, suggesting that grain boundary area reduction occurred on grains that formerly experienced grain boundary migration (Figure 4-5a). Locally, evidence for subgrain rotation is preserved in smaller grains within the thin section.

Albite grains can be found both in the mica cleavage domains and quartz microlithons. Inclusion trails in some of the albites locally appear parallel to truncated mica crenulations (S_{n-1}) and the isoclinal fold limbs (Figure 4-5c). Albite crystallization

may have occurred before the formation of S_n based on the observation of inclusion trails that captured patterns parallel to S_{n-1} foliation. Mica tails can be found on some albites. Albite grains are also found locally as boudins.

$^{40}Ar/^{39}Ar$ Step-Heating Results

Two aliquots of single white mica were analyzed from sample 16TP23A (Figure 4-6). Aliquot #1 yielded a plateau age of 451.7 ± 2.0 Ma (1σ). Ages decreased over the course of release of ~36% of the initial ^{39}Ar released from 499 to 459 Ma, after which the remainder of the spectrum defines the plateau. Aliquot #2 instead shows an age gradient of increasing ages from 370 – 457 Ma over the initial ~11% of the ^{39}Ar gas released with remaining steps defining the plateau with an age of 447.5 ± 2.0 Ma (1σ).

4.3 Middle Transect

4.3.1 16PR15A

Microstructures

Sample 16PR15A is from the Hazens Notch Schist formation, on western-central part of the Prospect Rock Fault footwall. In thin section, the sample is mainly composed of quartz and albite, with titanite and opaque grains present as accessory minerals. The sample exhibits spaced foliation, with anastomosing muscovite cleavage domains between quartz and albite microlithons (Figure 4-7a). Locally, some mica grains are highly oblique to the dominant S_n foliation and appear to be truncated by cleavage domains (Figure 4-7b). These could imply foliations prior to the dominant S_n.

Quartz grains are amoeboid, indicating grain boundary migration as the main deformation mechanism. Some grain boundaries are planar, displaying grain boundary area reduction. Rare evidence of subgrain rotation and bulging can also be found in the sample. Large albite grains are present, and show signs of twinning. Inclusion trails are present but are difficult to trace through the grain (Figure 4-7a).

In the Y-Z section, micas are more smoothly anastomosing. Inclusion trails are easier to trace in albites, and the trails are oblique to the dominant foliation, suggesting inclusion trails may have captured older foliations.

$^{40}Ar/^{39}Ar$ Step-Heating Results

Two aliquots of single white mica were analyzed from sample 16PR15A (Figure 4-8). Aliquot #1 did not yield a plateau age. Ages for the initial ~2% of gas release were variable, ranging from c. 454–514 Ma. Subsequent steps show a plateau-like segment, and have a weighted mean average of 431.8 ± 6.6 Ma (1σ). This is concordant with the plateau age from aliquot #2, which yielded a plateau of 428.4 ± 2.6 Ma (1σ). Ages for the initial ~2% of ^{39}Ar gas release are lower than the plateau age (c. 368–406 Ma), as are the ages for the final ~30% of ^{39}Ar gas release (c. 400–411 Ma).

4.3.2 16PR16A

Microstructures

Sample 16PR16A is from the Hazens Notch Formation, on the western side of the Prospect Rock Fault footwall. The thin section is composed of muscovite, quartz, and albite, with small amounts of biotite and chlorite. The dominant S_n foliation is defined by compositional layering of mica and quartz domains (Figure 4-9a). Large albite grains are

found within mica domains. Mica grain orientation and dissolution trails in albites also match the S_n foliation orientation. Individual mica grains roughly parallel to foliation can be seen in quartz domains.

Mica grains are generally thin and small, with larger isolated grains oblique to foliation. Oblique grains are often truncated by the dominant foliation, and may represent a former foliation (S_{n-1}). Three different mica orientations can be noted in thin section. In Y-Z section, crenulations are apparent in the mica domains and albite inclusion trails (Figure 4-9b). Quartz microlithons are finer grained than mica domains.

Quartz grains are mostly amoeboid, though some grain edges are planar or seem formerly planar (Figure 4-9a). Grain boundary migration may have been the dominant deformation mechanism, and planar grain boundaries suggest some degree of grain boundary area reduction. Subgrains appear locally in some of the quartz grains, indicating sub grain rotation. Albites grains appear as porphyroclasts in mica microlithons. Some grains exhibit twinning or minor chloritization. Albite inclusion trails generally match the orientation of surrounding mica.

$^{40}Ar/^{39}Ar$ Step-Heating Results

Two aliquots of single grain of white mica were analyzed from sample 16PR16A (Figure 4-10). Aliquot #1 yielded a plateau age of 431.5 ± 2.6 Ma (1σ). Ages decreased from c. 471-449 Ma for the initial ~16% of ^{39}Ar gas release, including a low second step at ~432 Ma; following steps defined the plateau. Aliquot #2 yielded a plateau age of 427.1 ± 2.8 Ma (1σ) with a reasonably flat spectrum. Initial steps (~4% of initial ^{39}Ar gas release) yielded ages of 398 Ma and 448 Ma. The final steps (final ~16% of ^{39}Ar gas

release) were not included in the plateau age calculation, and had ages of 398 Ma and 421 Ma.

4.3.3 16PR21A

Microstructures

Sample 16PR21A is from the Fayston Formation, taken from the middle transect of the PRF footwall. The thin section is largely composed of quartz, muscovite, and biotite, and exhibits anastomosing spaced foliation (S_n). Dissolution trails also help to define S_n (Figure 4-11a). Quartz and mica microlithons are separated by mica cleavage domains. Medium to large sized albite grains are found locally in quartz microlithons. Mica grains are very fine grained.

In the X-Z section, crenulations can be found within smaller truncated microlithons and cleavage domains, defining S_{n-1} (Figure 4-6A). In Y-Z section, a crenulation cleavage is apparent in mica microlithons, defining S_{n+1} (Figure 4-11b). Quartz grains are small to medium sized within microlithons. Quartz grains are generally amoeboid but occasionally exhibit planar edges, indicating deformation via grain boundary migration deformation and later grain boundary area reduction.

Large albite grains are present locally in quartz microlithons. Inclusion trails within the albite parallel S_n, and in Y-Z section capture crenulations. Albite grains also appear bent, and match the anastomosing foliation with its geometry.

$^{40}Ar/^{39}Ar$ Step-Heating Results

Two aliquots of single white mica grains were analyzed from sample 16PR21A (Figure 4-12). Aliquot #1 yielded a plateau age of 432.0 ± 2.1 Ma (1σ). Ages for the

initial ~65% of ^{39}Ar gas release defined the plateau. The following 14% of ^{39}Ar gas release (next two steps) were not included in the plateau calculations, and had ages of 411 Ma and 410 Ma. The final step had an age concordant with the plateau age (429 Ma), but was not included in the plateau calculation. Aliquot #2 did not yield a plateau age. Step ages generally fluctuated between ~439–416 Ma, with a weighted mean average of 426.9 ± 5.8 (1σ). Two steps at 467 Ma and at 387 Ma were excluded from the calculation.

4.3.4 16PR28A

Microstructures

Sample 16PR28A is from the Hazens Notch formation, on the eastern side of the Prospect Rock Fault footwall. The thin section is largely dominated by quartz microlithons, with mica cleavage domains containing both biotite and white mica. The dominant foliation appears as spaced foliation (S_n). Albite appears as large grains and boudins. Opaque minerals, potentially magnetite, are present as accessory minerals.

Spaced foliation (S_n) is defined by dissolution seams and mica cleavage domains, and is generally anastomosing (Figure 4-13a). S_{n-1} foliation appears as crenulated mica domains trapped between the main foliation. Axial planes to crenulations appear parallel to S_n. In the Y-Z section (Figure 4-13b), mica cleavage domains are bent into crenulations (S_{n+1}), trending differently than those found in the X-Z section.

Mica grains are generally small and thin. Quartz grains are small to medium sized, and appear either amoeboid or polygonal, recording evidence for both grain boundary migration and local grain boundary area reduction. Albite grains are present in the quartz domains, exhibit deformation twinning, and can be locally found as boudin

chains (Figure 4-13a). Inclusion trails within albite grains define an internal foliation locally perpendicular to the dominant external S_n, suggesting preservation of S_{n-1}. In the Y-Z section, crenulations parallel to S_{n+1} are captured in the inclusion trails.

$^{40}Ar/^{39}Ar$ Step-Heating Results

Two aliquots of white mica were analyzed from sample 16P28A, with aliquot #1 utilizing a single grain and aliquot #2 utilizing two grains (Figure 4-14). Aliquot #1 did not yield a plateau age. Ages increased from ~339 to 440 Ma in 5-72% of the initial ^{39}Ar gas release, and then decreased to ~375 Ma over the rest of the gas release. A large percentage of steps fell between 400-440 Ma. A weighted mean average of those steps was calculated at 416.6 ± 8.0 Ma (1σ). Aliquot #2 yielded with a plateau age of 447.8 ± 2.1 Ma (1σ). Steps within the plateau fluctuated between ~432–464 Ma. The initial step (~2% of initial ^{39}Ar gas release) was not included in the plateau, and had an age of ~424 Ma.

4.4 Southern Transect

4.4.1 16PR05A

Microstructures

Sample 16PR05A is from the Hazens Notch formation, on the western limits of the Prospect Rock Fault footwall. In thin section, the sample is composed of quartz, muscovite and biotite, with small undeformed garnet porphyroclasts and rare large albite grains. The sample exhibits spaced foliation, with mica and quartz microlithons and cleavage domains defined by parallel mica and pressure solution seams (Figure 4-15). An

S-C' fabric is apparent from the anastomosing and truncated foliations in the X-Z section. The sample foliation was recorded as 176º/23º (Az), with lineations as 266º/23º. S-C' fabric is consistent with a top-to-the-east sense of movement. In this sample the dominant foliation and lineation dip towards the west, thus top-to-the-east shear aligns with apparent reverse motion.

Mica grains are thin and small, though chlorite grains are larger. Local large mica grains appear oblique to the foliation, and are truncated by dissolution seams. Grains could represent an older foliation, but are not frequent enough to be conclusive.

Quartz grains appear either polygonal or amoeboid, suggesting the occurrence of grain boundary area reduction and grain boundary migration (Figure 4-15). Few grains exhibit subgrains and small protrusions on their edges, suggesting that subgrain rotation and bulging also occurred as a part of deformation. Most grains are small to medium in size. Albite grains appear elongated, and are bound by dissolution seams.

$^{40}Ar/^{39}Ar$ Step-Heating Results

Two aliquots of white mica were analyzed from sample 16PR05A. Aliquot #1 did not yield a plateau age, and produced large range of ages, from between 30 and 405 Ma (Figure 4-16). Ages mostly fell between three age brackets: 352–405 Ma, 197–245 Ma, and 28–89 Ma. A weighted mean average of 383 ± 100 Ma (1σ) was calculated. Aliquot #2 yielded a reasonably flat spectrum, with a plateau age of 419.3 ± 2.4 Ma (1σ, Figure 4-17). The first two steps (~3% of the initial ^{39}Ar gas released) decreased from ~509–456 Ma, after which the remainder of the spectrum defines the plateau.

4.4.2 16PR33A

Microstructures

Sample 16PR33A is from the Hazens Notch Formation, from the southern section of the Prospect Rock Fault footwall. The sample is largely composed of quartz, mica, and albite, with very small amounts of garnet. The spaced foliation (S_n) in the sample is slightly anastomosing, and composed of quartz + albite domains, separated by mica microlithons and cleavage domains (Figure 4-18). Mica microlithons are composed of muscovite and biotite.

Mica grains are predominantly thin and small, with locally large mica grains in mica microlithons often appearing oblique to the foliation. These either represent static recrystallization or an older foliation. In the Y-Z section, mica microlithons and cleavage domains are more anastomosing. Quartz microlithons are thin, from 1–4 grains thick. Quartz grains are medium to large in size, and generally amoeboid, suggesting grain boundary migration as the main deformation mechanism. Polygonal quartz grains are also not uncommon, implying the occurrence of grain boundary area reduction.

Albite grains are large, and generally sigmoidal in shape. Some grains are show deformational twinning, and are pinned between mica and quartz microlithons. Inclusion trails internal to albites are locally continuous with the external S_n. Wing-like muscovite and biotite structures can be found on the edges of albite grains (Figure 4-18).

$^{40}Ar/^{39}Ar$ Step-Heating Results

Two aliquots of single white mica were analyzed from sample 16PR33A (Figure 4-19). Aliquot #1 yielded a plateau of 420.0 ± 2.7 Ma (1σ), with ages decreasing from

~433–408 Ma over the plateau. The final step was not included in the plateau, and had an age of ~395 Ma. Aliquot #2 yielded a plateau of 428.7 ± 2.9 Ma (1σ), with ages increasing from 440-465 Ma over the first four steps (initial ~18% of ^{39}Ar gas release, steps not included in plateau). The remainder of the steps in the spectrum defined the plateau.

4.4.3 16PR04B

Microstructures

Sample 16PR04B is a quartzite member of the Hazens Notch formation, taken from the southern part of the Prospect Rock Fault footwall. The sample is almost entirely composed of quartz, with small grains of biotite and white mica. Foliation in the X-Z section is defined by mica orientation (Figure 4-20). In the Y-Z section, there is no semblance of foliation.

Quartz grains are small and appear with small bulged edges, suggesting bulging as the main deformation mechanism (Figure 4-20). Some subgrains and polygonal edges can be found on some quartz grain, indicating some subgrain rotation and grain boundary area reduction has occurred. A band of highly deformed quartz cuts the thin section oblique to foliation.

^{40}Ar/^{39}Ar Step-Heating Results

Two aliquots of white mica were analyzed from sample 16PR04B (Figure 4-21). Aliquot #1 did not yield a plateau. Ages decreased from 427 to 382 Ma. A weighted mean average of steps with ages older than 400 Ma yielded an age of 422 ± 8.6 Ma (1σ). Aliquot #2 utilized three grains, but did not yield enough Ar gas to generate an age.

Table 4 - 1 : Major Microstructures Observed and Calculated Plateau ages in Northern Transect Samples
Foliation is described via Right Hand Rule (RHR)

Northern Transect	16PR29A	16PR08A	16TP23A
Dominant foliation (Sn) defined by	Spaced foliation	Spaced foliation	Compositional layering
Orientation of S_n (RHR) and L_n (T/P)	358º/40º, 080º/40º	112º/74º, 290º/13º	020º/68º, 021º/02º
Present secondary foliations	None	S_{n-1}	S_{n-1}
Secondary foliations defined by	None	Truncated mica domains, truncated mica grains	Truncated mica domains, albite inclusion trails
Dominant quartz microstructures	Grain boundary migration, subgrain rotation	Grain boundary migration, subgrain rotation	Grain boundary area reduction
Dominant albite microstructures	None	None	Mica-winged albite
Kinematic indicators	S-C' shear fabrics (top-to-the-west)	None	None

Northern Transect	16PR29A	16PR08A	16TP23A
Aliquot #1	457.6 ± 2.0 Ma	458.6 ± 2.0 Ma	451.7 ± 2.0 Ma
Aliquot #2	No Plateau	456.7 ± 1.8 Ma	447.5 ± 2.0 Ma

Table 4 - 2 : Major Microstructures Observed and Calculated Plateau ages in Middle Transect Samples
Foliation is described via Right Hand Rule (RHR)

Middle Transect	16PR15A	16PR16A	16PR21A	16PR28A
Dominant foliation (S_n) defined by	Spaced Foliation	Compositional Layering	Spaced Foliation	Spaced Foliation
Present secondary foliations	S_{n-1}	S_{n+1}, S_{n-1}	S_{n+1}, S_{n-1}	S_{n+1}, S_{n-1}
Orientation of S_n (Az) and L_n (T/P)	130º/10º, 220º/10º	208º/18º, 009º/09º	010º/19º, 097º/19º	027º/65º, 149º/61º
Secondary foliation (Sn-1) defined by	Albite Inclusion Trails, Truncated Mica grains	Truncated Mica Grains	Truncated Mica Crenulations	Truncated Mica and Albite Crenulations
Secondary foliation (Sn+1) defined by	None	Mica and Albite Crenulations	Mica Crenulations	Mica Crenulations
Dominant quartz microstructures	Grain Boundary Migration	Grain Boundary Area Reduction (on formerly GBM grains)	Grain Boundary Area Reduction, Grain Boundary Migration	Grain Boundary Area Reduction, Grain Boundary Migration
Dominant albite microstructures	Inclusion Trails	Possible Mica Wings	Inclusion Trails, Grains follow Foliation	Inclusion Trails, sigmoidal grains, boudin chains
Kinematic indicators	None	None	None	None

Middle Transect	16PR15A	16PR16A	16PR21A	16PR28A
Aliquot #1	No Plateau	431.5 ± 2.6 Ma	432.0 ± 2.1 Ma	No Plateau
Aliquot #2	428.4 ± 2.6 Ma	427.1 ± 2.8 Ma	No Plateau	447.8 ± 2.1 Ma

Table 4-3 : Major Microstructures Observed and Calculated Plateau ages in Southern Transect Samples
Foliation is described via Right Hand Rule (RHR)

Southern Transect	16PR05A	16PR33A	16PR04B
Dominant foliation (Sn) Defined by	Spaced foliation	Spaced foliation	Spaced foliation
Orientation of S_n (Az) and L_n (T/P)	176º/23º, 266º/23º	162º/59º, 256º/59º	014º/35º, 104º/35º
Present secondary foliation	None	S_{n-1}	None
Secondary foliation defined by	None	Truncated mica domain	None
Dominant quartz microstructures	Grain boundary area reduction, grain boundary migration	Grain boundary migration, subgrain rotation	Bulging, grain boundary migration
Dominant albite microstructures	Follow foliation	Mica wings	None
Kinematic indicators	S-C' shear fabric	None	None

Southern Transect	16PR05A	16PR33A	16PR04B
Aliquot #1	No Plateau	420.0 ± 2.7 Ma	No Plateau
Aliquot #2	419.3 ± 2.4 Ma	428.7 ± 2.9 Ma	Insufficient Gas Produced

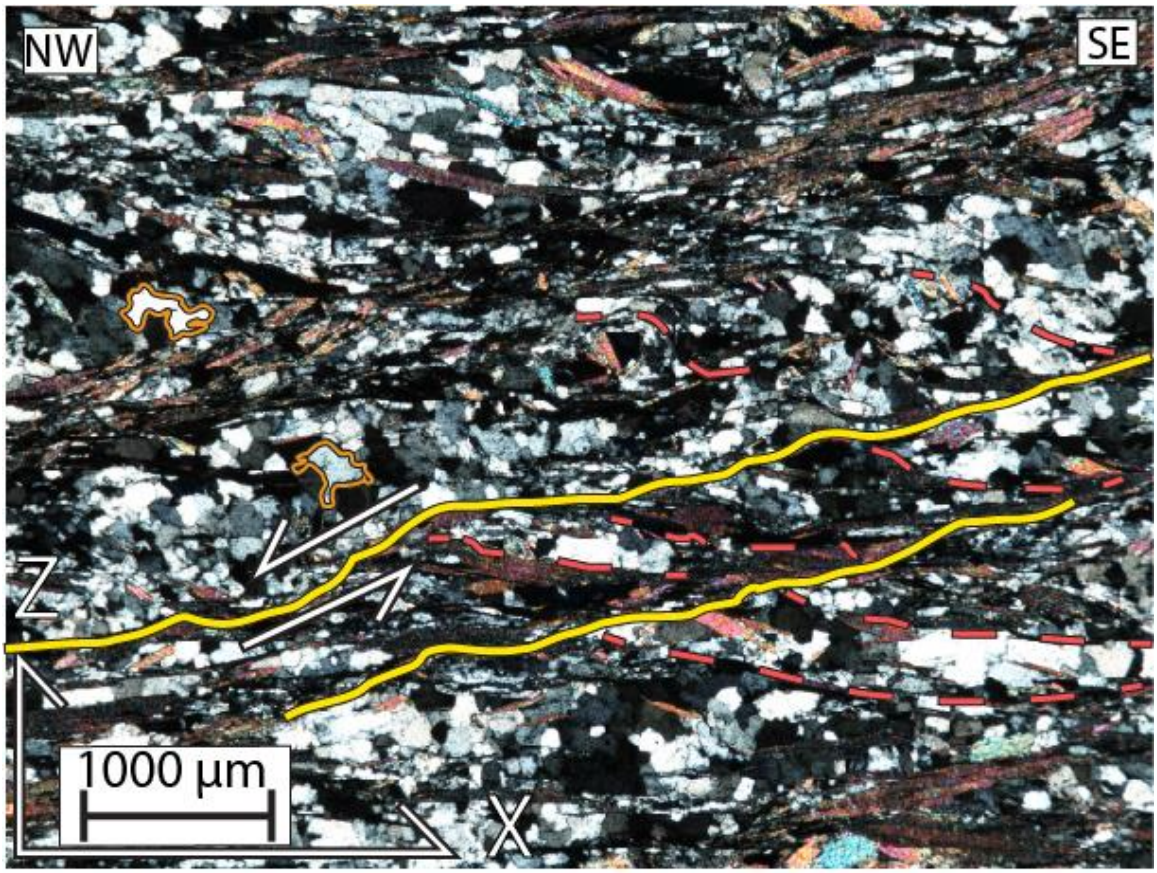

Figure 4-1: X-Z section of sample 16PR29A displaying S-C' fabrics. C' shear bands (yellow) can be identified as having deformed mica cleavage domains and quartz microlithons, offsetting the foliation (S, red). Inferred direction of motion is indicated by the white arrows. Quartz grains are generally amoeboid (orange). Mica grains oblique to foliation can also be noted beneath the S-C' fabric. Sample orientation is provided on table 4-1, and data are consistent with top-to-the-west motion.

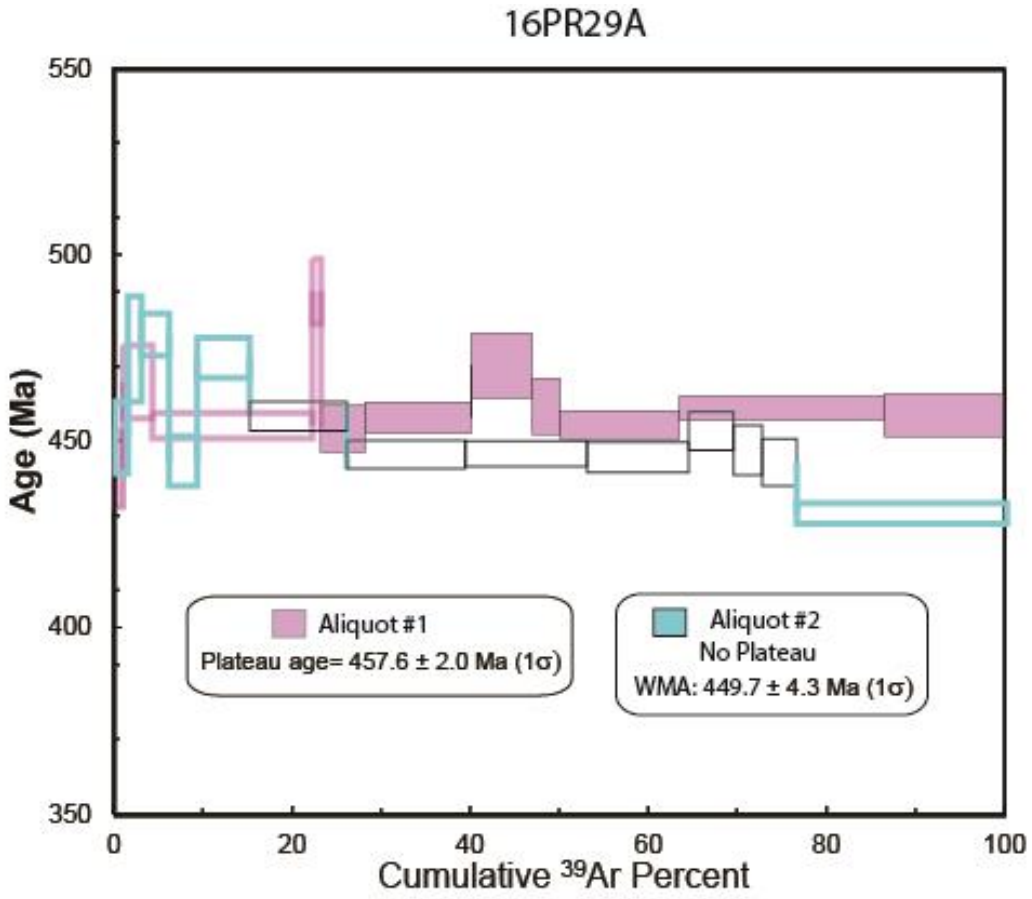

Figure 4-2: Apparent $^{40}Ar/^{39}Ar$ spectra of muscovite from sample 16PR29A, a schist of the Hazens Notch Formation. Box heights, weighted mean averages, and quoted errors are reported at the 1σ level. Shaded boxes define reported plateau ages, and outlined colored boxes were excluded from plateau calculations. Black boxes define steps utilized to calculate the weighted mean average in aliquot 2. A single muscovite grain was analyzed per aliquot.

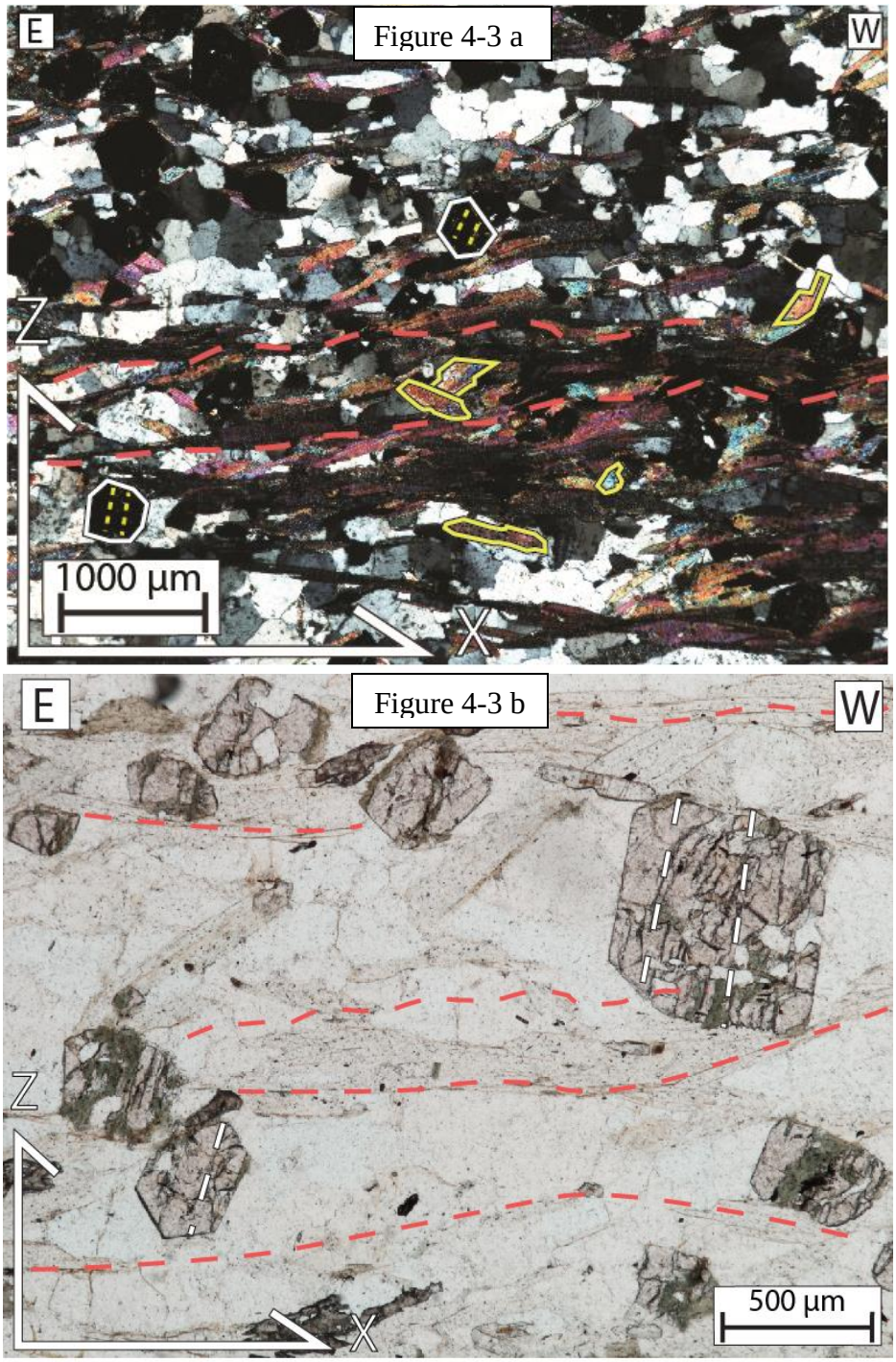

Figure 4-3: a. X-Z section of sample 16PR08A in cross polarized light. Spaced foliation (red), S_n, is defined by mica cleavage domains and quartz microlithons. Foliation is slightly anastomosing. Truncated micas (yellow), and could represent earlier foliations. b. X-Z section of sample 16PR08A in plain polarized light. Garnets can be observed, with fractures (white dashed lines) roughly perpendicular to foliation (red).

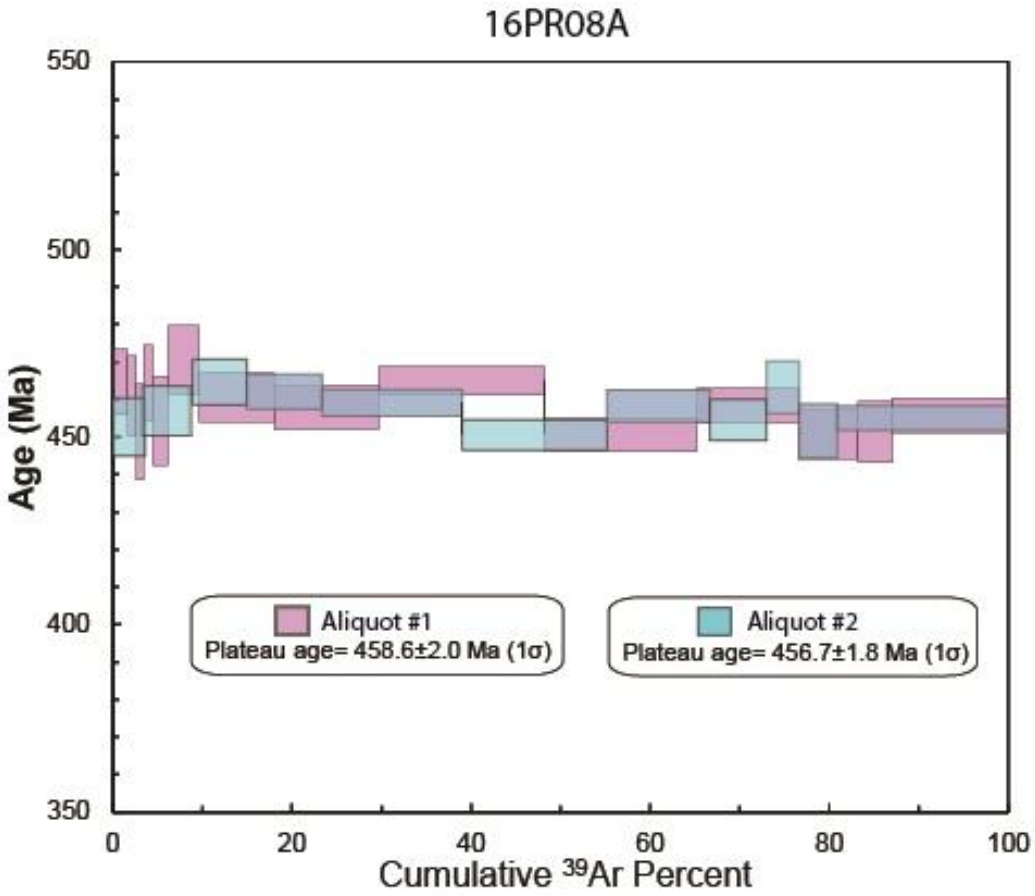

Figure 4-4 : Apparent $^{40}Ar/^{39}Ar$ spectra of muscovite from sample 16PR08A, a schist of the Hazens Notch Formation. Box heights, weighted mean averages (WMA), and quoted errors are reported at the 1σ level. Shaded boxes define reported plateau ages, and outlined boxes were excluded from plateau calculations. A single muscovite grain was analyzed per aliquot.

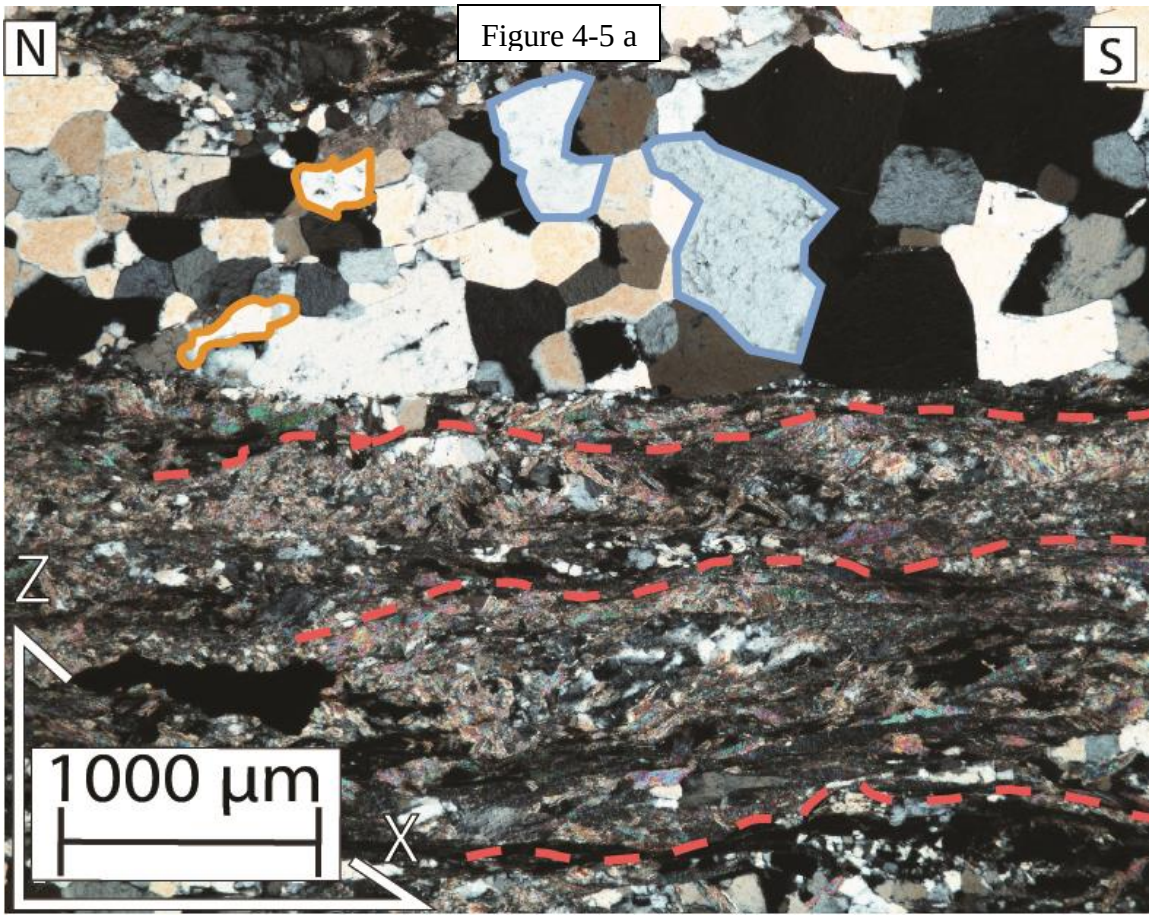

Figure 4-5: a. X-Z section of sample 16TP23A. Foliation (S_n, red) is defined by compositional layers of quartz and mica. Quartz grains show sign of grain boundary area reduction (polygonal grain boundaries) on grains that appear formerly amoeboidal (grain boundary migration). Grain boundary area reduction may have occurred on quartz grains formerly deformed by grain boundary migration.

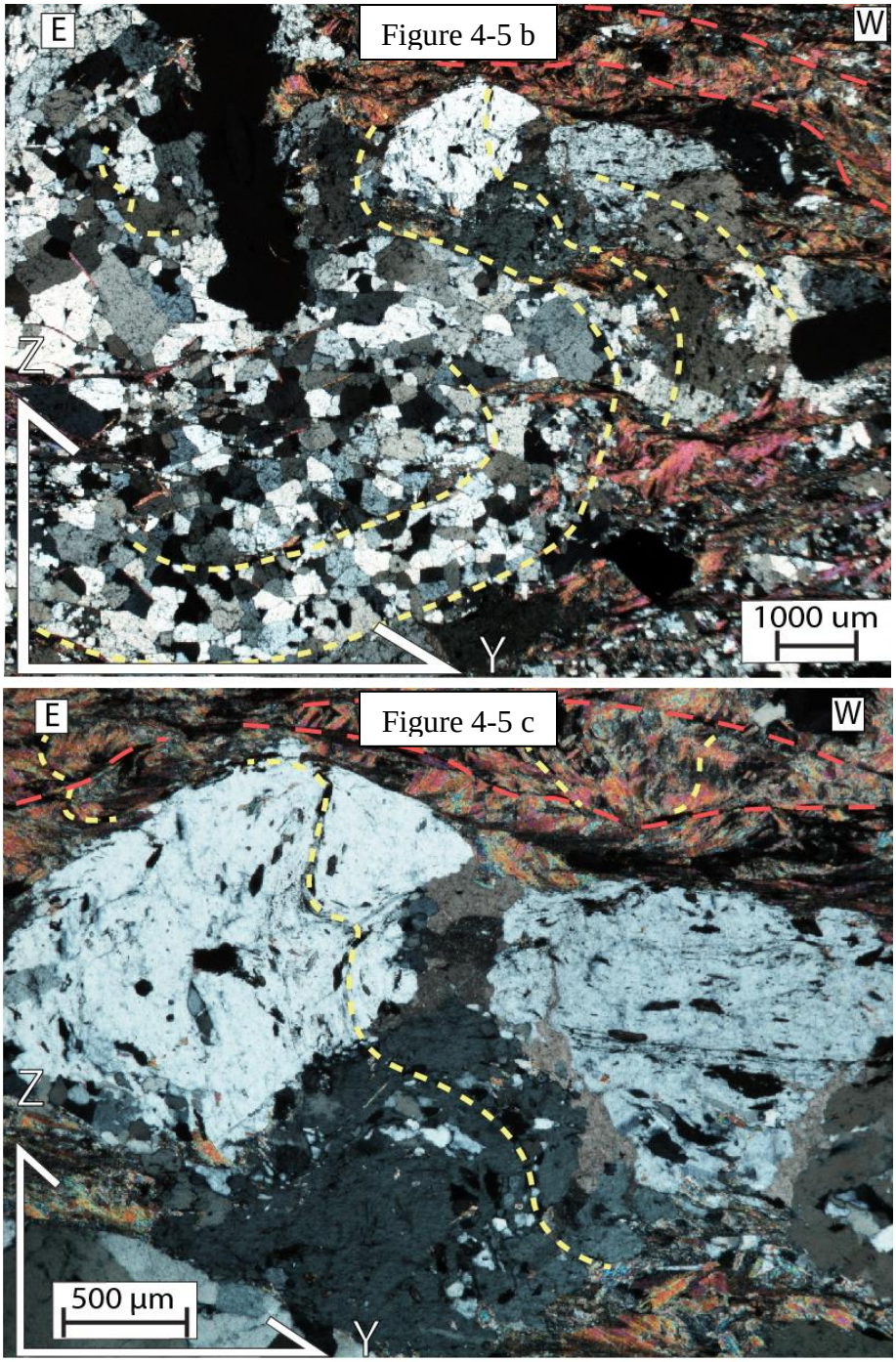

Figure 4-5: b.Y-Z section of sample 16TP23A. Quartz layers, albite grains and inclusion trails, and mica orientation (yellow) are not parallel to horizontal dissolution trails (S_n, red). On a larger scale, the fold appears as isoclinal and parallel to S_n, indicating an F_n fold. c. Y-Z section of sample 16PR29A. S_n is denoted by dissolution trails, though mica orientation between the dissolution trails are oblique to S_n and define S_{n-1}. Inclusion trails within albites are folded, and parallel to S_{n-1}.

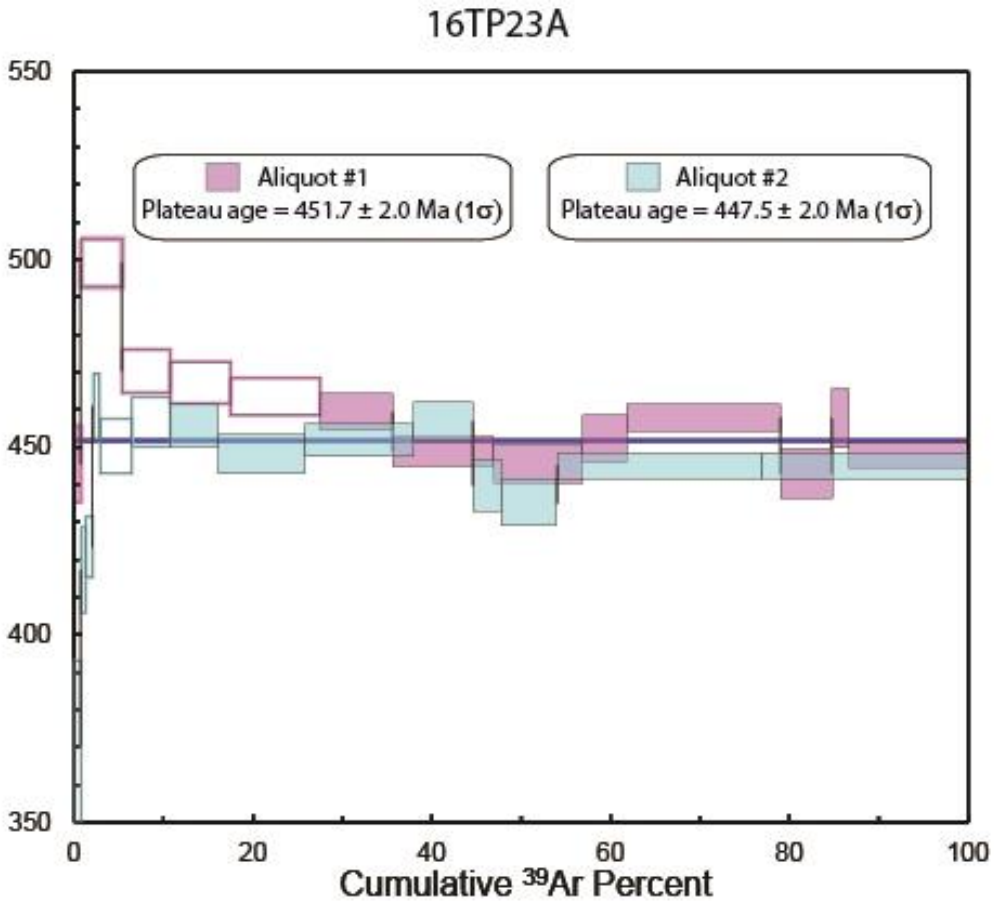

Figure 4-6: Apparent $^{40}Ar/^{39}Ar$ spectra of muscovite from sample 16TP23A, , a schist of the Hazens Notch Formation. Shaded boxes define reported plateau ages, and outlined boxes were excluded from plateau calculations. A single muscovite grain was analyzed per aliquot.

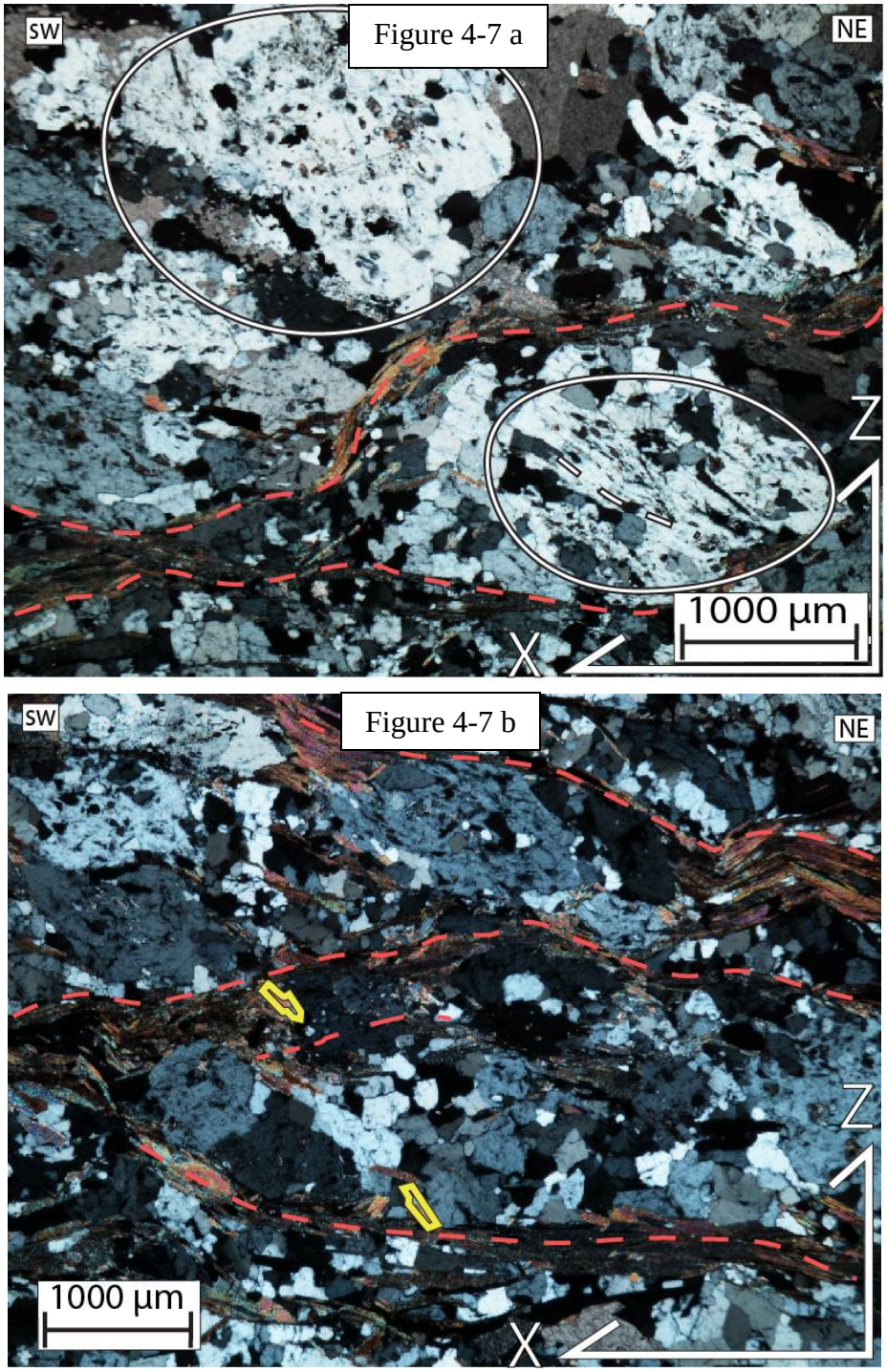

Figure 4-7: a. X-Z section of sample 16PR15A. Anastomosing spaced foliation (red) is defined by mica cleavage domains. Albites (circled) contain inclusion trails that are difficult to trace (white dashed line), though appear locally oblique to foliation. b. X-Z section of sample 16PR15A. Individual mica grains appear highly oblique to foliation, and appear to be truncated by cleavage domains.

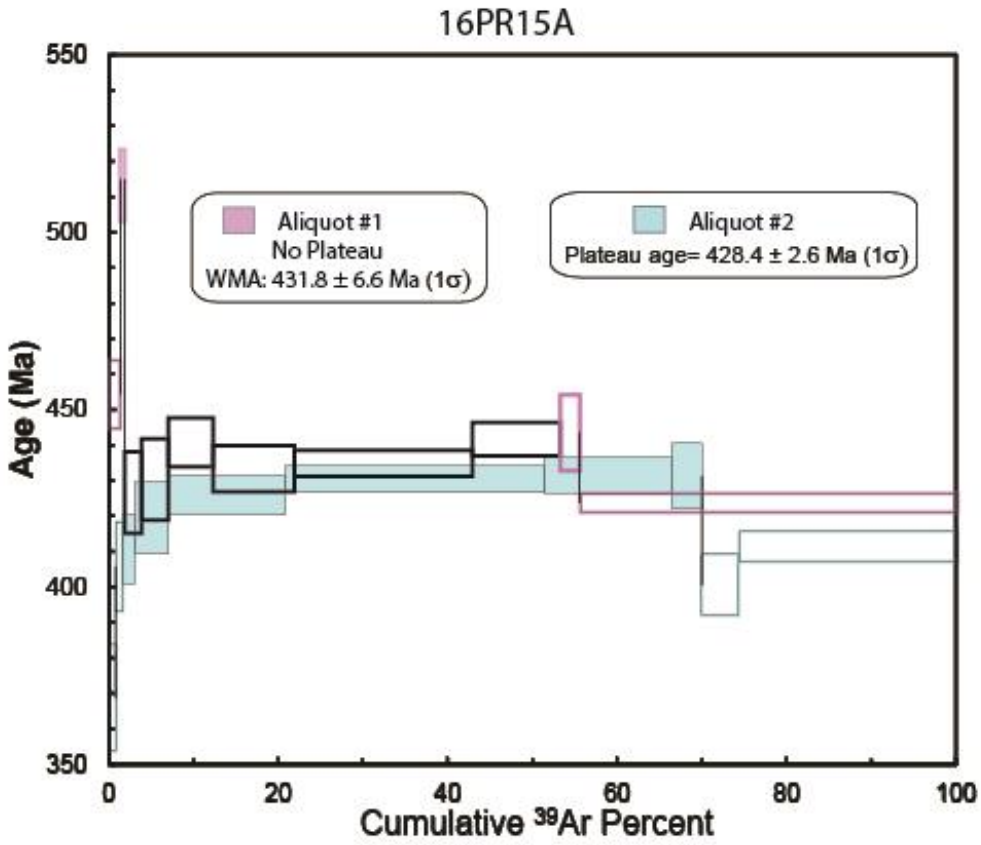

Figure 4-8: Apparent $^{40}Ar/^{39}Ar$ spectra of muscovite from sample 16PR15A, a Hazens Notch Formation Schist. Box heights, weighted mean averages, and quoted errors are reported at the 1σ level. Shaded boxes define reported plateau ages, and outlined colored boxes were excluded from plateau calculations. Black boxes define steps utilized to calculate the weighted mean average in aliquot 1. A single muscovite grain was analyzed per aliquot.

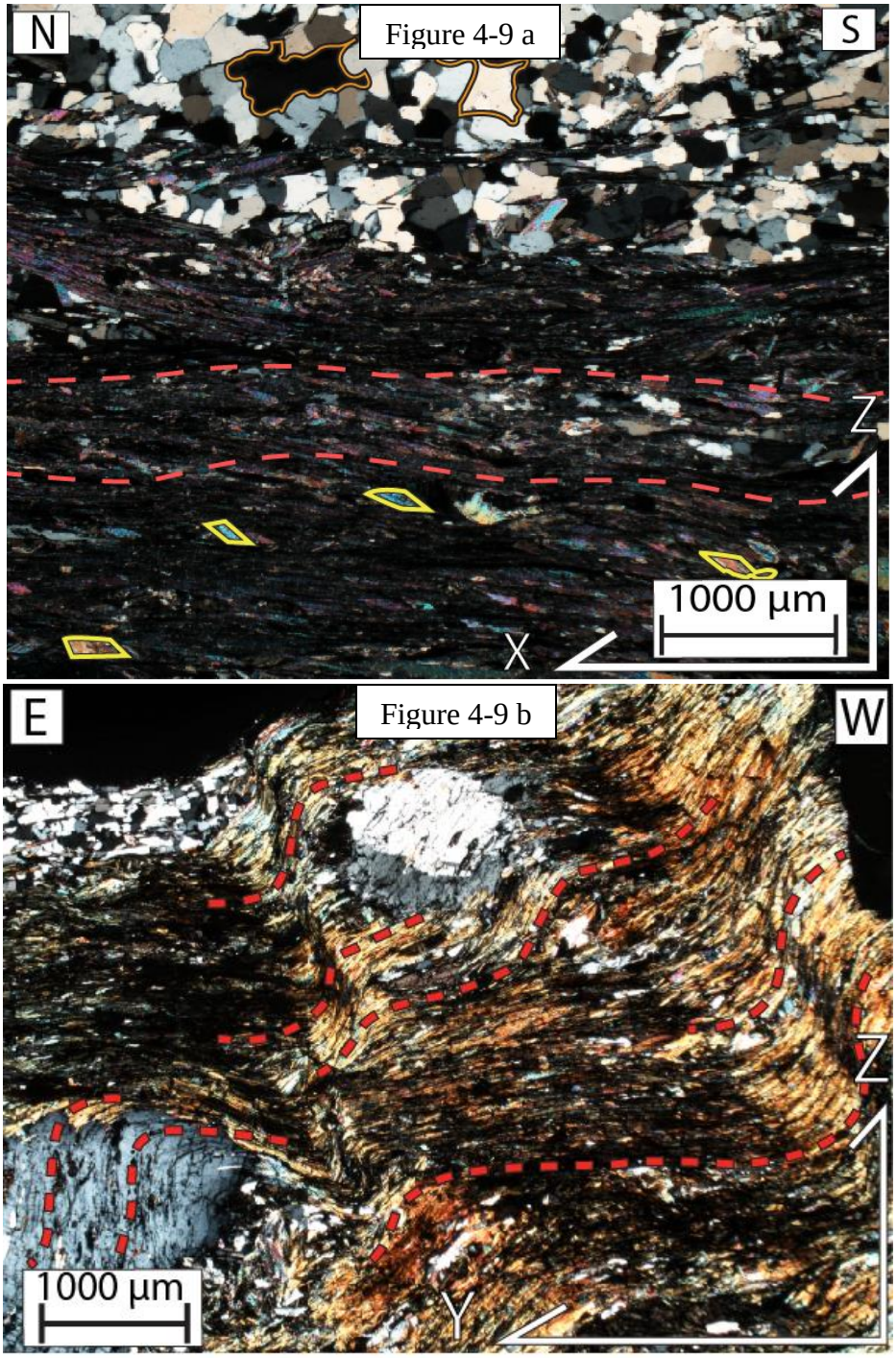

Figure 4-9: a. X-Z section of sample 16PR16A. Foliation is defined by compositional layering (S_n, red). Individual mica grains (purple) are locally oblique to foliation. b. Y-Z section of sample 16PR16A. Crenulations fold the dominant foliation and dissolution trails, and inclusion trails in mica follow the same pattern (red). Inclusion trail patterns in the albite match S_{n+1}, and therefore suggest to post-kinematic formation of albite with respect to development of S_n.

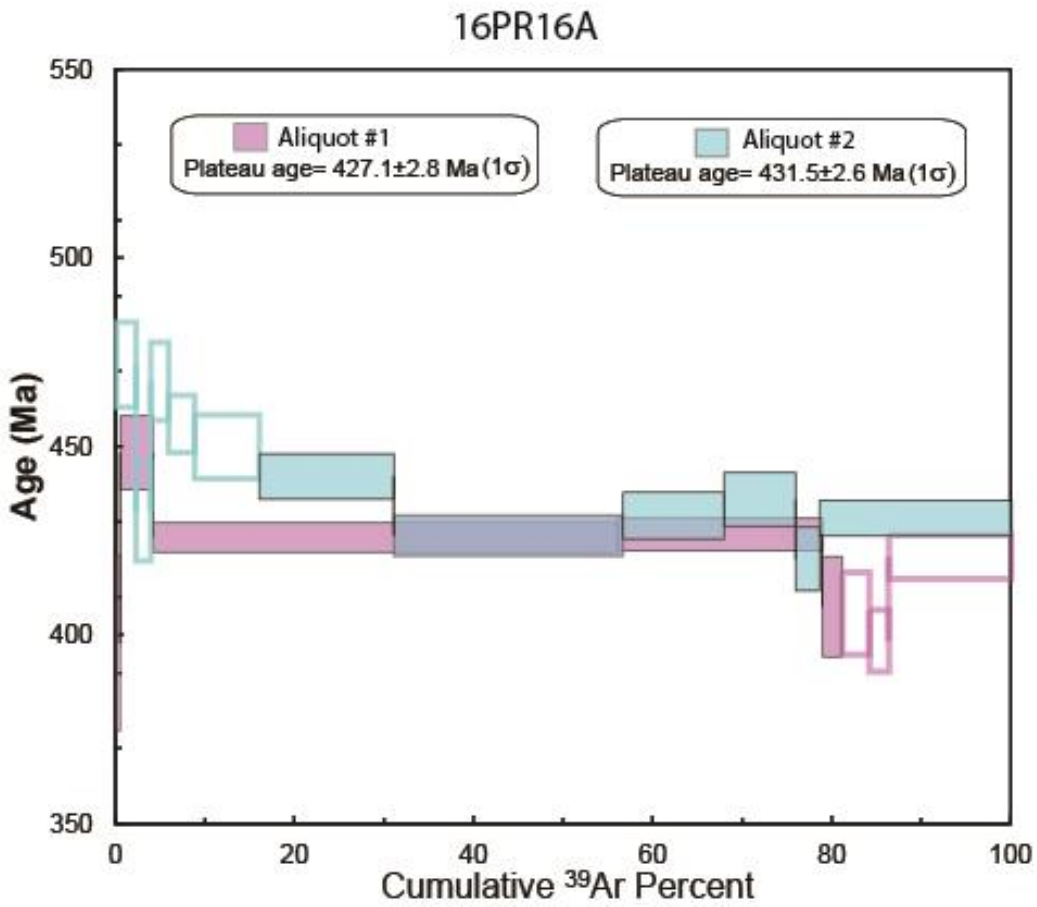

Figure 4-10: Apparent $^{40}Ar/^{39}Ar$ spectra of muscovite from sample 16PR16A, , a schist of the Hazens Notch Formation. Box heights and quoted errors are reported at the 1σ level. Shaded boxes define reported plateau ages, and outlined boxes were excluded from plateau calculations. A single muscovite grain was analyzed per aliquot.

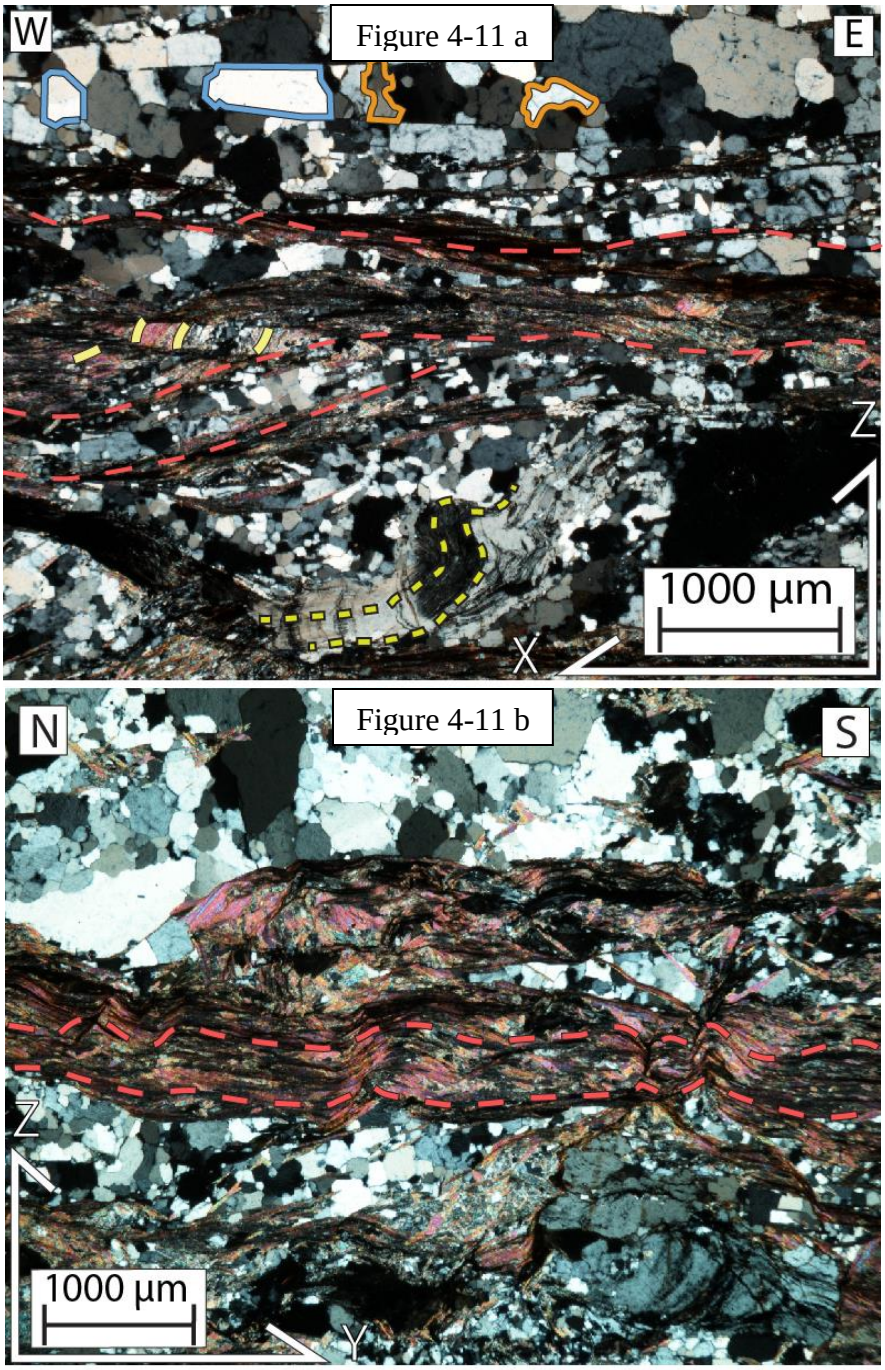

Figure 4-11: a. The X-Z section of sample 16PR21A. Both amoeboid and polygonal quartz grains can be seen, suggesting grain boundary migration and grain boundary area reduction. Crenulations can be noted within the mica microlithons (yellow), and are oblique to and truncated by the dominant foliation (red). Inclusion trails (dashed yellow) can be noted within an albite grain, and appear parallel to the mica crenulations. b. Y-Z section of sample 16PR21A. The dominant foliation, defined by mica cleavage domains and dissolution trails, is crenulated (red).

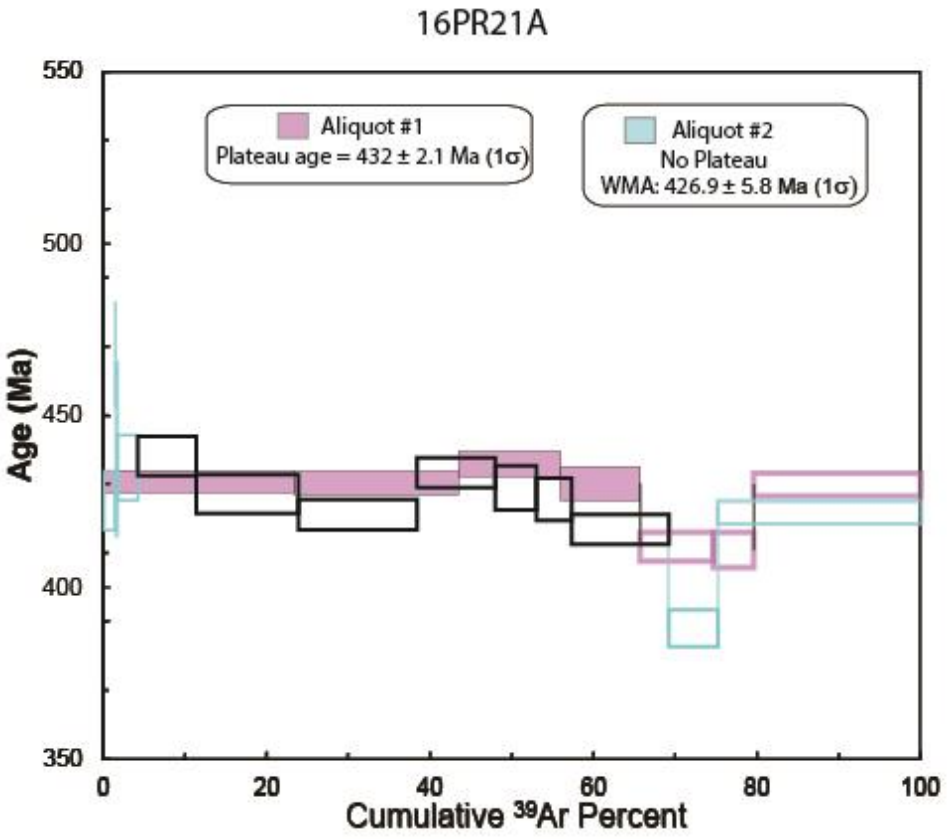

Figure 4-12: Apparent $^{40}Ar/^{39}Ar$ spectra of muscovite from sample 16PR21A, , a schist of the Hazens Notch Formation. Box heights, weighted mean averages, and quoted errors are reported at the 1σ level. Shaded boxes define reported plateau ages, and outlined colored boxes were excluded from plateau calculations. Black boxes define steps utilized to calculate the weighted mean average in aliquot 2. A single muscovite grain was analyzed per aliquot.

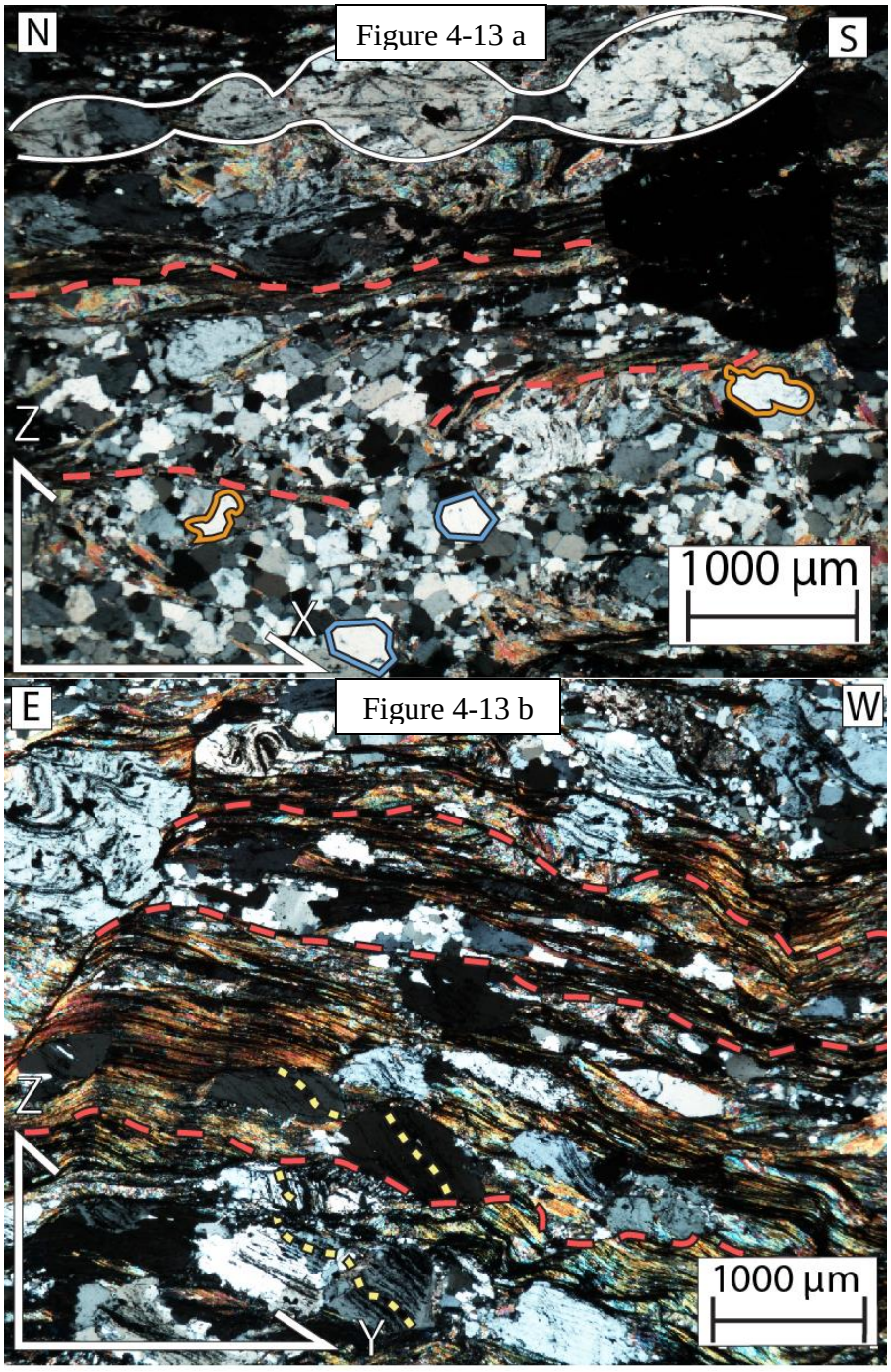

Figure 4-13: a. X-Z section of sample 16PR28A. Spaced foliation (red) is defined through dissolution seams and mica cleavage domains, and is generally anastomosing. Quartz grains exhibit grain boundary migration (orange) and grain boundary area reduction (blue). Horizontal albite boudins are roughly parallel to S_n. b. Crenulations in the dominant foliation can be seen in Y-Z section, with the crenulation axis perpendicular to dominant foliation. Inclusions in albites locally appear to define and include crenulation cleavage.

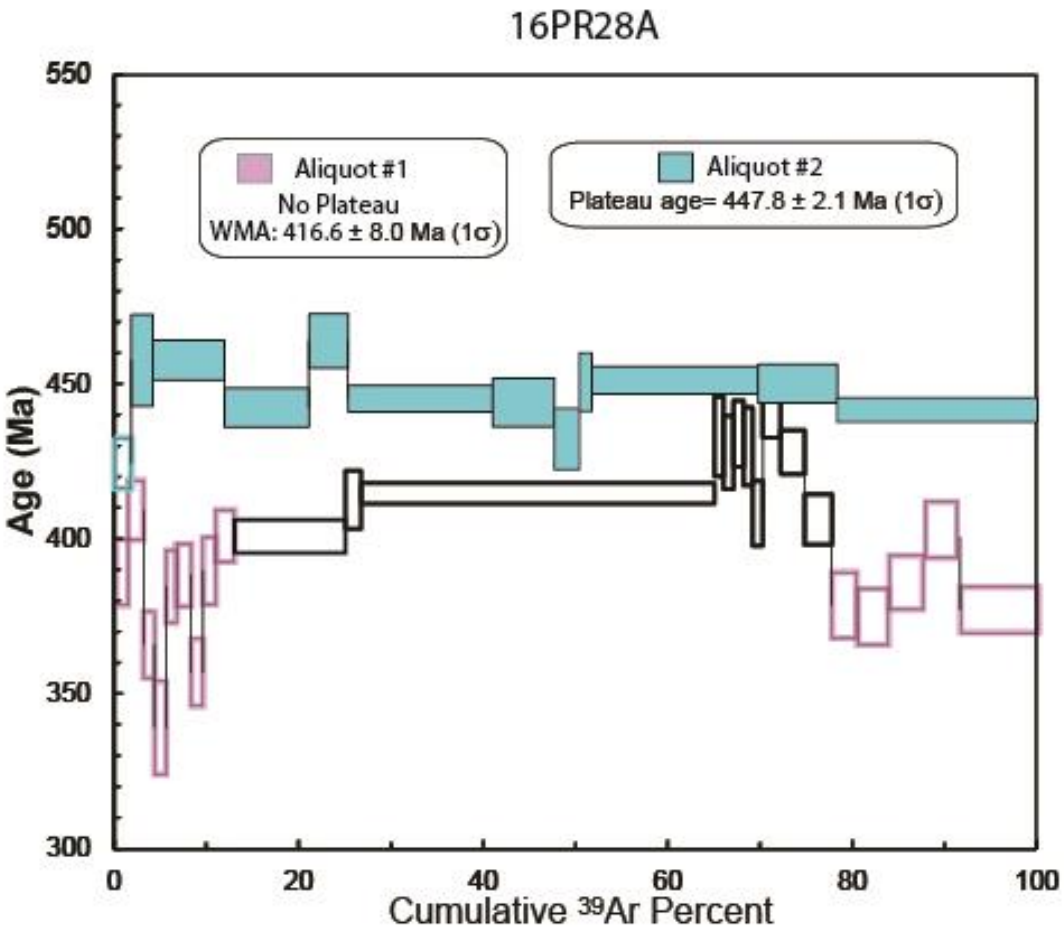

Figure 4-14: Apparent $^{40}Ar/^{39}Ar$ spectra of muscovite from sample 16PR28A, a schist of the Hazens Notch Formation. Box heights, weighted mean averages, and quoted errors are reported at the 1σ level. Shaded boxes define reported plateau ages, and outlined colored boxes were excluded from plateau calculations. Black boxes define steps utilized to calculate the weighted mean average in aliquot 1. A single grain was analyzed for the first aliquot, and two grains for the second.

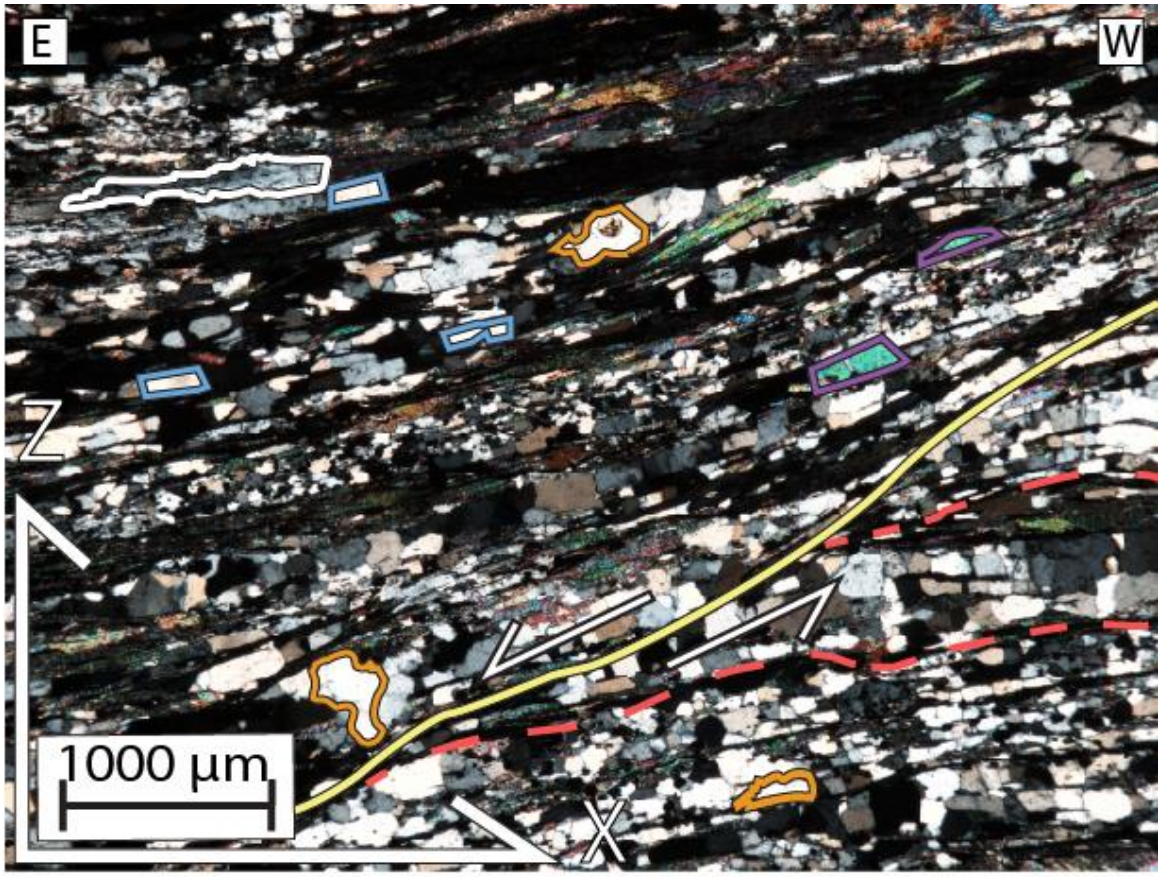

Figure 4-15: X-Z section of sample 16PR05A. Quartz microlithons defining the foliation (S_n, red) are truncated by S-C' shear bands (yellow). Both amoeboid (orange) and polygonal (blue) quartz grains can be seen, suggesting the occurrence grain boundary migration and grain boundary area reduction. Albite grains are found with the microlithons (white), with grains appearing flattened.

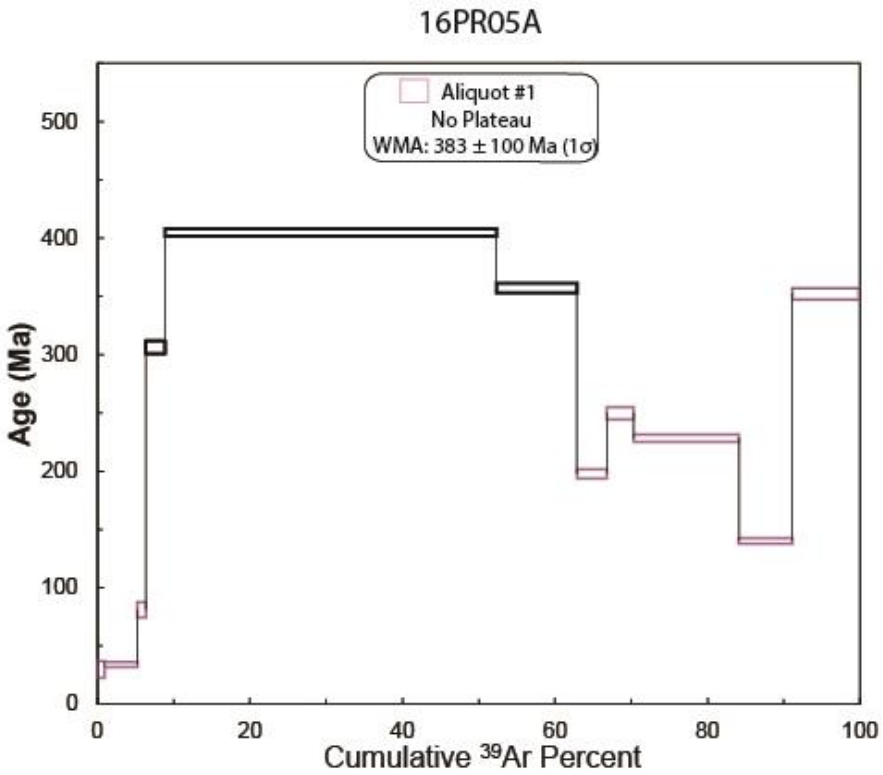

Figure 4-16: An apparent $^{40}Ar/^{39}Ar$ spectrum of muscovite from sample 16PR05A, a schist of the Hazens Notch Formation. Box heights, weighted mean averages, and quoted errors are reported at the 1σ level. Outlined colored boxes were excluded from plateau calculations. Black boxes define steps utilized to calculate the weighted mean average in aliquot 2. A single muscovite grain was analyzed for this aliquot.

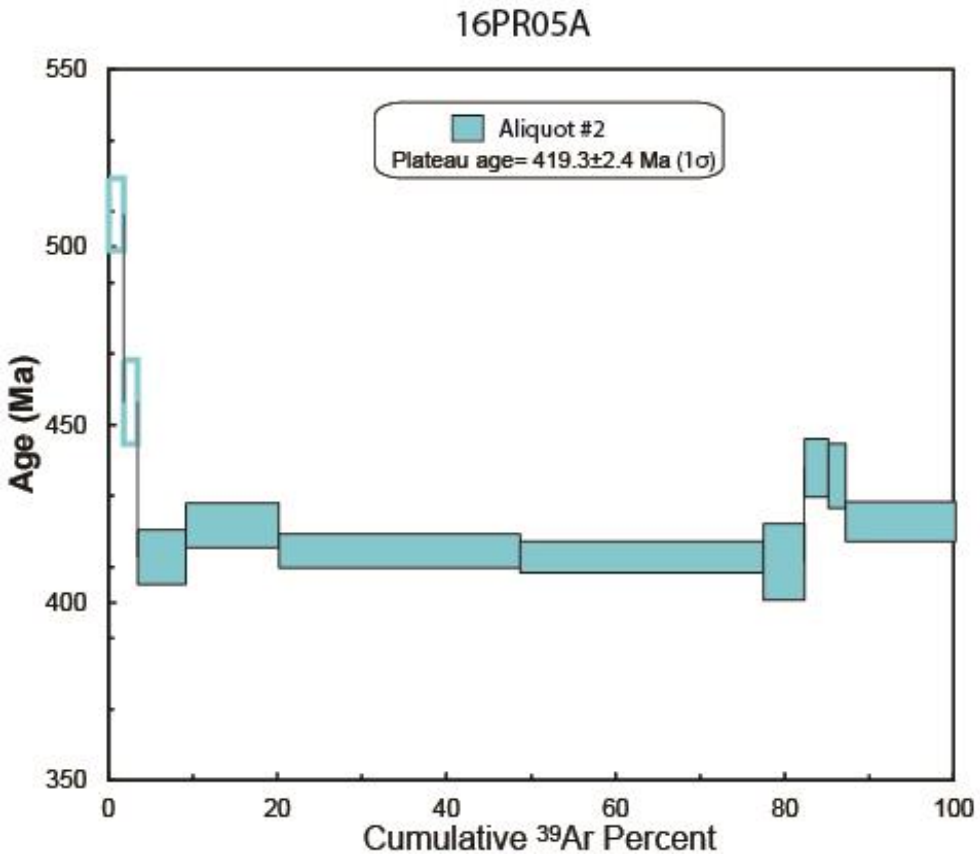

Figure 4-17: Apparent $^{40}Ar/^{39}Ar$ spectrum of muscovite from sample 16PR05A, a schist of the Hazens Notch Formation. Box heights and quoted errors are reported at the 1σ level. Shaded boxes defined reported plateau ages, and outlined boxes were excluded from plateau calculations. A single muscovite grain was analyzed for this aliquot.

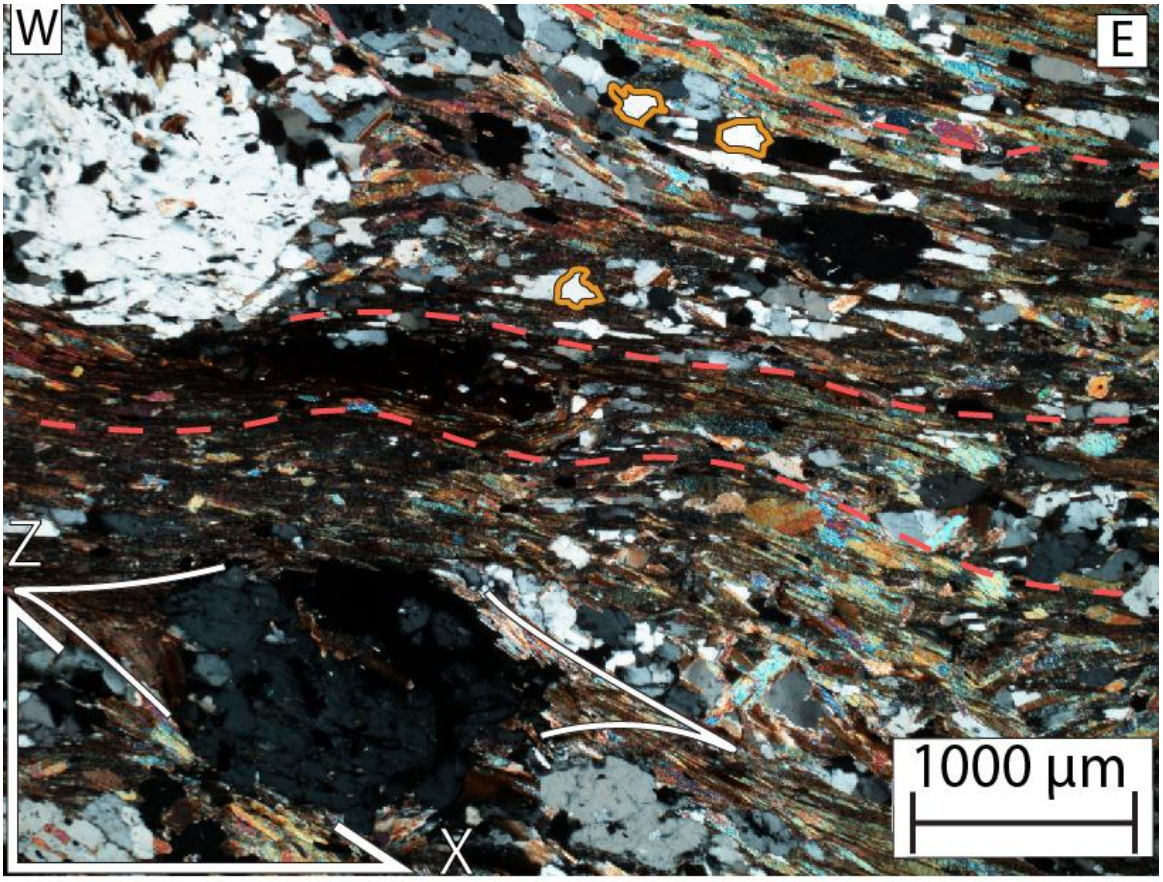

Figure 4-18: X-Z section of sample 16PR33A. The spaced foliation (S_n, red) is here defined by mica microlithons and cleavage domains. Amoeboid (orange) quartz grains can be seen, suggesting grain boundary migration. Wing like muscovite and biotite structures (white) are locally associated with albite grains.

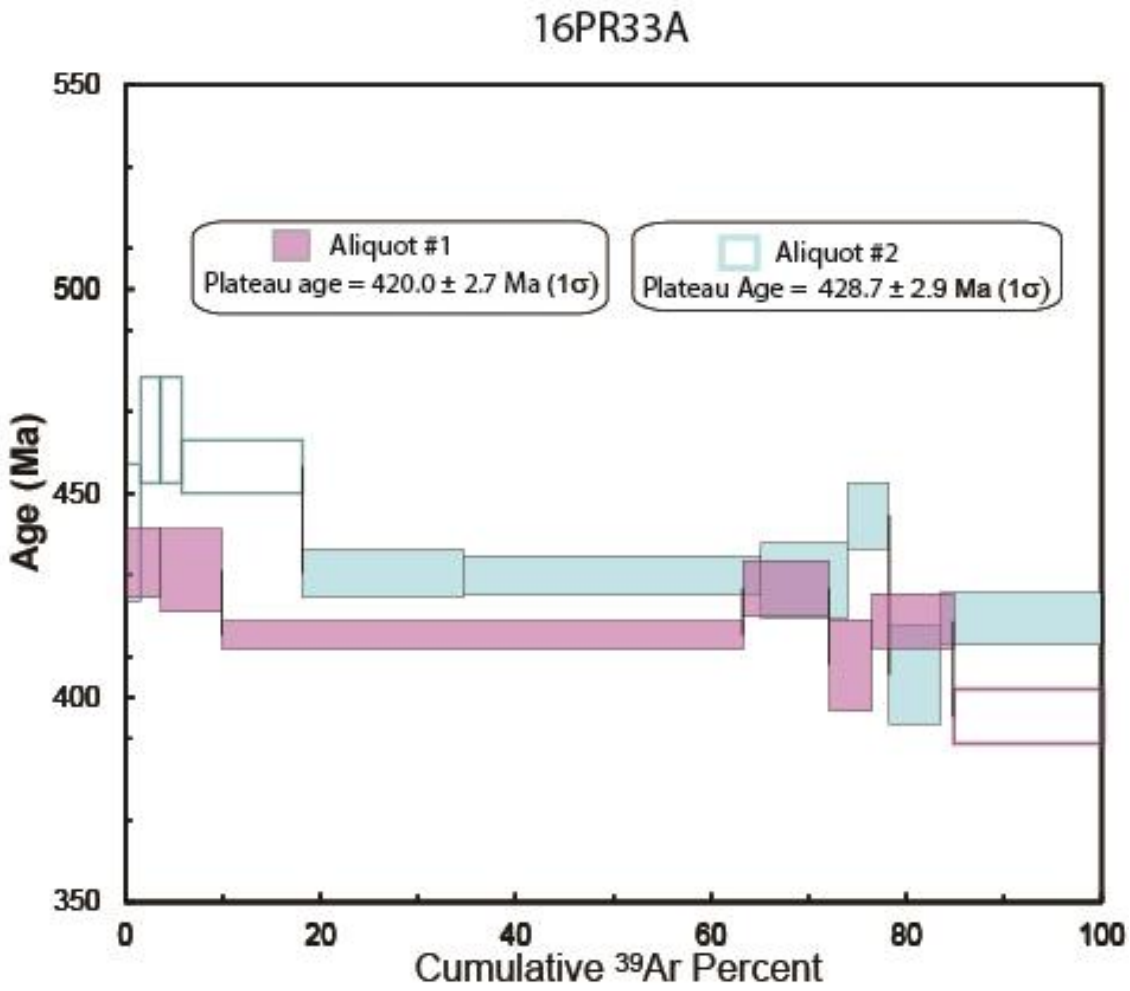

Figure 4-19: Apparent $^{40}Ar/^{39}Ar$ spectrum of muscovite from sample 16PR33A, a schist of the Hazens Notch Formation. Box heights and quoted errors are reported at the 1σ level. Shaded boxes defined reported plateau ages, and outlined boxes were excluded from plateau calculations. A single muscovite grain was analyzed per aliquot.

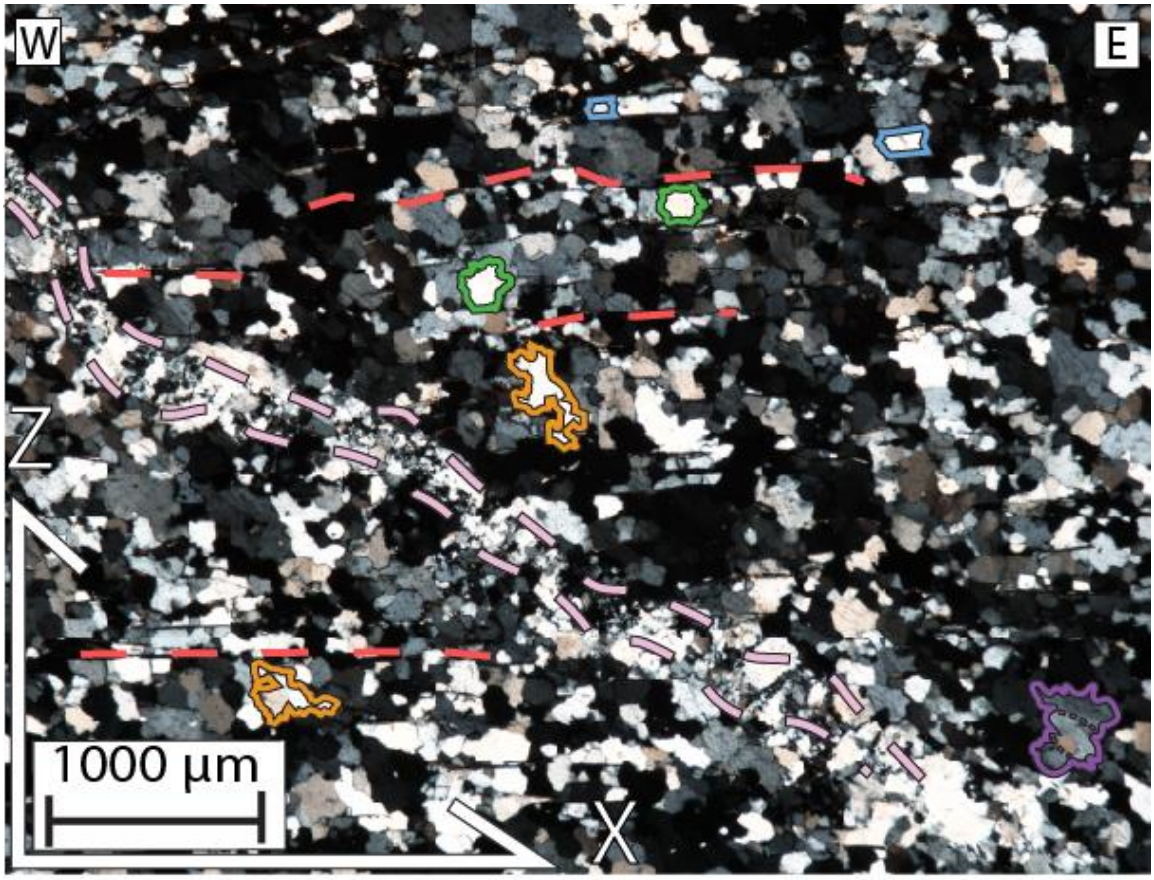

Figure 4-20 : X-Z section of sample 16PR04B. The sample is almost entirely quartz. Foliation (red) is defined by mica grains. Quartz grains (green) locally preserve microstructures that suggest bulging recrystallization was the predominant deformation mechanism, though evidence for grain boundary migration (orange), subgrain rotation (purple), and grain boundary area reduction (blue) can also be found in the sample. A quartz vein (pink) cuts across the sample diagonally.

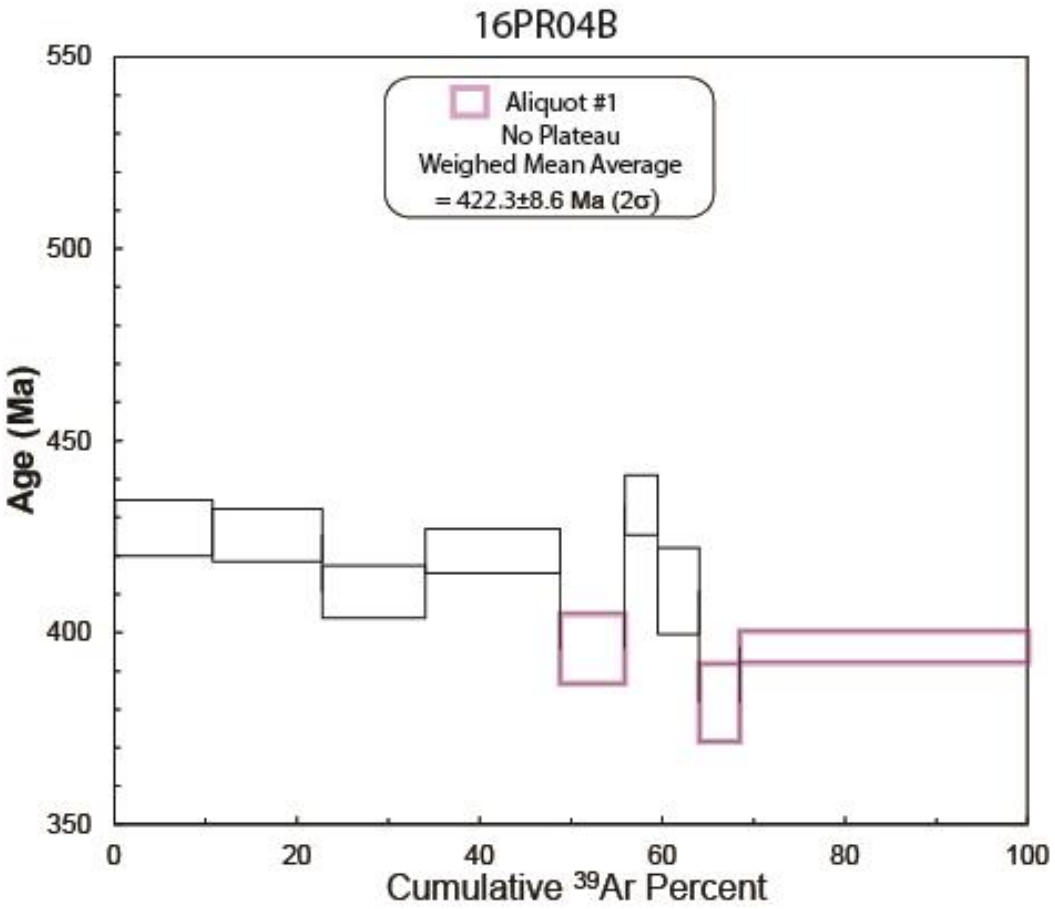

Figure 4-21: An apparent $^{40}Ar/^{39}Ar$ spectrum of muscovite from sample 16PR04B, a Hazens Notch Formation Schist. Box heights are reported at the 1σ level, and weighted mean averages (WMA) are reported at 2σ. Outlined colored boxes were excluded from plateau calculations. Black boxes define steps utilized to calculate the weighted mean average. A single muscovite grain was analyzed for this aliquot.

Chapter 5: Discussion

Microstructures from thin section and $^{40}Ar/^{39}Ar$ spectra, when analyzed spatially over the PRF footwall, can provide insight into the P-T-t-D path experienced by terranes around the TPC during exhumation. These results may aid in constraining possible exhumation models of the TPC. The following sections discusses spatially observed patterns of different microstructures, including foliation, quartz microstructures, kinematics, and their significance with regard to interpreting $^{40}Ar/^{39}Ar$ spectra.

5.1 Microstructures

5.1.1 Foliations

Foliations in this section are initially described in terms of S_n, S_{n+1}, S_{n-1}. Foliations in this field area are difficult to concretely define in terms of foliation event (i.e, S_1, S_2), as foliations are often composite. Kim et al. (2003) notes that S_1/S_2 composite foliation has been identified west of the Burgess Branch Fault Zone, and S_2/S_3 composite foliation has been identified to the east. As such, S_n in different samples may not always define the same foliation. Integration of microstructural data with $^{40}Ar/^{39}Ar$ dates to define foliations is discussed in section 5.3 below.

The dominant foliations (S_n) as they appear in thin sections from samples of the PRF footwall are predominantly spaced foliations, defined by mica microlithons and dissolution seams. S_n in some samples is defined by compositional layering of quartz, mica, and albite. Foliations younger than the dominant foliation (S_{n+1}) are found as crenulations in mica and albite porphyroblast inclusion trails. Foliations that predate- or

postdate the dominant foliation S_n are found in truncated mica domains and crenulations in mica domains. Additionally, some inclusion trails found within porphyroclastic albite do not align with S_n, suggesting that the albite captured an older foliation.

Spatial analysis of sample microstructures shows a pattern in the different foliation generations over the PRF footwall. Samples from the middle transect exhibit S_n, S_{n-1} and S_{n+1}, except for sample 16PR15A which lacks S_{n+1}. The high transect has S_{n-1} in two samples, and the other sample (16PR29A) is located on the PRF and defined by S-C' shear fabric. The southern transect exhibits S_n predominantly in samples 16PR04B and 16PR05A. Sample 16PR05A exhibits S-C' shear fabrics and is located on the PRF. Sample 16PR33A is found in the southern transect and exhibits both S_n and S_{n-1} foliations.

5.1.2 Quartz Microstructures

Quartz microstructures can be utilized for constraining the temperatures experienced during deformation (Passchier and Trouw, 2005, and references therein). Bulging (BLG) forms under low grade metamorphic conditions (300–400º C), subgrain rotation (SGR) forms under medium temperatures (400–500ºC), and grain boundary migration (GBM) forms under conditions of (500–700ºC). These temperature ranges may differ depending on stain rate, differential stress, and presence of water in the lattice or around grain boundaries (Passchier and Trouw, 2005). Grain boundary area reduction (GBAR) microstructures result from continued recovery if elevated temperatures outlast deformation. The dominant quartz microstructures have been identified for each sample in the results section above (Chapter 4).

Quartz grains in sample thin sections predominantly display either GBM or GBAR, with SGR and BLG only locally preserved. Some samples showed evidence for both medium metamorphic grade deformation structures (SGR) and high metamorphic grade structures (GBM) in similar amounts (samples 16PR08A, 16PR29A, 16PR33A). The presence of lower metamorphic grade quartz microstructures with higher grade structures may be indicative of multiple deformational events where the conditions in the second event were not intense enough to overprint structures from a prior event. Samples that exhibited GBAR as a major quartz microstructure were predominantly in the middle transect (samples 16PR16A, 16PR21A, 16PR28A, 16TP23A). Samples with GBM as the dominant quartz microstructure were more frequent in the northern and southern transects.

5.1.3 Kinematics

Kinematic indicators have been utilized in prior studies of the PRF to constrain movement history for the fault. Lamon (2001) utilized albite microstructures and shear band development to determine a top-to-the-east motion along the PRF, though later papers have questioned the application of those results for the entire PRF (Thompson and Thompson, 2003).

Only two samples from this study showed kinematic indicators in any thin sections. Samples 16PR05A and 16PR29A exhibit S-C' shear fabrics, and both are located along the mapped trace of the PRF. The sense of movement from the two samples

differ, with the northernmost sample (16PR29A) showing a top-to-the-west sense of motion, and the southernmost sample 16PR05A with a top-to-the-east sense of motion.

Differing directions of motion from the two samples could support Thompson and Thompson (2003)'s theory regarding motion along the PRF—overall westward motion with later east directed local reactivation near the Prospect Rock (close to sample 16PR05A, and Lamon (2001)'s field sites. However, two samples with a sense of motion is insufficient evidence for overall kinematic movement along the PRF, so these points only offer speculation and highlight the need for more studies along the PRF.

5.2 $^{40}Ar/^{39}Ar$ Dating

5.2.1 $^{40}Ar/^{39}Ar$ Age Plateaus and Age Spectra

Results from $^{40}Ar/^{39}Ar$ dating have also produced patterns when examined across the PRF footwall. Plateau ages of samples fall into three categories: between 458.6 ± 2.0 Ma and 447.5 ± 2.0 Ma, between 432.0 ± 2.1 Ma to 427.1 ± 2.6 Ma, and between 419.3 ± 2.4 Ma to 420.0 ± 2.7 Ma. These date brackets generally correspond with the northern, middle, and southern transects, respectively. Two samples have ages that correspond with another age bracket outside of their transect (see samples 16PR28A, 16PR33A). In the PRF footwall, older ages appear to the north, and seem to become younger moving south. Ages on the eastern side of the footwall (samples 16TP23A, 16PR28A) seem younger than other ages from the northern transect (samples 16PT29A, 16PR08A), but still fall within a similar age bracket. Samples with younger ages in this bracket (between 447.5 Ma and 451.7 Ma) are located closer to the BBFZ, which suggests that ages from these samples could have been altered by faulting associated with the BBFZ.

Apparent age spectra also follow a pattern when examined spatially. Age spectra for the northern transect were mostly flat, with most steps matching the plateaus and the age brackets for the high transect. Samples from the middle transect had a larger number of steps (both in cumulative ^{39}Ar percentage and actual number of steps) that deviated from plateaus and the middle transect age bracket. Deviant steps fluctuated from over 500 Ma to under 350 Ma. Age spectra for the southern transect were mostly consistent with the plateaus for each given graph. Two of the age spectra did not produce plateaus, and had a large range in step ages (Figure 4-16, Figure 4-21).

5.3 Integration of Microstructures and $^{40}Ar/^{39}Ar$ Ages over the PRF footwall

5.3.1 Northern Transect

Samples in the northern transect (and sample 16PR28A) have plateau dates that range from between 458.6 ± 2.0 Ma and 447.5 ± 2.0 Ma. Within this range, plateau dates can be further divided, with one set between 458.6 ± 2.0Ma and 456 ± 1.8 Ma, and another between 451.7 ± 2.0 Ma and 447.5 ± 2.0 Ma.

Samples 16PR29 and 16PR08 have older dates have dates of 457.6 ± 2.0, and 458.6 ± 2.0Ma and 456 ± 1.8 Ma respectively. These dates fall close to the age range of the Taconic Orogeny (470–460), and are from the northern section of the PRF footwall, with 16PR08 located close to the TPC. In thin section, sample 16PR08A preserves evidence for S_{n-1} in S_n microlithons, indicating that deformation forming S_n could have occurred during D_2, which has been associated with the Taconic Orogeny. 16PR29A exhibits S-C' fabrics, which suggests that movement along the PRF occurred during this period as well. GBAR does not strongly occur in these samples, but rather GBM is the

dominant quartz microstructure. This may indicate that the sample cooled during deformation or soon thereafter, and suggests limited recovery occurred after formation of the S-C' fabric. Under these conditions, micas may have capture the development of S-C' shear fabrics in sample 16PR29A during westward transport of the upper plate, which runs contrary to results regarding PRF motion from Lamon (2001).

Samples 16TP23A and 16PR28A have similar ages, with 451.7 ± 2.0 Ma and 447.5 ± 2.0 Ma, and 447.8 ± 2.1 Ma respectively. These samples are from the eastern side of the PRF footwall, and have plateau dates that are somewhat close to the Taconic Orogeny. Thin sections from both samples show evidence of an S_{n-1} foliation through mica domains and crenulations truncated by S_n. 16PR28A shows evidence of S_{n+1} through non-truncated mica crenulations. Age spectra for both samples produce plateaus, though sample 16PR28A exhibits a much larger range in step ages (between ~340 to 460 Ma). Ages from these samples could have sampled micas formed from events in the Taconic and the Salinic Orogenies, though the ages better align with the Taconic Orogeny. S_{n+1} could represent a third or fourth stage deformation. GBAR structures in both samples suggest sustained temperatures after deformation effectively ceased, which may contribute to variation in step ages.

Age spectra for samples from the northern transect are concordant with plateau dates, which suggests that plateau ages reliably date the dominant foliation. Based on the presence of both S_n and S_{n-1} in microstructures and the plateau ages that fall within the Taconic Orogeny, S_n in the northern transect aligns with S_2, and S_{n-1} with S_1 (See table 5-1).

5.3.2 Middle Transect

Samples 16PR15A, 16PR16A, and 16PR21A from the middle transect have plateau ages that fall within a similar range. Sample 16PR15 has a plateau age of 428.4 ± 2.6 Ma, sample 16PR16A has plateau ages of 431.5 ± 2.6 Ma and 427.1 ± 2.8 Ma, and sample 16PR21A has a plateau age of 432.0 ± 2.1 Ma. One plateau age from sample 16PR33A falls in a similar age range as samples from the middle transect (428.7 ± 2.9 MA).

Samples 16PR16A, 16PR21A, and PR28A exhibit three generations of foliation and similar quartz microstructures. S_{n+1} appears in thin sections as mica crenulations in all three samples, and additionally as crenulations captured in albite in sample 16PR16A. S_{n-1} appear as mica crenulations truncated by S_n in all samples, and is also found as crenulations captured as albite inclusion trail crenulations in samples 16PR15A and 16PR28A. All samples in the middle transect exhibit polygonal quartz grains, suggesting either formation during sustained higher temperatures outlasting deformation (or through grain boundary area reduction) or dissolution precipitation creep that occurred during crenulation cleavage development (cf. Ashley et al., 2013). The processes that formed these microstructures may have altered Ar concentrations in samples, resulting in a larger range in the apparent age spectra. The formation of S_{n+1} may be associated with deformation during the late Salinic Orogeny to early Acadian Orogeny, as samples in the middle transect exhibit minimum steps approaching Acadian ages. Minimum ages could represent subsequent activity post formation of the dominant foliation (S_n), such as the reactivation of the PRF, or movement along the nearby BBFZ or the Honey Hollow Fault

(Figure 2-1). S_n in the middle transect may represent a deformational period distinct from S_n in the northern transect based on plateau ages, though these ages may be altered by later processes that formed S_{n+1}. Overall, individual step heat ages for samples 16PR15A, 16PR16A, 16PR21A, and 16PR28A are varied and have steps that fall in both the range of Taconic, Salinic, and Acadian Orogenies.

Age spectra for samples from the middle transect are concordant with plateau dates, though they contain a larger number of steps that vary from plateau dates. Plateau ages reliably date the dominant foliation, but may have been influenced by subsequent deformational events. Samples exhibit 16PR16A, and 16PR21A exhibit three foliation generations, and plateau ages between 16PR15A, 16PR16A, and 16PR21A fall within a similar range (between ~427–432 Ma). Plateau ages for these samples match those of the Salinic Orogeny, suggesting that the dominant foliation in these three samples (S_n) is distinct from that of samples in the northern transect, and was formed during the Salinic. The dominant foliation for these samples thus is S_3 based on plateau ages and microstructures, with S_{n-1} and S_{n+1} aligning with S_2 and S_4 respectively. S_4 may represent deformation during phase 2 of the Salinic Orogeny, or potentially Acadian deformation, based on the range of minimum age steps from these samples (See table 5-1).

Samples 16PR28A also exhibits three foliation generations (S_n, S_{n-1}, S_{n+1}), with a single plateau age from aliquot #2 that falls within the range of the Taconic Orogeny (447.8 ± 2.1 Ma, 1σ). Aliquot #1 had a weighted mass average of 416.6 ± 8.0 Ma, with most steps falling within the Salinic Orogeny, and several steps falling within the Acadian Orogeny. Based on the variation of dates obtained from the spectra, it is difficult

to determine the structural generation for foliations. The dominant foliation (S_n) could be considered as S_2 through ages from Aliquot #1, or as S_3 with ages from aliquot #2. Likewise, interpretations of foliation generations for S_{n-1} and S_{n+1} are variable.

5.3.3 Southern Transect

Samples in the southern transect (16PR05A, 16PR33A, and 16PR04B) are located near the Lamoille River along the footwall of the PRF. Sample 16PR05A has one plateau age of 419.3 ± 2.4 Ma, and PR33A has plateau ages of 420.0 ± 2.7 Ma and 428.7 ± 2.9 Ma, which fall within the age range of the Salinic Orogeny. Step heat spectra from 16PR05 (aliquot #2) and 16PR33A (aliquot #1) show a consistent plateau near 420 Ma, with a small percentage of deviating steps. Smaller numbers of steps deviating from the plateau suggest that plateau dates are more likely aligned with formation of the dominant foliation (S_n). Mica winged albite parallel to S_n in 16PR33A also suggest that mica was formed during the dominant deformation phase and may be accurate for dating the formation of S_n. Plateau ages associated with S_n may represent Salinic deformation associated with reactivation of the PRF or activity along the nearby Honey Hollow Fault. Based on plateau ages, S_n in the southern transect may represent the same or a similar different deformational period to S_n in the middle transect, and may be distinct from S_n in the northern transect, despite the similarity in S_n structures in all samples.

Age spectra for samples from the southern transect are concordant with plateau dates, which suggests that plateau ages reliably date the dominant foliation. Plateau ages range from ~419–428, with two plateau dates closer to 420 Ma. These ages align with the Salinic Orogeny, and may date deformation simultaneous to/post-dating deformational

events associated with samples of the middle transect. The dominant foliation for these samples thus is S_3 based on plateau ages and microstructures, with S_{n-1} aligning with S_2 (See table 5-1)

Sample 16PR04B shows that there may be influence from other younger events, ranging from about 427 Ma to 380 Ma which includes dates from the Taconic up to the Acadian Orogeny. 16PR05A (aliquot #1) also has a large range in step ages, including steps (~81 Ma, ~30 Ma) that resemble pulses of exhumation noted in the neighboring White Mountains of New Hampshire, from ~65–85 Ma (Amidon et al, 2016) and ~20–0 Ma (Barr et al., 2017). These spectra may be indicative of other orogenic events that occurred after deformation associated with the formation of S_3 and S_4.

5.4 Further Tectonic Implications

Plateau ages from $^{40}Ar/^{39}Ar$ step heating demonstrate a range of ages, reaching from the Taconic to the Salinic Orogenies. These dates are correlative to ages from $^{40}Ar/^{39}Ar$ studies in the Quebec Appalachian regions of Canada. Plateau ages from the northern transect of this study both overlap with, and reach ages that are slightly younger than $^{40}Ar/^{39}Ar$ ages associated with the Taconic Orogeny in southern Quebec (Tremblay and Pinet, 2016, and references therein). Younger Taconic ages are expected south of Quebec, as along strike diachronism during deformation has been demonstrated between Quebec and New England. Plateau ages from the middle and southern transects of this study also fall within the range of ages dating phase 1 of the Salinic Orogeny in southern Quebec (Tremblay and Pinet, 2016, and references therein).

Examination of tectonic models detailing the Salinic Orogeny from southern Quebec will aid in developing a more complete geologic history in Vermont. The geology of Vermont plays a role in linking the geology of Quebec and the rest of New England, as ophiolite and accretionary wedge sequences in Vermont have been correlated between both locations (Kim et al., 2003). Further studies are needed to examine the spatial extent of the Salinic Orogeny into New England, and to correlate structures to observations noted in Quebec.

5.5 Future Work

More work is necessary to fully understand the role to fully understand the role the PRF played in the exhumation of the TPC. Results from this study have identified that ages from PRF footwall samples that correlate to the Taconic and Salinic orogenies, but more work is necessary to have a complete understanding of the PRF's geologic history.

Results from this study have used ages from $^{40}Ar/^{39}Ar$ analysis to correlate foliation generations in thin sections. Work has not been done to correlate foliations found in thin section (S_1-S_4) to foliation generations where they were observed in the field (Previously S_1 to S_3). Further examination of field structures and microstructures would aid in further matching structures to the new foliation schema. Additionally, studies have not yet found kinematic data that spans the entirety of the PRF footwall. Results from Lamon (2001) indicate top to the east movement of the PRF, but Thompson and Thompson (2003) argue that results from this study are too geographically limited, and push for a model utilizing westward motion with local fault reactivation of the PRF

towards the east. Results from this study show kinematic indicators both top to the west and east, but are insufficient to draw firm conclusions. Samples with kinematic indicators were identified as being located on the PRF. Studies utilizing more samples from along the PRF itself may lead to more kinematic indicators that further address the PRF's role in the exhumation of the TPC.

Further complicating this issue is the mapping of the PRF itself. The placement of the PRF is at certain points inferred (P. Thompson, 2018, personal communication), as the difference between the footwall and the hanging wall is determined by compositional differences (specifically by the lack or presence of albitic minerals), and the fault is difficult to identify in the field.

More research in this study area is also needed to fully understand the formation of the GMA. Past studies have associated the formation of the GMA with the Acadian Orogeny (Castonguay et al., 2011; Laird et al., 1984), but dates from this study have few steps that fall within the Acadian. Other studies examining the Acadian Orogeny in Vermont utilize $^{40}Ar/^{39}Ar$ Biotite dating (Webb et al., 2018; Lagor, 2016), whereas our samples from the PRF footwall utilized mainly muscovite. Closure temperatures between the two minerals are different as well as their stability under different conditions (P, T, D, fluid), so utilizing biotite to date rocks from the PRF footwall may aid in accurately comparing PRF footwall dates to those areas associated with the Acadian orogeny.

Examining other local faults besides the PRF may also be critical in having a full understanding of the PRF's history. The PRF is bounded on both sides by faults, the Burgess Branch Fault as a normal fault to its east, and the Honey Hollow Fault as a thrust

fault to its west. Movement along these faults could have impacted $^{40}Ar/^{39}Ar$ ages from rocks within the footwall, but the exact timing of fault movement is not yet understood for these faults either.

All aforementioned studies would be aided by further analysis of more samples from in and around the PRF. The scope of this study allowed for the examination of 45 thin sections and the dating of ten samples through $^{40}Ar/^{39}Ar$ analysis. A larger scope examination in and around the PRF footwall would no doubt aid in further constraining patterns in age and microstructures.

Table 5 - 3 : Correlating Foliations and Deformation Events

Field-defined foliations from Thompson and Thompson (2003), Thompson et al. (1999), and Kim et al. (1999)	**Deformation events from Castonguay et al. (2011)**	**$^{40}Ar/^{39}Ar$ and microstructure-defined foliations from this work**
S_0: Bedding. Appearances are rare, and often transposed,	Deformation of the Belvidere Mountain Complex: ~505–473 Ma (Pre-Taconic Deformation).	S_1: Mica defined foliations truncated by S_2. No definite dates, interpreted as earlier Taconic Orogeny.
S_1: Compositional layering, poorly preserved, often in quartzite beds. Commonly parallel to S_2. Associated with the Taconic Orogeny.	Early Deformation (D_e): ~471–460 Ma (Taconic Orogeny).	S_2: Defined quartz and mica microlithons in the northern transect, where it is the dominant foliation. Defined by mica grains truncated by S_3 in the middle and southern transects. ~458–447 Ma, interpreted as later Taconic Orogeny.
S_2: Spaced cleavage, frequently the dominant foliation over the GMA. Associated with peak metamorphism during the Taconic Orogeny.	Middle Deformation (D_m): ~446–415 Ma (Salinic Orogeny).	S_3: Defined quartz and mica microlithons in the middle and southern transects, where it is the dominant foliation. ~432–428 Ma (middle transect), and ~420–419 (southern transect). Interpreted as part of the Salinic Orogeny.
S_3: Spaced or crenulation cleavage. Average strike is 015º (AZ). Associated with the Acadian Orogeny.	Late Deformation (D_l): ~386–355 Ma (Acadian Orogeny).	S_4: Defined by crenulation cleavage deforming S_3. Features only appear in the middle transect. No definite dates, interpreted as part of either the Salinic Orogeny, or the Acadian Orogeny.

Chapter 6: Conclusions

$^{40}Ar/^{39}Ar$ plateau ages from this study have demonstrated that samples ages from the footwall of the Prospect Rock Fault range between 460–420 Ma (Figure 2-1). $^{40}Ar/^{39}Ar$ age spectra demonstrate that these ages are reliable. Plateau ages from these samples correspond to both the Taconic Orogeny (470–460 Ma) and the Salinic Orogeny (440–410 Ma, Castonguay et al., 2011; Tremblay and Pinet, 2016). $^{40}Ar/^{39}Ar$ plateau ages vary spatially over the PRF footwall, with Taconic plateau ages in the northern transect and Salinic plateau ages in the southern transect. Plateau ages did not correlate with the Acadian Orogeny (395–375 Ma), though minimum ages of age spectra from the middle transect fell within this range.

Patterns in microstructural features and in $^{40}Ar/^{39}Ar$ age spectra also correspond spatially to the PRF footwall. Based on microstructural observations and intergration with $^{40}Ar/^{39}Ar$ plateau ages, four foliation generations were identified. S_1 and S_2 were identified in samples from the northern transect, S_3 from samples from the middle and southern transect, and S_4 in the middle transect. Quartz microstructures patterns were also observed spacially, with grain boundary migration as the dominant quartz microstructure in the northern and southern transects (associated with metamorphic temperatures between 500–700ºC). Grain boundary area reduction (GBAR) appears with grain boundary migration (GBM) as the dominant quartz structures in the middle transect. GBAR may result from dissolution precipitation creep during crenulation cleavage (Ashley et al., 2013), or from sustained higher temperatures post metamorphism (Passchier and Trouw, 2005).

The range in $^{40}Ar/^{39}Ar$ spectra steps exhibited variations across the PRF footwall. Overall, steps in $^{40}Ar/^{39}Ar$ age spectra were overall concordant with plateaus. Spectra from the northern and southern transects exhibited step age range within Taconic (470–460 Ma) and Salinic Orogenies (440–410 Ma). Formation of the S_2 foliation associated with age plateaus for northern transect, and S_3 in the middle and southern transects, may be distinct based on plateau ages. Formation of S_3 in the middle and southern transects during the Salinic Orogeny could be related to deformation due to the reactivation of the PRF, or motion along the Honey Hollow Fault.

Spectra from the middle transect showed a larger variation in step age range, with steps ages ranging from the Taconic Orogeny through the Acadian Orogeny (395–375 Ma). The higher variation in ages in the middle transect could correlate with the formation of crenulations or sustained temperatures post metamorphism, both of which could have altered Ar concentrations within muscovite.

Results from the two kinematic indicators were not conclusive enough to draw substantial conclusions. However, the presence of top-to-the-west movement from S-C' shear bands stands contrary to Lamon's (2001) proposal for complete top-to-the-east movement of the PRF. More studies are necessary to verify direction of kinematic movement and draw further conclusions.

Overall, $^{40}Ar/^{39}Ar$ plateau ages from this study demonstrates that rocks from the Prospect Rock Fault footwall are more strongly associated with ages of the Taconic and Salinic Orogenies, though some samples show minimum ages that align with the Acadian Orogeny. These results align with results from Quebec that record evidence of the Salinic

Orogeny, and may aid in furthering Vermont's tectonic understanding of its geologic past.

BIBLIOGRAPHY

Agard, P., Yamato, P., Jolivet, L., & Burov, E., 2008, Discontinuous exhumation of oceanic crust: insights from blueschists and eclogites into the subduction channel, Earth Science Review, p. 10.

Andersen, T. B., Jamtveit, B., Dewey, J. F., & Swensson, E., 1991, Subduction and eduction of continental crust: major mechanisms during continent-continent collision and orogenic extensional collapse, a model based on the south Norwegian Caledonides, Terra Nova 3(3), p. 303-310.

Amidon, W. H., Roden-Tice, M., Anderson, A. J., McKeon, R. E., & Shuster, D. L., 2016, Late Cretaceous unroofing of the White Mountains, New Hampshire, USA: An episode of passive margin rejuvenation?, Geology 44 (6), p. 415-418.

Armstrong, T. R., Tracy, R. J., & Hames, W. E., 1992, Contrasting styles of Taconian, eastern Acadian and western Acadian metamorphism, central and western New England, Journal of Metamorphic Geology 10(3), 415-426.

Ashley, K. T., Webb, L. E., Spear, F. S., & Thomas, J. B., 2013, P-T-D histories from quartz: A case study of the application of the TitaniQ thermobarometer to progressive fabric development in metapelites, Geochemistry, Geophysics, Geosystems 14(9), p. 3821-3843.

Baldwin, S. L., Webb, L. E., & Monteleone, B. D., 2008, Late Miocene coesite-eclogite exhumed in the Woodlark Rift, Geology 36 (9), p. 735-738.

Barr, M., Amidon, W., "U-Pb dating of calcite veins in the Champlain Valley: constraints on post-Paleozoic rejuvenation in the eastern North American margin", the Vermont Geological Socienty Annual Spring Student Presentation Meeting, April 29, 2017, University of Vermont, Trinity Campus, Burlington, VT, Conference Presentation.

Beaumont, C., Ellis, S., & Pfiffner, A., 1999, Dynamics of sediment subduction-accretion at convergent margins: Short-term modes, long-term deformation, and tectonic implications, Journal of Geophysical Research: Solid Earth 104(B8), p. 17573-17601.

Bertrand, R., & Malo, M., 2001, Source rock analysis, thermal maturation and hydrocarbon generation in Siluro-Devonian rocks of the Gaspe Belt basin, Canada, Bulletin of Canadian Petroleum Geology 49(2), p. 238-261.

Bourque, P. A., 2001, Sea level, synsedimentary tectonics, and reefs: implications for hydrocarbon exploration in the Silurian–lowermost Devonian Gaspé Belt, Québec Appalachians, Bulletin of Canadian Petroleum Geology 49(2), p. 217-237.

Bothner, W. A., & Laird, J., 1987, Structure and metamorphism at Tillotson Peak, North-Central Vermont, Guidebook for field trips in Vermont (2), p. 383-405.

Bothner, W. A., and Laird, J., 1999, Geologic Map of the Tillotson – Haystack Area, Hazens Notch and Parts of the Lowell 7.5 Minute Quadranges, Vermont, Vermont Geological Survey.

Bradley, D. C., 2000, Migration of the Acadian orogen and foreland basin across the northern Appalachians of Maine and adjacent areas (No. 1624), US Department of the Interior, US Geological Survey.

Caby, R., 1994, Precambrian coesite from northern Mali: first record and implications for plate tectonics in the trans-Saharan segment of the Pan-African belt, European Journal of Mineralogy, p. 235-244.

Cady, W. M., Albee, A. L., & Chidester, A. H., 1963, Bedrock geology and asbestos deposits of the upper Missisquoi Valley and vicinity, Vermont (No. 1122-B), US Geological Survey.

Carswell, DA., 1990, Eclogite facies rocks, Blackie, Glasgow and London, p. 396.

Castonguay, S., Tremblay, A., Ruffet, G., Féraud, G., Pinet, N., & Sosson, M., 1997, Ordovician and Silurian metamorphic cooling ages along the Laurentian margin of the Quebec Appalachians: Bridging the gap between New England and Newfoundland, Geology 25(7), p. 583-586.

Castonguay, S., Ruffet, G., Tremblay, A., & Féraud, G., 2001, Tectonometamorphic evolution of the southern Québec Appalachians: 40Ar/39Ar evidence for Middle Ordovician crustal thickening and Silurian–Early Devonian exhumation of the internal Humber zone, Geological Society of America Bulletin 113(1), p. 144-160.

Castonguay, S., & Tremblay, A., 2003, Tectonic evolution and significance of Silurian Early Devonian hinterland-directed deformation in the internal Humber zone of the southern Quebec Appalachians, Canadian Journal of Earth Sciences 40(2), p. 255-268.

Castonguay, S., Ruffet, G., & Tremblay, A, 2007, Dating polyphase deformation across low-grade metamorphic belts: An example based on 40Ar/39Ar muscovite age constraints from the southern Quebec Appalachians, Canada, Geological Society of America Bulletin 119(7-8), p. 978-992.

Castonguay, S., Kim, J., Thompson, P. J., Gale, M. H., Joyce, N., Laird, J., & Doolan, B. L., 2012, Timing of tectonometamorphism across the Green Mountain anticlinorium,

northern Vermont Appalachians: $^{40}Ar/^{39}Ar$ data and correlations with southern Quebec, Bulletin 124(3-4), p. 352-367.

Cawood, P. A., McCausland, P. J., & Dunning, G. R., 2001, Opening Iapetus: constraints from the Laurentian margin in Newfoundland, Geological Society of America Bulletin 113(4), p. 443-453.

Cawood, P. A., & Nemchin, A. A., 2001 b, Paleogeographic development of the east Laurentian margin: Constraints from U-Pb dating of detrital zircons in the Newfoundland Appalachians, Geological Society of America Bulletin 113(9), p. 1234-1246.

Chemenda, A. I., Mattauer, M., Malavieille, J., & Bokun, A. N., 1995, A mechanism for syn-collisional rock exhumation and associated normal faulting: results from physical modelling, Earth and Planetary Science Letters 132(1-4), p. 225-232.

Chopin, C., 1984, Coesite and Pure Pyrope in High-grade Blueschists of the Western Alps: A First Record and Some Consequences, Contributions to Mineralogy and Petrology 86.2, p. 107-118.

Coish, R. A., Fleming, F. S., Larsen, M., Poyner, R., & Seibert, J., 1985, Early rift history of the proto-Atlantic Ocean; geochemical evidence from metavolcanic rocks in Vermont, American Journal of Science 285(4), p. 351-378.

Coish, R. A., Perry, D. A., Anderson, C. D., & Bailey, D., 1986, Metavolcanic rocks from the Stowe Formation, Vermont; remnants of ridge and intraplate volcanism in the Iapetus ocean, American Journal of Science 286(1), p. 1-28.

Coish, R. A., Bramley, A., Gavigan, T., & Masinter, R., 1991, Progressive changes in volcanism during lapetan rifting: Comparisons with the East African Rift-Red Sea system, Geology 19(10), p. 1021-1024.

Compagnoni, R., and Maffeo, B., 1973, Jadeite-bearing metagranite l.s. and related rocks in the Monte Mucrone Area (Siesa Lanzo zone, Western Italian Alps), Schweiz Mineral Petrog Mitt 53, p. 355-377.

Currie, C. A., Beaumont, C., & Huismans, R. S., 2007, The fate of subducted sediments: A case for backarc intrusion and underplating, Geology 35(12), p. 1111-1114.

Daczko, N. R., Caffi, P., and Mann, P., 2011, Structural Evolution of the Dayman Dome Metamorphic Core Complex, Eastern Papua New Guinea, Bulletin 123(11-12), p. 2335-2351.

De Souza, S., Tremblay, A., Ruffet, G., & Pinet, N., 2012, Ophiolite obduction in the Quebec Appalachians, Canada—$^{40}Ar/^{39}Ar$ age constraints and evidence for syn-tectonic erosion and sedimentation, Canadian journal of earth sciences 49(1), p. 91-110.

Dobrzhinetskaya, L. F, 2012, Microdiamonds — Frontier of Ultrahigh-pressure Metamorphism: A Review, Gondwana Research 21.1, p. 207-223

Duche^ne, S., Lardeaux, J. M., & Albarède, F., 1997, Exhumation of eclogites: insights from depth-time path analysis, Tectonophysics 280(1-2), p. 125-140.

Dunning, G. R., Krogh, T. E., & Pederson, R. B., 1986, U–Pb zircon ages of Appalachian–Caledonian ophiolites, Terra Cognita 6, L51.

Ernst, W. G., Maruyama, S., & Wallis, S., 1997, Buoyancy-driven, rapid exhumation of ultrahigh-pressure metamorphosed continental crust, Proceedings of the National Academy of Sciences 94(18), p. 9532-9537.

Ernst, W. G., 2006, Preservation/exhumation of ultrahigh-pressure subduction complexes, Lithos 92(3-4), p. 321-335.

Fryer, P., Wheat, C. G., & Mottl, M. J., 1999, Mariana blueschist mud volcanism: Implications for conditions within the subduction zone, Geology 27(2), p. 103-106.

Gerya, T., & Stöckhert, B., 2006, Two-dimensional numerical modeling of tectonic and metamorphic histories at active continental margins, International Journal of Earth Sciences 95(2), p. 250-274.

Gorczyk, W., Guillot, S., Gerya, T. V., & Hattori, K., 2007, Asthenospheric upwelling, oceanic slab retreat, and exhumation of UHP mantle rocks: Insights from Greater Antilles, Geophysical Research Letters 34(21).

Guillot, S., Hattori, K. H., & de Sigoyer, J., 2000, Mantle wedge serpentinization and exhumation of eclogites: insights from eastern Ladakh, northwest Himalaya, Geology 28(3), p. 199-202.

Guillot, S., Hattori, K. H., de Sigoyer, J., Nägler, T., & Auzende, A. L., 2001, Evidence of hydration of the mantle wedge and its role in the exhumation of eclogites, Earth and Planetary Science Letters 193(1-2), p. 115-127.

Guillot, S., Garzanti, E., Baratoux, D., Marquer, D., Mahéo, G., & De Sigoyer, J., 2003, Reconstructing the total shortening history of the NW Himalaya, Geochemistry, Geophysics, Geosystems, 4(7).

Guillot, S., Mahéo, G., De Sigoyer, J., Hattori, K. H., & Pecher, A., 2008, Tethyan and Indian subduction viewed from the Himalayan high-to ultrahigh-pressure metamorphic rocks, Tectonophysics 451(1-4), p. 225-241.

Guillot, S., Hattori, K., Agard, P., Schwartz, S., & Vidal, O., 2009, Exhumation processes in oceanic and continental subduction contexts: a review, Subduction zone geodynamics, Springer, Berlin, Heidelberg, pp. 175-205.

Hacker, B. R., Ratschbacher, L., Webb, L., Mcwilliams, M. O., Ireland, T., Calvert, A., Dong, S., Wenk, H., and Chateigner, D., 2000, Exhumation of Ultrahigh-pressure Continental Crust in East Central China: Late Triassic-Early Jurassic Tectonic Unroofing, Journal of Geophysical Research: Solid Earth 105.B6, p. 13339-13364.

Hacker, B. R., & Gerya, T. V., 2013a, Paradigms, new and old, for ultrahigh-pressure tectonism, Tectonophysics 603, p. 79-88.

Hacker, B. R., Gerya, T. V., and Gilotti, J. A., 2013b, Formation and Exhumation of Ultrahigh-Pressure Terranes, Elements 9.4, p. 289-93.

Hames, W. E., & Hodges, K. V., 1993, Laser $^{40}Ar/^{39}Ar$ evaluation of slow cooling and episodic loss of ^{40}Ar from a sample of polymetamorphic muscovite, Science 261(5129), p. 1721-1723.

Hattori, K. H., & Guillot, S., 2007, Geochemical character of serpentinites associated with high-to ultrahigh-pressure metamorphic rocks in the Alps, Cuba, and the Himalayas: Recycling of elements in subduction zones, Geochemistry, Geophysics, Geosystems 8(9).

Haüy, R. J., 1822, Traité de minéralogie 2nd éd, Bachelier et Huzard, Paris.

Hepburn, J. C., Trask, N. J., Rosenfeld, J. L., & Thompson Jr, J. B., 1984, Bedrock geology of the Brattleboro quadrangle, Vermont-New Hampshire, Vermont Agency of Environmental Conservation.

Hesse, R., & Dalton, E., 1991, Diagenetic and low-grade metamorphic terranes of Gaspé Peninsula related to the geological structure of the Taconian and Acadian orogenic belts, Quebec Appalachians. Journal of Metamorphic Geology, 9(6), p. 775-790.

Hibbard, J., 1994, Kinematics of Acadian deformation in the northern and Newfoundland Appalachians, The Journal of Geology 102(2), p. 215-228.

Hilairet, N., Reynard, B., Wang, Y., Daniel, I., Merkel, S., Nishiyama, N., & Petitgirard, S., 2007, High-pressure creep of serpentine, interseismic deformation, and initiation of subduction, Science 318(5858), p. 1910-1913.

Honsberger, I. W., 2015, Metamorphism, Deformation, Geochemistry, and Tectonics of Exhumed Ultramafic and Mafic Rocks in the Central and North-Central Vermont Appalacians, Doctoral Dissertation, University of New Hampshire.

Jahn, B. M., Caby, R., & Monie, P., 2001, The oldest UHP eclogites of the world: age of UHP metamorphism, nature of protoliths and tectonic implications, Chemical Geology 178(1-4), p. 143-158.

Jicha, B. R., & Brown, F. H., 2014, An age for the Korath Range, Ethiopia and the viability of $^{40}Ar/^{39}Ar$ dating of kaersutite in Late Pleistocene volcanics, Quaternary Geochronology 21, p. 53-57.

Julien, P. S., & Hubert, C., 1975, Evolution of the Taconian orogen in the Quebec Appalachians, American Journal of Science 275, p. 337-362.

Karabinos, P., 1998, Tectonic and stratigraphic development of the Connecticut Valley Trough in the New England Appalachians., In Geological Society of America Abstracts with Programs Vol. 30 No. 7, p. 191.

Karabinos, P., Samson, S. D., Hepburn, J. C., & Stoll, H. M., 1998, Taconian orogeny in the New England Appalachians: collision between Laurentia and the Shelburne Falls arc, Geology 26(3), p. 215-218.

Kim, J., Gale, M., Laird, J., Stanley, R., & Wright, S. F., 1999, Lamoille River valley bedrock transect # 2. In Guidebook to field trips in Vermont and adjacent regions of New Hampshire and New York: New England Intercollegiate Geological Conference Vol. 91, pp. 213-250.

Kim, J., Coish, R., Evans, M., & Dick, G., 2003, Supra–subduction zone extensional magmatism in Vermont and adjacent Quebec: Implications for early Paleozoic Appalachian tectonics, Geological Society of America Bulletin 115(12), p. 1552-1569.

Laird, J., and Albee, A. L., 1981, High-pressure Metamorphism in Mafic Schist from Northern Vermont, American Journal of Science 281.2 p. 97-126.

Laird, J., Lanphere, M. A., and Albee, A. L., 1984, Distribution of Ordovician and Devonian Metamorphism in Mafic and Pelitic Schists from Northern Vermont, American Journal of Science 284.4-5, p. 376-413.

Laird, J., Trzcienski, W. E., Bothner, W. A., Cheney, J. T., & Hepburn, J. C., 1993, High-pressure, Taconian, and subsequent polymetamorphism of southern Quebec and northern Vermont. in Field Trip Guidebook for the Northeastern United States: 1993 Boston GSA, v. 2, p 1-32. In 1993 Geological Society of America Annual Meeng and 85th Annual New England Intercollegiate Geological Conference Meeting, Boston, MA.

Lagor, S. W., 2016, The relationship between magmatism and deformation during the Acadian orogeny: A case study from eastern-central Vermont, Doctoral dissertation, University of Vermont.

Lamon, T. C., 2001, Tectonic Wedging in the Northern Vermont Appalachians: an Emplacement Model for the Albitic Core Rocks of the Green Mountain Anticlinorium, Masters Dissertation, University of Vermont.

Lee, J. Y., Marti, K., Severinghaus, J. P., Kawamura, K., Yoo, H. S., Lee, J. B., & Kim, J. S., 2006, A redetermination of the isotopic abundances of atmospheric Ar, Ceochimica et Cosmochimica Acta v. 70, p. 4507–4512.

Liou, J. G., Tsujimori, T., Zhang, R. Y., Katayama, I., & Maruyama, S., 2004, Global UHP metamorphism and continental subduction/collision: the Himalayan model, International Geology Review 46, p. 1-27.

Little, T. A., Baldwin, S. L., Fitzgerald, P. G., and Monteleone, B., 2007, Continental Rifting and Metamorphic Core Complex Formation Ahead of the Woodlark Spreading Ridge, D'Entrecasteaux Islands, Papua New Guinea, Tectonics 26.1.

Ludwig, K.R., 2003., Isoplot/EX, rev. 3.00, a Geochronological Toolkit for Microsoft Excel: Berkeley Geochronology Center Special Publication v. 4, 71 pp.

Malo, M., Ruffet, G., Pincivy, A., & Tremblay, A., 2008, A $^{40}Ar/^{39}Ar$ study of oceanic and continental deformation processes during an oblique collision: Taconian orogeny in the Quebec reentrant of the Canadian Appalachians, Tectonics 27(4).

Mazzotti, S., & Hyndman, R. D, 2002, Yakutat collision and strain transfer across the northern Canadian Cordillera, Geology 30(6), p. 495-498.

McDougall, I., & Harrison, T. M., 1999, Geochronology and Thermochronology by the $^{40}Ar/^{39}Ar$ Method, Oxford University Press on Demand.

McLelland, J. M., Selleck, B. W., Bickford, M. E., Tollo, R. P., Bartholomew, M. J., Hibbard, J. P., & Karabinos, P. M., 2010, Review of the Proterozoic evolution of the Grenville Province, its Adirondack outlier, and the Mesoproterozoic inliers of the Appalachians, From Rodinia to Pangea: The Lithotectonic Record of the Appalachian Region: Geological Society of America Memoir 206, p. 21-49.

McWilliams, C. K., Walsh, G. J., & Wintsch, R. P., 2010, Silurian-Devonian age and tectonic setting of the Connecticut Valley-Gaspe trough in Vermont based on U-Pb SHRIMP analyses of detrital zircons, American Journal of Science 310(5), p. 325-363.

Monteleone, B. D., Baldwin, S. L., Webb, L. E., Fitzgerald, P. G., Grove, M., & Schmitt, A. K., 2007, Late Miocene–Pliocene eclogite facies metamorphism, D'Entrecasteaux Islands, SE Papua New Guinea, Journal of Metamorphic Geology 25(2), p. 245-265.

Moore, D. E., & Lockner, D. A., 2007, Comparative deformation behavior of minerals in serpentinized ultramafic rock: Application to the slab-mantle interface in subduction zones, International Geology Review 49(5), p. 401-415.

Naylor, R. S., 1976, Isotopic dating and New England stratigraphy, Contributions to the stratigraphy of New England: Geological Society of America Memoir 148, p. 419-425.

Negredo, A. M., Replumaz, A., Villaseñor, A., & Guillot, S., 2007, Modeling the evolution of continental subduction processes in the Pamir–Hindu Kush region, Earth and Planetary Science Letters 259(1-2), p. 212-225.

Oldow, J. S., Bally, A. W., & Avé Lallemant, H. G., 1990, Transpression, orogenic float, and lithospheric balance, Geology 18(10), p. 991-994.

Passchier, C. W., & Trouw, R. A., 2005, Microtectonics (Vol. 1), Springer Science & Business Media.

Perrot, M., 2014, Étude structurale et microstructurale de la faille St-Joseph et de la ligne Baie Verte-Brompton dans les Appalaches du sud du Québec.

Pinet, N., Castonguay, S., & Tremblay, A., 1996, Thrusting and back thrusting in the Taconian internal zone, southern Quebec Appalachians, Canadian Journal of Earth Sciences 33(9), p. 1283-1293.

Pinet, N., 2013, Gaspé Belt subsurface geometry in the northern Québec Appalachians as revealed by an integrated geophysical and geological study: 2—Seismic interpretation and potential field modelling results, Tectonophysics 588, p. 100-117.

Pincivy, A., Malo, M., Ruffet, G., Tremblay, A., & Sacks, P. E., 2003, Regional metamorphism of the Appalachian Humber zone of Gaspé Peninsula: $^{40}Ar/^{39}Ar$ evidence for crustal thickening during the Taconian orogeny, Canadian Journal of Earth Sciences 40(2), p. 301-315.

Rankin, D. W., Coish, R. A., Tucker, R. D., Peng, Z. X., Wilson, S. A., & Rouff, A. A., 2007, Silurian extension in the Upper Connecticut Valley, United States and the origin of middle Paleozoic basins in the Quebec embayment, American Journal of Science 307(1), p. 216-264.

Ratcliffe, N. M., Aleinikoff, J. N., Burton, W. C., & Karabinos, P., 1991, Trondhjemitic, 1.35–1.31 Ga gneisses of the Mount Holly Complex of Vermont: evidence for an

Elzevirian event in the Grenville basement of the United States Appalachians, Canadian Journal of Earth Sciences 28(1), p. 77-93.

Renne, P. R., Swisher, C. C., Deino, A. L., Karner, D. B., Owens, T. L., & DePaolo, D. J., 1998, Intercalibration of standards, absolute ages and uncertainties in $^{40}Ar/^{39}Ar$ dating, Chemical Geology, v. 145, p. 117–152

Renne, P. R., Deino, A. L., Hilgen, F. J., Kuiper, K. F., Mark, D. F., Mitchell, W. S., Morgan, L. E., Mundil, R., and Smit, J., 2013, Time scales of critical events around the Cretaceous-Paleogene boundary, Science 339 (6120), p. 684-687.

Reynard, B., Hilairet, N., Balan, E., & Lazzeri, M., 2007, Elasticity of serpentines and extensive serpentinization in subduction zones, Geophysical Research Letters 34(13).

Rodgers, J., 1968, The eastern edge of the North American continent during the Cambrian and Early Ordovician, Studies of Appalachian geology: northern and maritime, p. 141-149.

Rubatto, D., & Hermann, J., 2001, Exhumation as fast as subduction?, Geology 29(1), p. 3-6.

Sasseville, C., Tremblay, A., Clauer, N., & Liewig, N., 2008, K–Ar age constraints on the evolution of polydeformed fold–thrust belts: The case of the Northern Appalachians (southern Quebec), Journal of Geodynamics 45(2-3), p. 99-119.

Schmidt, M. W., & Poli, S., 1998, Experimentally based water budgets for dehydrating slabs and consequences for arc magma generation, Earth and Planetary Science Letters 163(1-4), p. 361-379.

Simonetti, A., & Doig, R., 1990, U–Pb and Rb–Sr geochronology of Acadian plutonism in the Dunnage zone of the southeastern Quebec Appalachians, Canadian Journal of Earth Sciences 27(7), p. 881-892.

Sizova, E., Gerya, T., & Brown, M., 2012, Exhumation mechanisms of melt-bearing ultrahigh pressure crustal rocks during collision of spontaneously moving plates, Journal of Metamorphic Geology 30(9), p. 927-955.

Slack, J. F., 1994, Geochemical constraints on the evolution of the Connecticut Valley Trough, east-central Vermont, In Geological Society of America Abstracts with Programs Vol. 26, p. 73.

Slack, J. F., Offield, T. W., Woodruff, L. G., & Shanks III, W. C., 2001, Geology and geochemistry of Besshi-type massive sulfide deposits of the Vermont copper belt. Part II. Environmental Geochemistry and Mining History of Massive Sulfide Deposits in the

Vermont Copper Belt: Society of Economic Geologists Guidebook Series, 35, p. 193-211.

Smith, D. C., 1984, Coesite in clinopyroxene in the Caledonides and its implications for geodynamics, Nature 310, p. 641.

Steiger, R. H., & Jäger, E., 1977, Subcommission on geochronology: convention on the use of decay constants in geo- and cosmochronology: Earth and Planetary Science Letters v. 36, p. 359–362.

Stoenner, R. W., Schaeffer, O. A., & Katcoff, S., 1965, Half-lives of argon-37, argon-39, and argon-42, Science 148(3675), p. 1325-1328.

Stanley, R. S., and Ratcliffe, N. M., 1985, Tectonic Synthesis of the Taconian Orogeny in Western New England, Geological Society of America Bulletin 96(10), 1227-1250.

Stöckhert, B., & Renner, J., 1998, Rheology of crustal rocks at ultrahigh pressure. *In* When continents collide: geodynamics and geochemistry of ultrahigh-pressure rocks (pp. 57-95). Springer, Dordrecht.

Sutter, J. F., Ratcliffe, N. M., & Mukasa, S. B., 1985, $^{40}Ar/^{39}Ar$ and K-Ar data bearing on the metamorphic and tectonic history of western New England, Geological Society of America Bulletin 96(1), p. 123-136.

Tremblay, A., & Pinet, N., 2005, Diachronous supracrustal extension in an intraplate setting and the origin of the Connecticut Valley–Gaspé and Merrimack troughs, northern Appalachians, Geological magazine 142(1), p. 7-22.

Tremblay, A., & Pinet, N., 2016, Late Neoproterozoic to Permian tectonic evolution of the Quebec Appalachians, Canada, Earth-science reviews 160, p. 131-170.

Tremblay, A., Ruffet, G., & Castonguay, S., 2000, Acadian metamorphism in the Dunnage zone of southern Quebec, northern Appalachians: $^{40}Ar/^{39}Ar$ evidence for collision diachronism, Geological Society of America Bulletin 112(1), p. 136-146.

Tremblay, A., Ruffet, G., & Bédard, J. H., 2011, Obduction of Tethyan-type ophiolites—A case-study from the Thetford-Mines ophiolitic Complex, Quebec Appalachians, Canada, Lithos 125(1-2), p. 10-26.

Thompson, P.J., and Thompson, T.B., 1998, Digital bedrock geologic map of the Johnson quadrangle, Vermont. Vermont Geological Survey Open-File Report VG 98-2A, scale 1:24000.

Thompson, P. J., Thompson, T. B., Doolan, B. L., & Wright, S. F., 1999, Lithotectonic packages and tectonic boundaries across the Lamoille River transect in northern

Vermont. In Guidebook to Field Trips in Vermont and adjacent regions of New Hampshire and New York: New England Intercollegiate Geological Conference Vol. 91, pp. 51-94.

Thompson, P. J., and Thompson, T. B., 2003, The Prospect Rock Thrust: Western Limit of the Taconian Accretionary Prism in the Northern Green Mountain Anticlinorium, Vermont, Canadian Journal of Earth Sciences 40(2), p. 269-284.

Tsujimori, T., Sisson, V. B., Liou, J. G., Harlow, G. E., & Sorensen, S. S., 2006, Very-low-temperature record of the subduction process: A review of worldwide lawsonite eclogites, Lithos 92(3-4), p. 609-624.

Ueda, H., Usuki, T., & Kuramoto, Y., 2004, Intraoceanic unroofing of eclogite facies rocks in the Omachi Seamount, Izu-Bonin frontal arc, Geology 32(10), p. 849-852.

Ulmer, P., & Trommsdorff, V., 1995, Serpentine stability to mantle depths and subduction-related magmatism, Science 268(5212), p. 858-861.
van Staal, C. R., Barr, S. M., & Percival, J. A., 2012, Lithospheric architecture and tectonic evolution of the Canadian Appalachians and associated Atlantic margin, Tectonic styles in Canada: the LITHOPROBE perspective, Edited by JA Percival, FA Cook, and RM Clowes, Geological Association of Canada Special Paper, 49.

Van der Pluijm, B. A., & Marshak, S., 2004. Earth structure: An introduction to structural geology and tectonics. WW Norton and Company. Inc, New York.

van Staal, C. R., & De Roo, J. A., 1995, Mid-Paleozoic tectonic evolution of the Appalachian Central Mobile Belt in northern New Brunswick, Canada: collision, extensional collapse and dextral transpression, Current perspectives in the Appalachian–Caledonian Orogen, Edited by JP Hibbard, CR van Staal, and PA Cawood, Geological Association of Canada, Special Paper, 41, p. 367-389.

van Staal, C. R., Whalen, J. B., McNicoll, V. J., Pehrsson, S., Lissenberg, C. J., Zagorevski, A., & Jenner, G. A, 2007, The Notre Dame arc and the Taconic orogeny in Newfoundland, Geological Society of America Memoirs 200, p. 511-552.

van Staal, C. R., Whalen, J. B., Valverde-Vaquero, P., Zagorevski, A., & Rogers, N, 2009, Pre-Carboniferous, episodic accretion-related, orogenesis along the Laurentian margin of the northern Appalachians, Geological Society, London, Special Publications 327(1), p. 271-316.

Webb, L. E., Baldwin, S. L., Little, T. A., & Fitzgerald, P. G., 2008, Can microplate rotation drive subduction inversion?, Geology 36(10), p. 823-826.

Webb, L. W., Klepeis, K. A., Kim, J. J., New Insights on Acadian Deformation and Reactivation in Northern Vermont from Integrated Structural and Geochronological Studies, *In* North East Geological Society of America, March 18-20, Burlington, VT.

West, D. P., Ludman, A., & Lux, D. R., 1992, Silurian age for the Pocomoonshine Gabbro-Diorite, southeastern Maine and its regional tectonic implications, American Journal of Science 292(4), p. 253-273.

Whalen, J. B., Mortensen, J. K., & Roddick, J. C., 1991, Implications of U–Pb and K–Ar geochronology for petrogenesis and cooling history of the McGerrigle Mountains plutonic complex, Gaspé, Quebec, Canadian Journal of Earth Sciences 28(5), p. 754-761.

Whitehead, J., Reynolds, P. H., & Spray, J. G., 1996, $^{40}Ar/^{39}Ar$ age constraints on Taconian and Acadian events in the Quebec Appalachians, Geology 24(4), p. 359-362.

Whitehead, J., Dunning, G. R., & Spray, J. G., 2000, U-Pb geochronology and origin of granitoid rocks in the Thetford Mines ophiolite, Canadian Appalachians, Geological Society of America Bulletin 112(6), p. 915-928.

Williams, H., Colman-Sadd, S. P., & Swinden, H. S., 1988, Tectonic-stratigraphic subdivisions of central Newfoundland, Current Research, Part B, Geological Survey of Canada, Paper 88, p. 91-98.

Yamato, P., Agard, P., Burov, E., Le Pourhiet, L., Jolivet, L., & Tiberi, C., 2007, Burial and exhumation in a subduction wedge: Mutual constraints from thermomechanical modeling and natural P-T-t data (Schistes Lustrés, western Alps), Journal of Geophysical Research: Solid Earth, 112(B7).

Yin, A., Manning, C. E., Lovera, O., Menold, C. A., Chen, X., & Gehrels, G. E., 2007, Early Paleozoic tectonic and thermomechanical evolution of ultrahigh-pressure (UHP) metamorphic rocks in the northern Tibetan Plateau, northwest China, International Geology Review 49(8), p. 681-716.

Appendix A: $^{40}Ar/^{39}Ar$ Analytical Results

Table 1/01. $^{40}Ar/^{39}Ar$ analytical results for sample 16PR04B aliquot #1, muscovite (n=1 xtl; J=3.73978E-03± 0.24%)

Laser Wattage	Dwell Time	$^{37}Ar/^{39}Ar$	$^{37}Ar/^{39}Ar$ Error	$^{36}Ar/^{39}Ar$	$^{36}Ar/^{39}Ar$ Error	^{39}Ar (cps)	^{39}Ar (cps) Error	Cumulative % ^{39}Ar Released	% $^{40}Ar^*$	$^{39}Ar/^{40}Ar$	$^{39}Ar/^{40}Ar$ Error	Age (Ma)	1σ% Error (Ma)
4.0W	1	0.45508	0.05976	0.00545	0.00123	573.9	9.4	1.07080E+01	97.73	0.01393	0.00023	427.25	1.85
4.05W	1	0.30260	0.04856	0.00465	0.00105	643.2	10.0	2.27103E+01	98.05	0.01404	0.00022	425.35	1.77
4.075W	1	0.52786	0.05697	0.00583	0.00116	604.7	9.7	3.39929E+01	97.47	0.01452	0.00024	410.62	1.83
4.1W	1	0.20604	0.04329	0.00310	0.00088	788.5	10.4	4.87064E+01	98.68	0.01428	0.00019	421.28	1.59
4.125W	1	0.68202	0.09466	0.00777	0.00172	381.5	8.3	5.58254E+01	96.52	0.01499	0.00033	395.78	2.31
4.15W	1	1.26110	0.17842	0.01188	0.00344	192.4	3.2	5.94157E+01	95.25	0.01338	0.00023	433.27	1.92
4.2W	1	0.90661	0.14177	0.00820	0.00260	244.0	6.4	6.39684E+01	96.48	0.01438	0.00038	410.84	2.67
4.5W	1	0.83913	0.15276	0.01438	0.00301	235.8	5.8	6.83685E+01	93.51	0.01512	0.00038	381.77	2.65
Fuse	1	0.15110	0.02208	0.01168	0.00048	1695.2	15.2	1.00000E+02	94.87	0.01470	0.00014	396.18	1.42

Table 1/02. $^{40}Ar/^{39}Ar$ analytical results for sample 16PR05A aliquot #1, muscovite (n=1 xtl; 3.74033E-03 ± 0.24%)

Laser Wattage	Dwell Time	$^{37}Ar/^{39}Ar$	$^{37}Ar/^{39}Ar$ Error	$^{36}Ar/^{39}Ar$	$^{36}Ar/^{39}Ar$ Error	^{39}Ar (cps)	^{39}Ar (cps) Error	Cumulative % ^{39}Ar Released	% $^{40}Ar^*$	$^{39}Ar/^{40}Ar$	$^{39}Ar/^{40}Ar$ Error	Age (Ma)	1σ% Error (Ma)
3.8W	1	1.49604	0.36294	0.02927	0.00989	70.5	1.5	9.55E-01	32.85	0.07684	0.00623	29.94	24.00
3.9W	1	0.09641	0.08094	0.00414	0.00221	315.2	8.5	5.23E+00	80.09	0.16120	0.00717	33.79	5.67
4.0W	1	0.09690	0.31612	0.01781	0.00838	80.7	2.0	6.32E+00	69.41	0.05752	0.00335	80.95	8.36
4.1W	1	0.19035	0.13106	0.00458	0.00378	186.1	3.0	8.84E+00	97.27	0.01998	0.00036	306.59	2.00
4.2W	1	0.04473	0.00727	0.00372	0.00024	3211.8	22.1	5.24E+01	98.35	0.01486	0.00011	405.12	1.23
4.225W	1	0.11859	0.03425	0.00196	0.00092	780.7	8.9	6.29E+01	99.00	0.01720	0.00020	357.28	1.50
4.3W	1	0.08465	0.08519	0.00468	0.00224	286.6	5.0	6.68E+01	95.62	0.03137	0.00061	197.82	2.24
4.5W	1	0.01797	0.10707	0.00343	0.00268	263.2	5.1	7.04E+01	97.45	0.02496	0.00050	249.73	2.21
4.9W	1	0.00464	0.02653	0.00195	0.00071	1019.9	13.5	8.42E+01	98.38	0.02773	0.00038	228.27	1.69
5.5W	1	0.00919	0.05250	0.00075	0.00138	515.6	8.4	9.12E+01	98.95	0.04661	0.00081	139.98	2.02
fuse	1	0.00728	0.04160	0.00183	0.00117	650.8	8.9	1.00E+02	99.04	0.01746	0.00025	352.42	1.67

Table 1/03. $^{40}Ar/^{39}Ar$ analytical results for sample 16PR05A aliquot #2, muscovite (n=1 xtl; J= 3.74033E-03 ± 0.24%)

Laser Wattage	Dwell Time	$^{37}Ar/^{39}Ar$	$^{37}Ar/^{39}Ar$ Error	$^{36}Ar/^{39}Ar$	$^{36}Ar/^{39}Ar$ Error	^{39}Ar (cps)	^{39}Ar (cps) Error	Cumulative % ^{39}Ar Released	% ^{40}Ar*	$^{39}Ar/^{40}Ar$	$^{39}Ar/^{40}Ar$ Error	Age (Ma)	1σ% Error (Ma)
4.0W	1	1.00695	0.37146	0.12552	0.00811	93.8	1.2	1.74486E+00	69.54	0.00813	0.00011	509.51	2.23
4.05W	1	0.41368	0.37058	0.01189	0.00772	89.6	1.9	3.41015E+00	95.52	0.01263	0.00031	456.75	2.51
4.1W	1	0.63562	0.10960	0.00606	0.00227	304.4	5.3	9.07121E+00	97.39	0.01441	0.00026	413.20	1.95
4.15W	1	0.40491	0.05910	0.00027	0.00114	593.4	8.6	2.01047E+01	99.88	0.01443	0.00021	422.06	1.66
4.175W	1	0.14004	0.02285	0.00092	0.00042	1531.0	16.9	4.85740E+01	99.60	0.01466	0.00016	414.94	1.44
4.2W	1	0.15849	0.02265	0.00130	0.00045	1545.2	16.0	7.73078E+01	99.43	0.01470	0.00015	413.26	1.40
4.225W	1	0.78103	0.14150	0.00503	0.00253	261.8	6.6	8.21764E+01	97.82	0.01454	0.00037	411.83	2.55
4.25W	1	1.46664	0.23142	0.00134	0.00445	152.0	2.7	8.50027E+01	99.45	0.01380	0.00026	438.27	1.94
4.5W	1	1.27072	0.30531	0.00713	0.00625	109.3	2.1	8.70354E+01	97.11	0.01355	0.00027	436.03	2.11
Fuse	1	0.37381	0.05039	0.00729	0.00100	697.2	8.7	1.00000E+02	96.96	0.01396	0.00018	423.23	1.57

Table 1/04. $^{40}Ar/^{39}Ar$ analytical results for sample 16PR08A aliquot #1, muscovite (n=1 xtl 3.74089E-03 ± 0.23%)

Laser Wattage	Dwell Time	$^{37}Ar/^{39}Ar$	$^{37}Ar/^{39}Ar$ Error	$^{36}Ar/^{39}Ar$	$^{36}Ar/^{39}Ar$ Error	^{39}Ar (cps)	^{39}Ar (cps) Error	Cumulative % ^{39}Ar Released	% ^{40}Ar*	$^{39}Ar/^{40}Ar$	$^{39}Ar/^{40}Ar$ Error	Age (Ma)	1σ% Error (Ma)
4.0W	1	0.49526	0.17185	0.02112	0.00397	165.7	2.7	1.54599E+00	92.45	0.01198	0.00021	464.97	1.98
4.05W	1	0.35724	0.24393	0.02864	0.00623	106.7	2.0	2.54138E+00	89.95	0.01176	0.00024	461.30	2.32
4.075W	1	0.03771	0.31321	0.02741	0.00837	83.1	2.0	3.31653E+00	90.13	0.01206	0.00031	451.73	2.74
4.1W	1	0.12001	0.20699	0.00149	0.00570	114.9	2.3	4.38807E+00	99.43	0.01288	0.00028	464.75	2.15
4.125W	1	0.10802	0.15447	0.01104	0.00412	176.4	4.3	6.03351E+00	95.81	0.01272	0.00032	454.70	2.53
4.15W	1	0.09013	0.06644	0.00266	0.00185	374.8	7.1	9.52999E+00	99.00	0.01264	0.00024	470.91	1.98
4.175W	1	0.10686	0.02823	0.00295	0.00079	896.9	12.4	1.78973E+01	98.86	0.01293	0.00018	460.93	1.62
4.2W	1	0.12751	0.02027	0.00228	0.00057	1251.7	15.7	2.95744E+01	99.11	0.01305	0.00017	458.27	1.52
4.225W	1	0.09304	0.01339	0.00235	0.00037	1981.0	15.6	4.80559E+01	99.10	0.01282	0.00010	465.31	1.25
4.25W	1	0.08974	0.01390	0.00260	0.00041	1824.6	18.2	6.50776E+01	98.97	0.01326	0.00013	450.98	1.36
4.275W	1	0.11810	0.02304	0.00260	0.00060	1204.7	11.8	7.63168E+01	98.99	0.01302	0.00013	458.69	1.35
4.325W	1	0.20897	0.03683	0.00442	0.00100	722.1	10.3	8.30538E+01	98.26	0.01317	0.00019	451.17	1.66
4.5W	1	0.61765	0.10401	0.00521	0.00171	415.7	7.3	8.69323E+01	97.96	0.01312	0.00023	451.70	1.91
fuse	1	0.08820	0.01896	0.00303	0.00052	1400.7	13.9	1.00000E+02	98.82	0.01308	0.00013	456.15	1.36

Table 1/05. $^{40}Ar/^{39}Ar$ analytical results for sample 16PR08A aliquot #2, muscovite (n=1 xtl; J= 3.74089E-03 ± 0.23%)

Laser Wattage	Dwell Time (Min)	$^{37}Ar/^{39}Ar$	$^{37}Ar/^{39}Ar$ Error	$^{36}Ar/^{39}Ar$	$^{36}Ar/^{39}Ar$ Error	^{39}Ar (cps)	^{39}Ar (cps) Error	Cumulative % ^{39}Ar Released	% $^{40}Ar^*$	$^{39}Ar/^{40}Ar$	$^{39}Ar/^{40}Ar$ Error	Age (Ma)	1σ% Error (Ma)
4.0W	1	0.43429	0.05690	0.02159	0.00134	592.1	9.3	3.76378E+00	92.07	0.01231	0.00019	452.35	1.87
4.025W	1	0.40915	0.04470	0.01038	0.00091	833.7	11.4	9.06301E+00	96.06	0.01270	0.00018	456.63	1.65
4.05W	1	0.39435	0.03921	0.01186	0.00084	950.4	11.5	1.51041E+01	95.61	0.01241	0.00015	464.35	1.56
4.075W	1	0.23742	0.02668	0.00301	0.00054	1324.7	12.9	2.35245E+01	98.84	0.01290	0.00013	461.72	1.35
4.1W	1	0.16756	0.01442	0.00229	0.00030	2454.6	18.2	3.91264E+01	99.11	0.01303	0.00010	458.86	1.23
4.125W	1	0.21117	0.01472	0.00213	0.00028	2538.0	21.9	5.52587E+01	99.16	0.01332	0.00012	450.32	1.29
4.15W	1	0.26301	0.02063	0.00270	0.00041	1809.4	16.3	6.67597E+01	98.95	0.01304	0.00012	457.99	1.32
4.175W	1	0.44484	0.03747	0.00582	0.00074	999.3	11.6	7.31113E+01	97.74	0.01301	0.00015	454.17	1.49
4.2W	1	0.70554	0.06308	0.00640	0.00123	567.0	8.2	7.67155E+01	97.58	0.01266	0.00019	464.54	1.68
4.5W	1	0.63965	0.05631	0.00788	0.00104	669.1	10.2	8.09683E+01	96.94	0.01300	0.00020	451.31	1.75
Fuse	1	0.15338	0.01244	0.00349	0.00025	2994.2	20.0	1.00000E+02	98.64	0.01310	0.00009	454.69	1.20

Table 1/06. 40Ar/39Ar analytical results for sample 16PR15A aliquot #1, muscovite (n=1 xtl; J= 3.75313E-03 ± 0.23%)

Laser Wattage	Dwell Time (Min)	$^{37}Ar/^{39}Ar$	$^{37}Ar/^{39}Ar$ Error	$^{36}Ar/^{39}Ar$	$^{36}Ar/^{39}Ar$ Error	^{39}Ar (cps)	^{39}Ar (cps) Error	Cumulative % ^{39}Ar Released	% $^{40}Ar^*$	$^{39}Ar/^{40}Ar$	$^{39}Ar/^{40}Ar$ Error	Age (Ma)	1σ% Error (Ma)
4.0W	1	0.30753	0.18648	0.01947	0.00520	142.5	2.7	1.27780E+00	92.81	0.01238	0.00024	454.53	2.17
4.1W	1	0.18347	0.43988	0.01623	0.01200	60.4	0.9	1.81939E+00	94.69	0.01095	0.00020	514.98	2.01
4.15W	1	0.15780	0.12072	0.00461	0.00326	220.2	5.7	3.79446E+00	98.07	0.01403	0.00037	426.98	2.60
4.175W	1	0.34371	0.08075	0.01614	0.00204	351.4	8.6	6.94640E+00	93.61	0.01326	0.00033	430.69	2.59
4.2W	1	0.20098	0.04383	0.00566	0.00127	589.8	8.8	1.22364E+01	97.72	0.01348	0.00020	441.08	1.72
4.225W	1	0.15741	0.02528	0.00312	0.00067	1072.4	15.5	2.18558E+01	98.71	0.01387	0.00020	433.70	1.68
4.25W	1	0.06755	0.01105	0.00209	0.00032	2337.9	18.9	4.28267E+01	99.14	0.01388	0.00012	435.21	1.27
4.275W	1	0.14883	0.02451	0.00436	0.00064	1155.5	11.7	5.31910E+01	98.24	0.01350	0.00014	442.32	1.39
4.8W	1	0.44957	0.10712	0.01668	0.00320	253.4	5.6	5.54638E+01	93.61	0.01283	0.00029	443.77	2.39
fuse	1	0.03066	0.00521	0.00227	0.00017	4965.1	28.8	1.00000E+02	99.03	0.01427	0.00009	424.07	1.17

Table 1/07. $^{40}Ar/^{39}Ar$ analytical results for sample 16PR15A aliquot #2, muscovite (n=1 xtl; J= 3.75313E-03± 0.23%)

Laser Wattage	Dwell Time (Min)	$^{37}Ar/^{39}Ar$	$^{37}Ar/^{39}Ar$ Error	$^{36}Ar/^{39}Ar$	$^{36}Ar/^{39}Ar$ Error	^{39}Ar (cps)	^{39}Ar (cps) Error	Cumulative % ^{39}Ar Released	% ^{40}Ar*	$^{39}Ar/^{40}Ar$	$^{39}Ar/^{40}Ar$ Error	Age (Ma)	1σ% Error (Ma)
4.0W	1	1.81130	0.77520	0.03508	0.01243	52.3	1.5	7.76099E-01	84.97	0.01435	0.00049	368.88	3.85
4.1W	1	2.34799	0.80903	0.00293	0.01196	54.2	1.4	1.57967E+00	98.69	0.01499	0.00046	406.17	2.99
4.15W	1	0.17980	0.41716	0.00315	0.00667	97.2	2.1	3.02077E+00	98.62	0.01472	0.00035	411.07	2.39
4.175W	1	0.85263	0.12786	0.00420	0.00227	270.1	6.3	7.02642E+00	98.20	0.01433	0.00034	419.84	2.38
4.2W	1	0.29326	0.04083	0.00246	0.00071	927.0	11.5	2.07744E+01	98.96	0.01418	0.00018	426.27	1.53
4.225W	1	0.16718	0.01837	0.00177	0.00031	2059.7	17.6	5.13205E+01	99.26	0.01406	0.00012	430.68	1.29
4.25W	1	0.32802	0.03566	0.00323	0.00066	1012.5	11.6	6.63365E+01	98.65	0.01394	0.00016	431.80	1.47
4.275W	1	1.20089	0.14493	0.00590	0.00263	239.2	4.9	6.98835E+01	97.57	0.01381	0.00029	431.62	2.18
4.8W	1	1.46915	0.12524	0.00944	0.00213	295.3	5.9	7.42635E+01	95.84	0.01475	0.00030	400.90	2.19
fuse	1	0.24430	0.02086	0.00410	0.00034	1735.4	17.1	1.00000E+02	98.21	0.01463	0.00015	411.82	1.39

Table 1/08. $^{40}Ar/^{39}Ar$ analytical results for sample 16PR16A aliquot #1, muscovite (n=1 xtl; J= 3.75313E-03± 0.23%)

Laser Wattage	Dwell Time (Min)	$^{37}Ar/^{39}Ar$	$^{37}Ar/^{39}Ar$ Error	$^{36}Ar/^{39}Ar$	$^{36}Ar/^{39}Ar$ Error	^{39}Ar (cps)	^{39}Ar (cps) Error	Cumulative % ^{39}Ar Released	% ^{40}Ar*	$^{39}Ar/^{40}Ar$	$^{39}Ar/^{40}Ar$ Error	Age (Ma)	1σ% Error (Ma)
4.0W	1	0.12608	0.23978	0.03788	0.00688	112.9	2.2	2.17511E+00	87.35	0.01118	0.00023	471.52	2.40
4.1W	1	0.16765	0.31885	0.02416	0.00839	84.9	2.2	3.81143E+00	90.76	0.01281	0.00035	432.61	2.92
4.15W	1	0.13479	0.24497	0.00060	0.00687	105.7	2.2	5.84729E+00	99.77	0.01291	0.00029	467.17	2.21
4.175W	1	0.38253	0.18202	0.00042	0.00482	148.9	2.3	8.71682E+00	99.83	0.01328	0.00022	455.92	1.79
4.2W	1	0.08114	0.07271	0.00539	0.00201	372.8	6.8	1.59001E+01	97.87	0.01321	0.00024	449.86	1.96
4.225W	1	0.26400	0.03536	0.00297	0.00095	782.3	10.4	3.09712E+01	98.79	0.01361	0.00018	441.92	1.59
4.25W	1	0.12766	0.02075	0.00245	0.00057	1330.9	16.7	5.66115E+01	98.96	0.01420	0.00018	426.21	1.54
4.275W	1	0.31994	0.04528	0.00379	0.00128	584.0	8.0	6.78619E+01	98.42	0.01393	0.00019	431.51	1.63
4.5W	1	0.49326	0.06995	0.00061	0.00170	414.6	6.6	7.58503E+01	99.75	0.01396	0.00023	435.88	1.77
4.9W	1	1.01576	0.20047	0.01026	0.00536	138.0	2.5	7.85096E+01	95.72	0.01398	0.00027	420.04	2.09
fuse	1	0.20543	0.02372	0.00157	0.00069	1115.5	11.7	1.00000E+02	99.34	0.01408	0.00015	430.89	1.40

Table 1/09. $^{40}Ar/^{39}Ar$ analytical results for sample 16PR16A aliquot #2, muscovite (n=1 xtl; J= 3.75682E-03 ± 0.23%)

Laser Wattage	Dwell Time (Min)	$^{37}Ar/^{39}Ar$	$^{37}Ar/^{39}Ar$ Error	$^{36}Ar/^{39}Ar$	$^{36}Ar/^{39}Ar$ Error	^{39}Ar (cps)	^{39}Ar (cps) Error	Cumulative % ^{39}Ar Released	% ^{40}Ar*	$^{39}Ar/^{40}Ar$	$^{39}Ar/^{40}Ar$ Error	Age (Ma)	1σ% Error (Ma)
4.0W	1	0.32758	1.39658	0.07687	0.02111	30.6	1.2	4.83571E-01	73.77	0.01143	0.00049	398.17	5.43
4.1W	1	0.53592	0.17721	0.01241	0.00310	233.0	4.7	4.15991E+00	95.22	0.01290	0.00027	448.64	2.19
4.15W	1	0.07252	0.01306	0.00167	0.00022	3284.0	27.6	5.59781E+01	99.29	0.01424	0.00012	426.19	1.29
4.175W	1	0.14978	0.02946	0.00250	0.00048	1455.9	14.0	7.89503E+01	98.94	0.01417	0.00014	426.96	1.36
4.2W	1	2.08217	0.46769	0.04238	0.00529	137.8	3.6	8.11245E+01	83.93	0.01270	0.00035	407.90	3.14
4.35W	1	0.44263	0.22167	0.01433	0.00365	193.6	4.8	8.41794E+01	93.91	0.01423	0.00036	406.12	2.64
4.7W	1	1.83495	0.31664	0.02203	0.00502	136.1	2.4	8.63273E+01	90.75	0.01407	0.00026	398.84	2.15
Fuse	1	0.10749	0.04952	0.00467	0.00079	866.5	11.4	1.00000E+02	98.01	0.01425	0.00019	421.10	1.61

Table 1/10. $^{40}Ar/^{39}Ar$ analytical results for sample 16PR21A aliquot #1, muscovite (n=1 xtl; J= 3.79383E-03± 0.26%)

Laser Wattage	Dwell Time (Min)	$^{37}Ar/^{39}Ar$	$^{37}Ar/^{39}Ar$ Error	$^{36}Ar/^{39}Ar$	$^{36}Ar/^{39}Ar$ Error	^{39}Ar (cps)	^{39}Ar (cps) Error	Cumulative % ^{39}Ar Released	% ^{40}Ar*	$^{39}Ar/^{40}Ar$	$^{39}Ar/^{40}Ar$ Error	Age (Ma)	1σ% Error (Ma)
4.1W	1	0.00249	0.00866	0.00538	0.00024	3462.5	23.4	2.33145E+01	97.75	0.01398	0.00010	430.89	1.23
4.125W	1	0.00422	0.00962	0.00064	0.00024	2990.6	22.6	4.34518E+01	99.73	0.01428	0.00011	430.46	1.24
4.15W	1	0.04763	0.01552	0.00127	0.00040	1855.1	14.5	5.59433E+01	99.47	0.01404	0.00011	435.98	1.26
4.25W	1	0.04272	0.02082	0.00077	0.00051	1442.3	15.9	6.56553E+01	99.67	0.01428	0.00016	430.22	1.43
4.5W	1	0.04189	0.02073	0.00193	0.00057	1332.9	12.9	7.46305E+01	99.14	0.01492	0.00015	411.88	1.37
5.0W	1	0.01184	0.03785	0.00127	0.00100	730.1	8.9	7.95466E+01	99.43	0.01500	0.00019	410.89	1.52
fuse	1	0.00285	0.00910	0.00262	0.00026	3037.6	22.7	1.00000E+02	98.89	0.01418	0.00011	429.97	1.24

Table 1/11. $^{40}Ar/^{39}Ar$ analytical results for sample 16PR21A aliquot #2, muscovite (n=1 xtl; J= 3.79383E-03 ± 0.26%)

Laser Wattage	Dwell Time (Min)	$^{37}Ar/^{39}Ar$	$^{37}Ar/^{39}Ar$ Error	$^{36}Ar/^{39}Ar$	$^{36}Ar/^{39}Ar$ Error	^{39}Ar (cps)	^{39}Ar (cps) Error	Cumulative % ^{39}Ar Released	% ^{40}Ar*	$^{39}Ar/^{40}Ar$	$^{39}Ar/^{40}Ar$ Error	Age (Ma)	1σ% Error (Ma)
4.0W	1	0.16386	0.26783	0.04657	0.00458	149.8	2.4	1.28086E+00	83.19	0.01209	0.00020	425.12	2.17
4.025W	1	13.77675	3.28686	0.01436	0.02948	20.3	0.6	1.45414E+00	94.58	0.01264	0.00040	467.80	3.10
4.075W	1	3.18209	1.74412	0.03242	0.02678	23.1	1.1	1.65180E+00	88.02	0.01237	0.00063	439.99	5.23
4.1W	1	0.77995	0.14132	0.00709	0.00232	286.2	6.0	4.09909E+00	97.08	0.01377	0.00029	434.75	2.20
4.125W	1	0.21214	0.04551	0.00765	0.00086	834.9	10.4	1.12396E+01	96.89	0.01361	0.00017	438.10	1.57
4.15W	1	0.15596	0.02754	0.00234	0.00042	1463.3	18.8	2.37546E+01	99.00	0.01431	0.00019	427.06	1.56
4.175W	1	0.16248	0.02371	0.00298	0.00042	1700.2	17.1	3.82953E+01	98.71	0.01450	0.00015	420.98	1.39
4.2W	1	0.18438	0.03599	0.00628	0.00059	1118.7	10.8	4.78626E+01	97.40	0.01385	0.00014	433.28	1.38
4.225W	1	0.31284	0.06882	0.00683	0.00113	585.8	8.4	5.28728E+01	97.15	0.01398	0.00020	428.81	1.70
4.25W	1	0.54934	0.07959	0.00525	0.00123	508.0	7.0	5.72176E+01	97.77	0.01420	0.00020	425.50	1.66
4.5W	1	0.30040	0.02923	0.00269	0.00047	1385.4	13.9	6.90659E+01	98.82	0.01469	0.00015	416.74	1.39
4.8W	1	0.41627	0.05748	0.00514	0.00097	703.8	9.3	7.50851E+01	97.59	0.01571	0.00021	387.89	1.63
Fuse	1	0.10499	0.01444	0.00191	0.00024	2913.2	22.5	1.00000E+02	99.17	0.01454	0.00012	421.62	1.25

Table 1/12. $^{40}Ar/^{39}Ar$ analytical results for sample 16PR28A aliquot #1, muscovite (n=1 xtl; J= 3.81825E-03± 0.24%)

Laser Wattage	Dwell Time (Min)	$^{37}Ar/^{39}Ar$	$^{37}Ar/^{39}Ar$ Error	$^{36}Ar/^{39}Ar$	$^{36}Ar/^{39}Ar$ Error	^{39}Ar (cps)	^{39}Ar (cps) Error	Cumulative % ^{39}Ar Released	% ^{40}Ar*	$^{39}Ar/^{40}Ar$	$^{39}Ar/^{40}Ar$ Error	Age (Ma)	1σ% Error (Ma)
4.0W	1	0.11657	0.26344	0.00111	0.00604	100.0	2.0	1.31014E+00	99.47	0.01605	0.00044	389.21	2.67
4.1W	1	0.29047	0.20333	0.00484	0.00511	129.6	2.5	3.00878E+00	97.84	0.01493	0.00034	409.38	2.35
4.15W	1	0.02852	0.29878	0.00125	0.00751	88.2	1.6	4.16467E+00	99.36	0.01716	0.00049	365.93	2.82
4.2W	1	0.03122	0.26018	0.01130	0.00618	101.3	3.6	5.49253E+00	94.04	0.01766	0.00073	339.15	4.17
4.225W	1	1.12423	0.31543	0.00132	0.00790	83.8	1.7	6.59124E+00	99.36	0.01627	0.00049	384.80	2.94
4.25W	1	0.65257	0.21503	0.00118	0.00527	122.9	2.6	8.20220E+00	99.43	0.01609	0.00041	388.47	2.54
4.275W	1	0.38111	0.28394	0.00113	0.00654	97.8	2.1	9.48412E+00	99.40	0.01766	0.00053	356.93	2.95
4.3W	1	0.57434	0.25025	0.00105	0.00592	105.6	2.3	1.08680E+01	99.50	0.01604	0.00044	389.82	2.70
4.325W	1	0.50826	0.19395	0.00114	0.00405	150.7	2.6	1.28431E+01	99.47	0.01553	0.00032	401.17	2.15
4.35W	1	0.11684	0.02879	0.00852	0.00087	918.6	11.5	2.48813E+01	96.18	0.01502	0.00019	400.86	1.60
4.375W	1	0.09746	0.21091	0.00084	0.00480	131.8	2.4	2.66085E+01	99.62	0.01505	0.00034	412.74	2.26
4.4W	1	0.00802	0.00931	0.00370	0.00026	2919.7	22.5	6.48703E+01	98.37	0.01478	0.00012	414.86	1.27
4.425W	1	0.43952	0.34078	0.01078	0.00908	76.0	1.9	6.58659E+01	95.59	0.01369	0.00039	433.18	2.84
4.45W	1	0.09066	0.35405	0.00232	0.00768	84.8	2.1	6.69771E+01	99.00	0.01436	0.00039	428.04	2.67
4.475W	1	0.05458	0.35675	0.01140	0.00797	80.2	1.7	6.80277E+01	95.36	0.01362	0.00032	434.13	2.43
4.5W	1	0.46598	0.37163	0.01247	0.00960	73.3	1.8	6.89884E+01	94.90	0.01371	0.00038	429.94	2.82
4.525W	1	0.19209	0.32975	0.00960	0.00835	86.8	1.9	7.01258E+01	95.80	0.01465	0.00036	408.39	2.53
4.625W	1	0.21133	0.17410	0.00092	0.00487	148.9	2.5	7.20771E+01	99.62	0.01399	0.00025	440.68	1.88
4.725W	1	0.02315	0.13763	0.00462	0.00359	198.0	3.0	7.46721E+01	98.04	0.01422	0.00023	428.09	1.79
4.825W	1	0.53284	0.19758	0.00407	0.00313	224.6	4.3	7.76155E+01	98.16	0.01511	0.00030	406.34	2.07
4.925W	1	0.02129	0.13243	0.00444	0.00338	205.9	5.6	8.03142E+01	97.84	0.01627	0.00045	378.70	2.76
5.025W	1	0.01703	0.10596	0.00355	0.00273	257.5	6.0	8.36881E+01	98.25	0.01650	0.00039	375.31	2.41
5.125W	1	0.37834	0.10871	0.00154	0.00256	277.8	6.1	8.73280E+01	99.26	0.01620	0.00036	385.39	2.29
5.225W	1	0.38615	0.08562	0.00113	0.00213	320.0	6.0	9.15217E+01	99.48	0.01554	0.00030	400.73	2.03
Fuse	1	0.24308	0.04680	0.00465	0.00109	647.0	12.2	1.00000E+02	97.74	0.01633	0.00031	377.19	2.06

Table 1/13. $^{40}Ar/^{39}Ar$ analytical results for sample 16PR28A aliquot #2, muscovite (n=2 xtl; J= 3.81825E-03± 0.24%)

Laser Wattage	Dwell Time (Min)	$^{37}Ar/^{39}Ar$	$^{37}Ar/^{39}Ar$ Error	$^{36}Ar/^{39}Ar$	$^{36}Ar/^{39}Ar$ Error	^{39}Ar (cps)	^{39}Ar (cps) Error	Cumulative % ^{39}Ar Released	% $^{40}Ar^*$	$^{39}Ar/^{40}Ar$	$^{39}Ar/^{40}Ar$ Error	Age (Ma)	1σ% Error (Ma)
4.0W	1	0.84332	0.27458	0.00995	0.00341	164.0	2.9	1.83478E+00	95.83	0.01404	0.00026	424.81	2.03
4.05W	1	1.12834	0.20743	0.01281	0.00324	210.1	6.4	4.18553E+00	95.10	0.01281	0.00039	458.07	3.04
4.1W	1	0.52245	0.06238	0.00234	0.00100	693.9	9.5	1.19511E+01	99.07	0.01332	0.00019	458.19	1.61
4.125W	1	0.49426	0.06079	0.00025	0.00135	815.8	11.4	2.10808E+01	99.89	0.01396	0.00020	442.78	1.62
4.15W	1	0.44812	0.11288	0.00094	0.00167	382.4	7.0	2.53601E+01	99.63	0.01320	0.00025	464.33	1.94
4.175W	1	0.12168	0.03424	0.00250	0.00043	1397.5	13.0	4.09989E+01	98.97	0.01372	0.00013	445.69	1.33
4.2W	1	0.42792	0.08048	0.00374	0.00100	596.9	10.2	4.76787E+01	98.47	0.01370	0.00024	444.51	1.87
4.225W	1	0.42063	0.19857	0.00908	0.00245	241.2	5.2	5.03781E+01	96.26	0.01381	0.00030	432.70	2.29
4.25W	1	0.67181	0.39261	0.01495	0.00490	122.0	2.3	5.17431E+01	94.24	0.01291	0.00025	451.07	2.14
4.5W	1	0.15459	0.03237	0.00270	0.00040	1609.3	15.1	6.97523E+01	98.91	0.01351	0.00013	451.64	1.34
4.7W	1	0.29278	0.06285	0.00921	0.00087	763.5	10.0	7.82969E+01	96.37	0.01321	0.00018	450.54	1.62
Fuse	1	0.09166	0.02472	0.00406	0.00033	1939.3	16.5	1.00000E+02	98.33	0.01376	0.00012	442.08	1.30

Table 1/14. $^{40}Ar/^{39}Ar$ analytical results for sample 16PR29A aliquot #1, muscovite (n=1 xtl; J= 3.84067E-03± 0.21%)

Laser Wattage	Dwell Time (Min)	$^{37}Ar/^{39}Ar$	$^{37}Ar/^{39}Ar$ Error	$^{36}Ar/^{39}Ar$	$^{36}Ar/^{39}Ar$ Error	^{39}Ar (cps)	^{39}Ar (cps) Error	Cumulative % ^{39}Ar Released	% $^{40}Ar^*$	$^{39}Ar/^{40}Ar$	$^{39}Ar/^{40}Ar$ Error	Age (Ma)	1σ% Error (Ma)
4	1	0.57583	0.18782	0.05230	0.00490	148.1	2.7	9.57489E-01	82.00	0.01153	0.00022	442.81	2.37
4.1	1	0.15367	0.05836	0.00566	0.00146	501.0	10.2	4.19720E+00	97.81	0.01296	0.00027	466.24	2.12
4.2	1	0.08100	0.01053	0.00560	0.00027	2780.6	19.6	2.21777E+01	97.77	0.01334	0.00010	454.43	1.22
4.05	1	0.35263	0.20002	0.00866	0.00472	146.0	2.4	2.31216E+01	96.86	0.01212	0.00021	490.48	1.87
4.15	1	0.26788	0.03800	0.00350	0.00090	772.5	10.4	2.81166E+01	98.59	0.01348	0.00019	453.68	1.60
4.25	1	0.07504	0.01592	0.00206	0.00033	1839.0	16.3	4.00084E+01	99.17	0.01346	0.00012	456.61	1.30
4.75	1	0.01685	0.02902	0.00073	0.00058	1050.9	19.0	4.68037E+01	99.71	0.01307	0.00024	470.60	1.91
4.125	1	0.23744	0.05956	0.00246	0.00134	491.4	7.8	4.99810E+01	99.02	0.01334	0.00022	459.69	1.76
4.175	1	0.11106	0.01418	0.00213	0.00031	2066.1	16.7	6.33413E+01	99.14	0.01352	0.00011	454.71	1.26
4.225	1	0.07847	0.00826	0.00182	0.00020	3550.8	23.6	8.63020E+01	99.27	0.01339	0.00009	459.14	1.19
Fuse	1	0.00752	0.01376	0.00620	0.00036	2118.3	24.9	1.00000E+02	97.55	0.01321	0.00016	457.30	1.51

Table 1/15. $^{40}Ar/^{39}Ar$ analytical results for sample 16PR29A aliquot #2, muscovite (n=1 xtl; J= 3.84067E-03 ± 0.21%)

Laser Wattage	Dwell Time (Min)	$^{37}Ar/^{39}Ar$	$^{37}Ar/^{39}Ar$ Error	$^{36}Ar/^{39}Ar$	$^{36}Ar/^{39}Ar$ Error	^{39}Ar (cps)	^{39}Ar (cps) Error	Cumulative % ^{39}Ar Released	% ^{40}Ar*	$^{39}Ar/^{40}Ar$	$^{39}Ar/^{40}Ar$ Error	Age (Ma)	1σ% Error (Ma)
4.0W	1	0.58801	0.15284	0.01994	0.00235	291.5	5.6	1.39021E+00	92.44	0.01271	0.00025	451.83	2.17
4.05W	1	0.66918	0.13157	0.01294	0.00218	314.0	8.8	2.88791E+00	95.23	0.01235	0.00035	475.56	2.81
4.1W	1	0.43002	0.06509	0.00565	0.00105	657.2	7.4	6.02228E+00	97.88	0.01258	0.00015	479.43	1.46
4.125W	1	0.32497	0.06431	0.00208	0.00094	665.2	9.7	9.19496E+00	99.14	0.01384	0.00020	445.49	1.67
4.15W	1	0.24615	0.03335	0.00191	0.00053	1231.9	13.7	1.50707E+01	99.26	0.01294	0.00015	473.15	1.43
4.175W	1	0.16501	0.01875	0.00157	0.00031	2284.1	18.8	2.59646E+01	99.37	0.01345	0.00011	457.61	1.26
4.2W	1	0.11255	0.01417	0.00134	0.00025	2780.6	22.3	3.92268E+01	99.45	0.01381	0.00012	447.28	1.26
4.225W	1	0.11265	0.01555	0.00187	0.00023	2868.6	20.6	5.29084E+01	99.23	0.01378	0.00010	447.48	1.22
4.25W	1	0.11831	0.01724	0.00204	0.00031	2383.0	20.8	6.42743E+01	99.16	0.01380	0.00012	446.57	1.29
4.275W	1	0.36954	0.04242	0.00246	0.00067	1056.0	11.6	6.93110E+01	99.00	0.01354	0.00015	453.59	1.43
4.3W	1	0.44392	0.06091	0.00393	0.00106	677.8	9.8	7.25437E+01	98.40	0.01364	0.00020	448.45	1.67
4.5W	1	0.39187	0.05258	0.00145	0.00079	818.5	11.4	7.64477E+01	99.40	0.01389	0.00020	445.24	1.62
Fuse	1	0.08091	0.00833	0.00190	0.00014	4938.1	29.6	1.00000E+02	99.19	0.01435	0.00009	431.45	1.17

Table 1/16. $^{40}Ar/^{39}Ar$ analytical results for sample 16PR33A aliquot #1, muscovite (n=1 xtl; J= 3.87917E-03 ± 0.20%)

Laser Wattage	Dwell Time (Min)	$^{37}Ar/^{39}Ar$	$^{37}Ar/^{39}Ar$ Error	$^{36}Ar/^{39}Ar$	$^{36}Ar/^{39}Ar$ Error	^{39}Ar (cps)	^{39}Ar (cps) Error	Cumulative % ^{39}Ar Released	% ^{40}Ar*	$^{39}Ar/^{40}Ar$	$^{39}Ar/^{40}Ar$ Error	Age (Ma)	1σ% Error (Ma)
4.0W	1	1.07302	0.19486	0.02359	0.00383	159.8	2.7	3.56445E+00	90.70	0.01321	0.00024	433.50	2.08
4.05W	1	0.50634	0.11051	0.00573	0.00219	282.2	6.4	9.85821E+00	97.56	0.01426	0.00033	431.65	2.34
4.1W	1	0.09318	0.01302	0.00324	0.00028	2388.0	19.0	6.31104E+01	98.55	0.01500	0.00012	415.84	1.27
4.125W	1	0.54715	0.07556	0.00441	0.00142	396.8	6.2	7.19592E+01	98.09	0.01450	0.00023	427.24	1.77
4.425W	1	0.75557	0.16107	0.01038	0.00311	194.2	5.0	7.62897E+01	95.40	0.01484	0.00039	408.51	2.67
5.0W	1	0.66850	0.08031	0.00423	0.00169	374.3	5.8	8.46372E+01	98.13	0.01482	0.00023	419.21	1.76
Fuse	1	0.30373	0.04729	0.00483	0.00096	688.9	11.3	1.00000E+02	97.73	0.01572	0.00026	395.90	1.84

Table 1/17. $^{40}Ar/^{39}Ar$ analytical results for sample 16PR33A aliquot #2, muscovite (n=1 xtl; J= 3.87917E-03 ± 0.20%)

Laser Wattage	Dwell Time (Min)	$^{37}Ar/^{39}Ar$	$^{37}Ar/^{39}Ar$ Error	$^{36}Ar/^{39}Ar$	$^{36}Ar/^{39}Ar$ Error	^{39}Ar (cps)	^{39}Ar (cps) Error	Cumulative % ^{39}Ar Released	% ^{40}Ar*	$^{39}Ar/^{40}Ar$	$^{39}Ar/^{40}Ar$ Error	Age (Ma)	1σ% Error (Ma)
4.0W	1	0.43458	0.71242	0.04814	0.01158	56.2	1.6	1.45618E+00	82.97	0.01185	0.00037	440.71	3.58
4.05W	1	0.29618	0.46208	0.01287	0.00750	82.6	2.0	3.59413E+00	95.10	0.01275	0.00034	465.74	2.66
4.1W	1	0.29627	0.46221	0.01287	0.00750	82.6	2.0	5.73207E+00	95.10	0.01275	0.00034	465.74	2.66
4.15W	1	0.16059	0.08447	0.00533	0.00133	475.0	6.6	1.80326E+01	97.87	0.01341	0.00019	456.70	1.65
4.175W	1	0.07524	0.05691	0.00369	0.00109	638.3	8.3	3.45635E+01	98.41	0.01441	0.00019	430.67	1.58
4.2W	1	0.13485	0.03255	0.00314	0.00055	1174.6	12.7	6.49822E+01	98.65	0.01446	0.00016	430.25	1.43
4.225W	1	0.10842	0.10621	0.00500	0.00187	342.2	7.1	7.38452E+01	97.85	0.01440	0.00030	428.81	2.19
4.25W	1	0.30357	0.23268	0.00856	0.00389	164.3	2.7	7.80993E+01	96.52	0.01364	0.00024	444.70	1.92
4.6W	1	0.12193	0.19024	0.01525	0.00338	201.0	5.5	8.33035E+01	93.35	0.01461	0.00041	405.76	2.88
Fuse	1	0.21239	0.05939	0.00823	0.00101	644.7	9.4	1.00000E+02	96.43	0.01454	0.00021	419.60	1.72

Table 1/18. $^{40}Ar/^{39}Ar$ analytical results for sample 16TP23A aliquot #1, muscovite (n=1 xtl; J= 3.85084E-03± 0.25%)

Laser Wattage	Dwell Time (Min)	$^{37}Ar/^{39}Ar$	$^{37}Ar/^{39}Ar$ Error	$^{36}Ar/^{39}Ar$	$^{36}Ar/^{39}Ar$ Error	^{39}Ar (cps)	^{39}Ar (cps) Error	Cumulative % ^{39}Ar Released	% ^{40}Ar*	$^{39}Ar/^{40}Ar$	$^{39}Ar/^{40}Ar$ Error	Age (Ma)	1σ% Error (Ma)
4.025W	1	-0.00783	-0.30347	0.02087	0.00616	104.2	2.0	6.43819E-01	91.98	0.01287	0.00027	445.55	2.32
4.1W	1	0.06103	0.04052	0.00408	0.00083	749.1	9.4	5.27289E+00	98.53	0.01211	0.00015	499.14	1.52
4.125W	1	0.01596	0.03618	0.00229	0.00071	874.6	10.5	1.06769E+01	99.11	0.01304	0.00016	470.30	1.49
4.15W	1	0.10780	0.02901	0.00217	0.00057	1092.2	12.6	1.74255E+01	99.15	0.01314	0.00016	467.28	1.46
4.175W	1	0.04389	0.01945	0.00303	0.00040	1627.9	17.0	2.74845E+01	98.81	0.01322	0.00014	463.49	1.40
4.2W	1	0.08971	0.02515	0.00210	0.00050	1313.6	13.8	3.56013E+01	99.16	0.01340	0.00014	459.36	1.40
4.225W	1	0.02931	0.01726	0.00137	0.00032	1835.2	15.4	4.69415E+01	99.44	0.01379	0.00012	448.90	1.28
4.25W	1	0.00432	0.01974	0.00240	0.00040	1605.2	17.9	5.68600E+01	99.01	0.01385	0.00016	445.59	1.44
4.275W	1	0.08103	0.04335	0.01128	0.00092	794.9	10.4	6.17719E+01	95.57	0.01315	0.00017	452.24	1.62
4.5W	1	0.02621	0.01186	0.00232	0.00024	2788.7	20.5	7.90036E+01	99.07	0.01343	0.00010	457.92	1.23
4.65W	1	0.09834	0.03234	0.00486	0.00069	938.1	13.4	8.48003E+01	98.00	0.01380	0.00020	442.98	1.68
4.8W	1	0.18070	0.10028	0.01000	0.00223	301.3	4.8	8.66618E+01	96.11	0.01304	0.00022	457.72	1.85
Fuse	1	0.04579	0.01533	0.00413	0.00030	2158.6	15.9	1.00000E+02	98.32	0.01367	0.00010	448.01	1.24

Table 1/19. $^{40}Ar/^{39}Ar$ analytical results for sample 16TP23A aliquot #2, muscovite (n=1 xtl; J= 3.85084E-03± 0.25%)

Laser Wattage	Dwell Time (Min)	$^{37}Ar/^{39}Ar$	$^{37}Ar/^{39}Ar$ Error	$^{36}Ar/^{39}Ar$	$^{36}Ar/^{39}Ar$ Error	^{39}Ar (cps)	^{39}Ar (cps) Error	Cumulative % ^{39}Ar Released	% ^{40}Ar*	$^{39}Ar/^{40}Ar$	$^{39}Ar/^{40}Ar$ Error	Age (Ma)	1σ% Error (Ma)
4.0W	1	1.59387	0.34791	0.36973	0.01642	120.0	2.4	7.32655E-01	34.39	0.00594	0.00012	370.31	6.03
4.05W	1	3.12475	0.46940	0.04460	0.00699	91.4	1.9	1.29050E+00	83.22	0.01260	0.00029	417.30	2.73
4.1W	1	1.76898	0.34224	0.02126	0.00472	129.8	2.2	2.08292E+00	91.38	0.01358	0.00024	423.34	2.05
4.15W	1	1.40203	0.34871	0.01051	0.00497	127.2	2.2	2.85975E+00	95.94	0.01295	0.00023	460.94	1.96
4.175W	1	0.52896	0.07816	0.00351	0.00103	594.0	9.5	6.48708E+00	98.57	0.01364	0.00022	450.23	1.78
4.2W	1	0.32705	0.06344	0.00396	0.00084	699.9	9.7	1.07608E+01	98.42	0.01339	0.00019	456.84	1.64
4.225W	1	0.30263	0.04892	0.00315	0.00070	871.4	10.5	1.60820E+01	98.73	0.01347	0.00016	455.74	1.50
4.25W	1	0.22002	0.02909	0.00230	0.00041	1594.0	17.9	2.58154E+01	99.06	0.01377	0.00016	448.14	1.45
4.275W	1	0.06719	0.02314	0.00126	0.00032	1998.4	18.4	3.80182E+01	99.49	0.01370	0.00013	451.88	1.32
4.3W	1	0.13637	0.04099	0.00187	0.00063	1082.7	11.7	4.46298E+01	99.24	0.01350	0.00015	456.91	1.41
4.325W	1	0.20595	0.08352	0.00343	0.00127	531.5	8.0	4.78755E+01	98.56	0.01400	0.00021	439.74	1.72
4.55W	1	0.04914	0.04568	0.00105	0.00063	1012.9	14.5	5.40607E+01	99.55	0.01430	0.00021	435.04	1.65
Fuse	1	0.02953	0.01133	0.00141	0.00019	3761.6	27.4	7.70304E+01	99.41	0.01392	0.00011	445.07	1.23
Fuse	1	0.02953	0.01133	0.00141	0.00019	3761.6	27.4	1.00000E+02	99.41	0.01392	0.00011	445.07	1.23